

THE UNIVERSITY OF QUEENSLAND

AUSTRALIA

Quantum Photonics with Enhanced Quantum Dot Single-Photon Sources

Jihun Cha

M.S.



Candidate's ORCID

A thesis submitted for the degree of Doctor of Philosophy at

The University of Queensland in 2022

School of Mathematics and Physics

Abstract

My thesis focuses on improving the performance of single-photon sources based on a single quantum dot coupled to micropillar cavity. There are three important parameters to judge the quality of single–photons generated by this source—the degree of suppression of multi-photon emission, HOM-visibility, and source brightness. We demonstrated that by shaping the spectral profile of the pump excitation pulse laser, we can achieve a more efficient coupling with the micropillar, which leads to significant suppression of background noise. This procedure resulted in reducing multi-photon noise and increase of single-photon indistinguishability. This is achieved without spectral filtering in the single–photon collection path, therefore not compromising the source brightness.

We also considered automation of the optimisation procedure through machine learning techniques. The machine learning drastically simplifies the search for the best spectral pulse shaping. We test this automated procedure in different optimisation tasks. Surprisingly, when applying this optimisation procedure to improve single-photon indistinguishably, we achieved simultaneous increase of Hong-Ou-Mandel visibility and a 3-fold increase in source brightness.

We also explored automation of single-photon collection into a single-mode optical fibre. Here we used a deformable mirror to correct wave–front distortions on the source output emission. The automation of single-photon collection lead to an increase of coupling efficiencies by a factor as high as 70%.

Finally we also used spectral shaping of the pump laser to explore different excitation schemes for the quantum dot. In particular, we investigated the coherent two-colour excitation using the automated pulse shaping. We confirmed the generation of resonant single-photon emission in the quantum dot. Further we also explored phonon-assisted excitation. In both cases, it was possible to produce emission lines which are spectrally detached from the pump laser. Using these excitation techniques enables collection of single-photons without employing the cross polarisation filtering, leading to increase in brightness.

We hope the procedures described in this thesis can lead to better performance of quantum dot single-photon sources. It may also enable to employ this type of single-photon source to realise large scale photonic quantum computing and quantum communication technologies.

Declaration by author

(All candidates to reproduce this section in their thesis verbatim)

This thesis is composed of my original work, and contains no material previously published or written by another person except where due reference has been made in the text. I have clearly stated the contribution by others to jointly-authored works that I have included in my thesis.

I have clearly stated the contribution of others to my thesis as a whole, including statistical assistance, survey design, data analysis, significant technical procedures, professional editorial advice, financial support and any other original research work used or reported in my thesis. The content of my thesis is the result of work I have carried out since the commencement of my higher degree by research candidature and does not include a substantial part of work that has been submitted to qualify for the award of any other degree or diploma in any university or other tertiary institution. I have clearly stated which parts of my thesis, if any, have been submitted to qualify for another award.

I acknowledge that an electronic copy of my thesis must be lodged with the University Library and, subject to the policy and procedures of The University of Queensland, the thesis be made available for research and study in accordance with the Copyright Act 1968 unless a period of embargo has been approved by the Dean of the Graduate School.

I acknowledge that copyright of all material contained in my thesis resides with the copyright holder(s) of that material. Where appropriate I have obtained copyright permission from the copyright holder to reproduce material in this thesis and have sought permission from co-authors for any jointly authored works included in the thesis.

Publications included in this thesis

No publications included.

Submitted manuscripts included in this thesis

No manuscripts submitted for publication.

Other publications during candidature

Conference abstracts

1. **J. Cha**, L. Howard, A. Tranter, M. Su, M. P. Almeida, A. G. White, A toolbox for improving the performance of a solid-state single-photon source, *Korean Physical Society (KPS) Spring Meeting*, B12.07, Virtual conference, South Korea (2019).

2. **J. Cha**, Enhanced single photons from electrically-controlled quantum-dot micropillars, *23rd Australian Institute of Physics (AIP) Congress*, 12E - AIP QUICC, Perth, WA, Australia (2018).

Contributions by others to the thesis

No contributions by others.

Statement of parts of the thesis submitted to qualify for the award of another degree

No works submitted towards another degree have been included in this thesis.

Research involving human or animal subjects

No animal or human subjects were involved in this research.

Acknowledgments

I would like to express my gratitude to those who have helped me in various ways during my PhD period until this thesis is completed.

First of all, I would like to express my gratitude to Prof. Andrew G. White, who, as my supervisor at school, always encouraged me with new ideas and positive and bright smiles. Next, I would like to express my gratitude to Dr. Marcelo P. Almeida, my co-supervisor, who worked closely with me on quantum dots during my PhD. I would also like to express my gratitude to Dr. Till J. Weinhold, who gave a lot of advice and help regarding the usage and operation of laboratory equipment, and also to Dr. Jacquiline Romero, who always encouraged me with warm encouragement and a soft smile at group meetings. thank you for In addition to these people, I would like to thank all my colleagues who have experimented and researched with me at QTlab, at the SMP. I would like to thank Dr. Niccolò Somaschi, Dr. Juan C. Loredo for many advice on the quantum dot. In addition, I would also like to thank Prof. Won–Sang Chung, who often gave me words of encouragement by e-mail during difficult times.

Next, I would like to express my gratitude to my friends who have maintained a good relationship for more than 10 years and have always supported and encouraged me in my studies. Many thanks to Mr. John P Collins, Mr. Mark Collins, Mr. Anton Scicluna, Mr. Tonny Collins, Mr. Sam Mclean, Mr. Dan Cochrane, Mr. Lach Mclean, Mrs. Leonie Cochrane, Mrs. Denise Maclean, Mr. James Scicluna, Mrs. Amy Scicluna, the Mclean family.

Although not everyone's names are mentioned above, I want to express my heartfelt gratitude to everyone who assisted me during my PhD.

Lastly, I would like to express my deepest gratitude to my family, Mr. Young–Chul Cha, Mrs. Ji–Won Ahn, Miss. Hyo–Sun Cha, who believed in me and encouraged me until I finished my degree.

Financial support

ARC Centre of Excellence for Engineered Quantum System (EQUS)
University of Queensland Research Training Stipend
University of Queensland Research Training Tuition Fee Offset

Keywords

quantum physics, quantum optics, photonics, quantum dots, machine learning

Australian and New Zealand Standard Research Classifications (ANZSRC)

ANZSRC code: 510804, Quantum optics and quantum optomechanics, 30%
ANZSRC code: 510204, Photonics, optoelectronics and optical communication, 40%
ANZSRC code: 461105, Reinforcement learning 30%

Fields of Research (FoR) Classification

FoR code: 5108, Quantum physics, 80%
FoR code: 5102, Atomic, molecular and optical physics, 20%

Contents

Abstract ii

Contents **viii**

List of Figures **x**

List of Tables **xii**

List of Abbreviations and Symbols **xiii**

1 Intro to thesis **1**

2 Single–Photons from Solid-State Quantum Dot Sources **3**

2.1 Introduction 3

2.1.1 Multi–photon suppression 4

2.1.2 Indistinguishability 5

2.1.3 Brightness 6

2.2 Single–Photon Emission in a Quantum Dot 7

2.3 Cavity Quantum Electrodynamics with Quantum Dots 9

2.3.1 Spontaneous Emission Rate 9

2.3.2 Modification of Spontaneous Emission Rate 10

3 Source property and Alignment **13**

3.1 Electrically tunable solid–state QD single–photon sources 13

3.2 Source Alignment 15

3.2.1 *Pump–beam preparation, QD-source excitation, Single-photon collection, and Imaging system* 16

4 Manually Improving Quantum Dot Single Photon Sources **21**

4.1 Suppressing multi-photon generation 21

4.1.1 Spectral pulse-shaping 22

4.2 Improving single-photon indistinguishability 32

4.3 Pump–power characterisation 33

4.4 Enhancing single-photon production rates . . . 33
4.5 Different QD–excitation methods . . . 35
4.5.1 Phonon–assisted excitation . . . 36
4.5.2 Two-colour excitation . . . 37
4.5.3 Conclusion . . . 44

5 Automatic Optimisation of Quantum Dot Single Photon Sources 45
5.1 Introduction . . . 45
5.1.1 Gaussian Process . . . 47
5.1.2 Artificial Neural Network . . . 47
5.2 Preliminary Optimisations . . . 48
5.2.1 Preliminary Optimisation: $g^2(0)$ . . . 48
5.2.2 Preliminary Optimisation: HOM–visibility . . . 54
5.3 Machine-Learning Optimisation . . . 57
5.4 Towards the Best Quantum Emitter . . . 61
5.4.1 The final attempt of Machine–Learning Optimisation: $g^2(0)$ . . . 61
5.4.2 The final attempt of Machine–Learning Optimisation: HOM–visibility . . . 63
5.5 Improving the overall source efficiency . . . 64
5.5.1 Machine–learning Optimisation: Brightness . . . 64
5.6 Conclusion . . . 67

6 Discussion and Conclusion 71

Bibliography 75

A Machine Learning Code 85
A.1 $g^2(0)$ calculation in *Python* . . . 85
A.2 HOM–visibility calculation in *Python* . . . 86
A.3 SLM mask in *Python* . . . 88

List of Figures

2.1 Desiderata for excellent single-photon sources 4
2.2 Two typical excitation methods of the QD system to generate single-photon. 8

3.1 Photon source: semiconductor photonic–chip 14
3.2 Solid-state QD single-photon source (micropillar structure) 15
3.3 Overview of the configuration of three steps (1. ***Pump–beam preparation***, 2. ***QD–source excitation***, 3. ***Single–photon collection***) to obtain single photons from QD. 16
3.4 Pump preparation and source excitation 17
3.5 Single-photon collection and the imaging system 19

4.1 Spectral mismatch between the pump laser and cavity 22
4.2 A typical ultra-short pulse-shaping setup 23
4.3 Preliminary pulse laser spectrum shaping by using a micro-slit 24
4.4 Second-order correlation measurement of the single–photons obtained using the bandwidth ∼55GHz (8ps) pulsed laser as pump 26
4.5 Pulse laser spectrum shaper employing an SLM (LCOS-SLM x10468-03, Hamamatsu) . 28
4.6 $g^2(0)$ measured with superconducting nanowire single-photon detector (SNSPD) 31
4.7 Two-photon interference single–photon coincidence counting histograms when pulse shaping is not used (black) and used (violet) 32
4.8 Correlation between pump-power and single–photon count–rate 34
4.9 Temporal pulse multiplexing setup 35
4.10 Phonon-assisted excitation of QD 36
4.11 Concept of the coherent two-colour excitation method of a two-level system 37
4.12 Spectral change according to the strength of the sidebands (the blue–to–red peak distance: 0.410 ± 0.005nm) pulse pump laser 39
4.13 Near coherent driving QD with two-colour laser pulses 40
4.14 Evolution of the QD signal mixed with the two-colour pump laser when different voltages are applied 42
4.15 Spectral change according to the strength of the sidebands (the blue–to–red peak distance: 0.710 ± 0.005nm) pulse pump laser 43

5.1 Conceptual diagram of an artificial neural network 48
5.2 Logical flow chart of the machine learning process for pulse pump laser optimisation . . 49
5.3 Preliminary test run of machine–learning (ML) for $g^2(0)$ measurement 52
5.4 Preliminary test run of the machine–learning (ML) optimisation of the HOM–visibility measurement 55
5.5 Comparison of amplitude and phase changes of SLM pixels through the machine–learning (ML) process 56
5.6 Evolution of spectral shapes showing the results of HOM-visibility evolution by ML optimisation 57
5.7 Top-view of experimental apparatus considered in the pulse shaping protocol (exactly folded 4–f pulse shaper using an SLM) 58
5.8 Influence of humidity inside of the cavity of the pulsed pump laser to the machine–learning (ML) optimisation of the $g^2(0)$ measurement 60
5.9 Conceptual overview of the whole experiment setup 62
5.10 $g^2(0)$ ML optimisation process, a 40-second acquisition time for each run, Humidity = $9.0 \pm 0.3\%$ inside of the cavity of the pulsed pump laser 63
5.11 HOM–visibility ML optimisation process, a 200-second acquisition time for each run, Humidity = $7 \pm 2\%$ inside of the cavity of the pulsed pump laser 63
5.12 Conceptual diagram of the deformable mirror used in this project 65
5.13 Single–photon collection system with deformable mirrors 66
5.14 Machine–learning (ML) optimisation of single–photon count–rate by using the deformable mirrors 67

List of Tables

4.1 Comparison of $g^2(0)$ values among the QD single–photon sources 31

List of Abbreviations and Symbols

Abbreviations	
ANNs	Artificial neural networks
APD	Avalanche–Photo–Diode
BG	Background noise
BS	Beam–Splitter
CQED	Cavity–Quantum–Electrodynamics
DBR	Distributed–Bragg–Reflectors
EOM	Electro–Optical–Modulator
FBS	Fibre–Beam–Splitter
FSS	Fine-Structure Splitting
FWHM	Full–Width–Half–Maximum
GTI	Gires-Tournois–Interferometer
HWP	Half–Wave–Plate
KID	Kinetic–Inductance–Detector
LED	Light-Emitting–Diode
ML	Machine–Learning
PBS	Polarisation–Beam–Splitter
QD	Quantum–Dot
QKD	Quantum–Key–Distribution
QWP	Quarter–Wave–Plate
SLM	Spatial–Light–Modulator
SNSPD	Superconducting–Nanowire–Single-Photon–Detector
SPDC	Spontaneous–Parametric–Down–Conversion
TES	Transition–Edge–Sensor
STJ	Superconducting–Tunnel–Junction
CCD	Charge-Coupled–Device

Symbols	
f	Focal length

$g^2(0)$	Second-order correlation function at zero delay
$V(n)$	Variance in the photon number
n	Photon number
V_{HOM}	HOM–visibility
$C_{\parallel}$	Coincidence count when photons are maximally indistinguishable
$C_{\perp}$	Coincidence count when photons are maximally distinguishable
M	Indistinguishability
T	Transmission coefficient
R	Reflection coefficient
B_{QD}	Brightness of the quantum dot source
η	Overall collection efficiency
B_{lens}	Brightness at the first lens
β	Probability of a preferential emission into a target mode
η_{lens}	Probability of collecting a photon from the target mode into an optical lens
p_{state}	Probability of state
η_{QE}	Probability of radiative emission
$\otimes$	Product
$\mathbb{S}$	A quantum system
$\mathbb{E}$	Environment of the quantum system
$\mathscr{H}$	Hilbert space of the total system
$\mathscr{H}_{\mathbb{S}}$	Hilbert space of the quantum system
$\mathscr{H}_{\mathbb{E}}$	Hilbert space of the environment
$H_{\mathbb{S}}$	Self–Hamiltonian of the open system $\mathbb{S}$
$H_{\mathbb{E}}$	Free Hamiltonian of the environment
$\hat{H}_{\mathbb{I}}$	Hamiltonian describing the interaction between the system and the environment
$\rho_{\mathbb{S}}$	reduced density matrix
H	Hamiltonian
γ_0	Spontaneous emission rate
ω_0	Transition frequency
$\mathbb{D}(\omega)$	Effective density of modes
κ	Damping rate of the resonator
V	Effective mode–volume in a cavity
ω_c	Frequency of the cavity
ω	Frequency
c	Speed of light
k	Wave number
λ	Wave length
Q	Quality factor
γ_f	Spontaneous emission rate in free space
g	Dipole-coupling constant
γ'	Spontaneous emission of the electromagnetic field into the vacuum modes

Chapter 1

Intro to thesis

Why do we do science? It is not an easy question. This curiosity drives human technology to reach the level of creating artificial atoms these days. In quantum optics, solid-state quantum-dot (QD) serves as an important stepping stone. This is because solid-state QD single-photon sources have become possible that guarantee high purity and indistinguishability while overwhelmingly exceeding the brightness— 20 times brighter [1] —compared to any other single-photon sources. One interesting feature of this type of source is the deterministic production of single photons through pulsed laser pumping. This can significantly contribute to realising quantum computing and quantum communication by overcoming the limitation of probabilistic single-photon generation from spontaneous parametric down-conversion single-photon sources. Furthermore, we introduce most of the solutions to improve the performance of the world's best single-photon source.

This thesis talks about solid-state QD single–photon sources. It covers various attempts to align sources, and excitation methods, and improve the performance of generating single photons. Chapter 2 describes single–photons, and introduces important parameters required for single–photon sources. In addition, it explains the principle of generating single–photons from QDs, a brief theoretical background on cavity quantum-electrodynamics, introduces the single–photon source, and describes the composition of the experimental setup to use this source. Chapter 3 introduces the electrically tunable solid-state QD single–phonon source and describes the setup to generate single–phonon via resonant excitation by using a pulsed pump laser. This chapter gives details about the source property and the alignment. Chapter 4 introduces programmable spectral pulse shaping, and demonstrates the improvement of both multi-photon suppression and single-photon indistinguishability by manipulating the pulse pump spectral profile manually. Next, the single–photon count rate according to the pump laser power is investigated for the source's convenience. A simple experimental setup that can improve the single-photon production rates is introduced. A brief description and feasibility of two other different excitation methods (two-colour excitation and phonon-assisted excitation) are introduced. These are realised by utilising our programmable pulse shaper. Chapter 5 introduces the optimisation of three parameters—multi-photon suppression, indistinguishability, and brightness—through the machine learning process using the spectral pulse shaper. In addition, the overall single-photon

collection efficiency is improved by using a deformable mirror by machine learning. Therefore, all of those mentioned above can improve the performance of a solid-state QD single-photon source according to a given optical material or situation, and it is expected to greatly contribute to the application of this source. Chapter 5 demonstrates the best performance of the machine learning optimisation process for our source. This chapter concludes the overall effort to improve the performance of our source and highlights possible strategies to improve the single-photon source performance further. Chapter 6 shows the conclusion and discussion of this thesis.

There is a Korean word, “Hongik Ingan”. This means “To benefit the human world widely”, it is hoped that this thesis will be helpful to scientists using sources similar to this QD single–photon source in the future.

Chapter 2

Single–Photons from Solid-State Quantum Dot Sources

This chapter reviews three desirable properties of a single-photon source. These three parameters provide a quantitative reference for the improvement we will try in Chapter 3. A theoretical review of cavity quantum dynamics and QDs provides an understanding of how the emission from QD sources is mathematically enhanced. Next, a brief description of our source's properties and experimental system explains the structure of this QD single–photon source and the system of optical devices to drive the source. It also explains how the source works.

2.1 Introduction

High-quality single photons are a key resource in the development of many quantum technologies. Single-photon-based metrology protocols can improve resolution and precision beyond the standard noise limits [2]. In communication, quantum key distribution (QKD) with single-photons leads to completely secure transmission of cryptographic keys [3], quantum light sources that emit triggered single–photons or entangled photon pairs could help QKD systems function better [4]. In quantum computing, superposition and entanglement of single photons can process information at speeds well beyond what is classically possible [5]. These are only a few examples requiring the development of single-photon sources with optimised performance.

Figure 2.1 shows the desiderata for a single-photon source. The first is ***multi–photon suppression***. This captures how well the source generates one and only one photon and is determined by the value of the second-order correlation function at zero delay. The second is single-photon ***indistinguishability***, which captures how identical sequentially-generated photons are to each other, and is determined by the value of the Hong-Ou-Mandel visibility. Finally ***brightness*** measures how often we can obtain single photons from the source. It involves not only how fast we can produce the photons but also how well we can collect them. It is technically challenging to get a single–photon source that satisfies all three conditions at the same time.

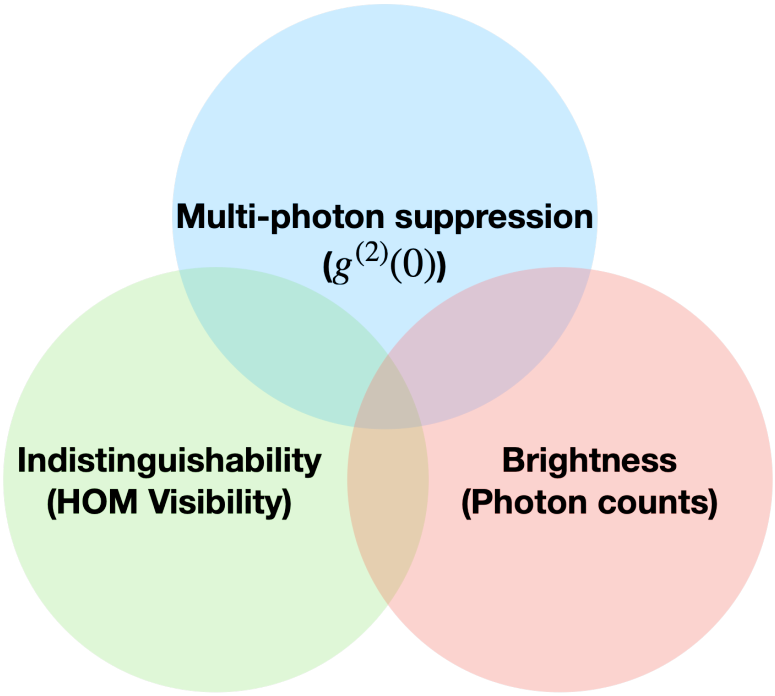


Figure 2.1: Desiderata for excellent single-photon sources

2.1.1 Multi–photon suppression

Multi-photon suppression refers to the capacity of the source to deliver photons only in a $n = 1$ Fock state. Here, a Fock state is a quantum state that is an element of a Fock space with a well-defined number of particles (or quanta) [6]. In this case, the source generates one–and only one–photon per each pulse-excitation. Multi–photon suppression is quantified by measuring the second-order correlation function at zero delays, namely, $g^2(0)$. Here, $g^2(0)$ is defined [7] by

$$g^{(2)}(0) = \frac{\langle a^\dagger a^\dagger a a \rangle}{\langle a^\dagger a \rangle^2} = 1 + \frac{V(n) - \bar{n}^2}{\bar{n}}, \tag{2.1}$$

where, $a^\dagger$ [8] is the photon-creation operator that increases the number of photons in a given state by one, a [8] is the photon-annihilation operator that decreases the number of photons in a given state by one, $V(n)$ is the variance in the photon number, $V(n) = \langle (a^\dagger a)^2 \rangle - \langle a^\dagger a \rangle^2$, and n is the photon number. Because the variance is zero for a number state, in the case of a perfect single–photon, the average number of photons per pulse is 1, so the value of $g^2(0)$ is 0.

To measure $g^2(0)$, consider the expected value of simultaneously detecting a single photon from two detectors at the two outputs of the 50:50 beam splitter (BS), $g^2(0)$ is defined in Ref. [9],

$$g^{(2)}(0) = \frac{\langle n_1(t) n_2(t) \rangle_t}{\langle n_1(t) \rangle_t \langle n_2(t) \rangle_t}, \tag{2.2}$$

where, $n_1(t)$, $n_2(t)$ are the number of counts detected on the detector-1,-2 at time t, respectively. more details about probabilistic consideration of detection event to calculate $g^2(0)$ can be found in Ref.[10, 11]. This measurement was first described by Hanbury Brown and Twiss [12], and shows

no coincidence events between detector 1 and detector 2 for the outputs from a 50:50 BS when only consecutive single-photons enter ($1 - g^2(0)$ is sometimes called the purity). Higher multi–photon suppression means lower values of $g^2(0)$. If only a single-photon is generated from a QD, the value of the second-order correlation function at zero delay is equal to 0.

2.1.2 Indistinguishability

Generally, single-photon indistinguishability is quantified by the visibility obtained from a Hong-Ou-Mandel (HOM) experiment [13]: when two indistinguishable single-photons simultaneously enter at the input ports of a 50:50 BS there will be an absence of coincidence counts between two detectors positioned at the output ports. This bunching effect is a certificate of the non-classicality of light. This unique property of photons is the most fundamental resource for optical quantum information processing [14]. The key figure of merit to quantify single-photon indistinguishability, the HOM–visibility, is defined in Ref. [9] as,

$$V_{HOM} = \frac{C_{\perp} + C_{\parallel}}{C_{\perp}}, \tag{2.3}$$

where, $C_{\parallel}$ is the second-order coincidence count which can be measured between two detectors placed on the two outputs of a 50:50 beam splitter when two identical single photons are provided into each of the two inputs of the beam splitter, $C_{\perp}$ is the second-order coincidence count which can be measured between two detectors placed on the two outputs of a 50:50 beam splitter when two distinguishable single photons (for example, with orthogonal polarisation) are provided into each of the two inputs of the beam splitter when photons are maximally distinguishable and can be obtained by varying the polarisation or arrival time of the photons at the beam splitter.

On the other hand, indistinguishability, M is defined in Ref. [9] as,

$$M = V_{HOM}\left(\frac{R^2 + T^2}{2RT}\right) \tag{2.4}$$

where, $T = 1 - R$, T and R are the transmission and reflection coefficient of the beam splitter, respectively. When $R = T = 0.5$, indistinguishability, M simply equals HOM visibility.

An extracted indistinguishability is considered in Ref. [9] as,

$$M^{\star} = M + g^2(0) \tag{2.5}$$

where, M is the indistinguishability which can be obtained by eq.2.4, $g^2(0)$ is the second-order correlation function at zero delay. Eq.2.5 is useful for more accurately diagnosing the performance-limiting factors when developing a single-photon source because the multi-photon suppression and single-photon indistinguishability of QD single-photon source can be controlled independently. Eq.2.5 refers to the description of the wave packet overlap that pertains to all the degrees of freedom except for the photon number.

2.1.3 Brightness

It has been stated in Ref. [9] that various figures of merit are employed to measure the brightness of a single-photon source. These measures include the count rate of the detector, photons collected per second, and the brightness of the first lens. The selection of the appropriate measure depends on one's perspective, and making comparisons can be difficult.

In the case of deterministic QD single-photon sources, it is defined as the number of photons collected per excitation pulse into the first lens in Ref. [1], each pulse to be collected should consist of only a single photon without a vacuum component— an element with no photons in the wave packet collected from the source —and should be measurable. In the case of photon pair sources, it is defined as the probability of having exactly one photon in a single-mode fibre at a given clock cycle in Ref. [15]. Both definitions of brightness consider how frequently and efficiently a single-photon source produces single photons. In reality, the loss of the generated single photons as they pass through the optics is inevitable, but it is preferred to minimise the loss as much as possible.

One way to express the brightness of a single-photon source is the brightness at the first lens, which is defined in Ref. [9],

$$B_{lens} = \beta \eta_{lens} p_{state} \eta_{QE}, \tag{2.6}$$

where, β is the probability of a preferential emission into a target mode— here $\beta = \Gamma_{mode}/(\Gamma_{mode} + \Gamma_{others})$, where Γ_{mode} is the emission rate into the target mode, Γ_{others} is the emission rate into all other modes —, η_{lens} is the probability of collecting a photon from the target mode into the first optical lens, p_{state} is the probability of the initial state of QD, in which the QD is ready to emit a single photon— Ideally, $p_{state} = 1$ at saturated power —, and η_{QE} is the quantum efficiency of the transition: the probability of radiative emission. the emitting state quantum efficiency is defined as $Q = k_{rad}/(k_{rad} + k_{nrad})$ in Ref. [16], here k_{rad} is the radiative decay rate, k_{nrad} is the non-radiative decay rate. i.e. the probability of a QD relaxing from its lowest-excited state by emitting a photon. Note that it is important to understand the difference between the quantum yield and the quantum efficiency. The quantum yield is the probability that a photon will be emitted after one photon has been absorbed. On the other hand, quantum efficiency is the probability that a photon will be emitted after the system has been excited to its emitting state. However, in a two-level system, the quantum yield is equal to the quantum efficiency of the emitting state. This is because each photon absorption excites the system to its emitting state. Note that this definition of brightness is mostly referenced in general.

As a more practical consideration beyond the definition of brightness in the first lens, the definition of brightness coupled to single-mode fibre is presented in Ref. [15] as,

$$B_{QD} = p_1 \eta, \tag{2.7}$$

where, p_1 is a single-photon probability— the probability of having exactly one photon in a single-mode fibre at a given clock cycle —, η is the overall collection efficiency which is the coupling

efficiency from the source to single-mode fibre.

One phenomenon that can affect the brightness of fluorescence in QDs is blinking. It is known as fluorescence intermittency— irregular alternation of phases of fluorescence the phenomenon in which a QD randomly cycles between a bright emitting ON state and a dark non-emitting OFF state under continuous excitation [17]. Under a wide range of experimental conditions, QD blinking is known to exhibit inverse power law statistics [18, 19]. However, controllable variables can affect blinking behaviour— for example, QD structure engineering [20] and environment control [21] can reduce blinking—, benefiting most applications. Blinking is affected by the energy and intensity of the excitation source. Higher energy excitation impacts blinking statistics [22] and contributes to fluorescence decay, blue-shift, and peak broadening [23]. Multiple excitons— electron and hole pairs —have been experimentally and theoretically linked to changes in blinking behaviour [24, 25, 26]. This evidence highlights the importance of understanding the formation of excitons to fully comprehend the behaviour of QD. Ref. [27] compares the impact of pulsed and continuous wave (CW) laser excitation on the photophysical properties of a single QD. In the case of pulsed excitation, the average number of excitons per pulse is given by,

$$\langle N \rangle_{\mathrm{pul}} = \ln 2 \frac{P}{E_{\mathrm{p}} \Gamma} \frac{\sigma_{\mathrm{abs}}}{\pi r^2}, \tag{2.8}$$

where, P is the average laser power, E_{p} is the photon energy, Γ is the repetition rate of the pulsed laser, σ_{abs} is the absorption cross-section, r is the radius of the focus laser beam at the full-width-half-maximum of its intensity. In the case of CW excitation, the average number of excitons per fluorescence lifetime is given by,

$$\langle N \rangle_{\mathrm{cw}} = \ln 2 \frac{P \tau_{\mathrm{f}}}{E_{\mathrm{p}}} \frac{\sigma_{\mathrm{abs}}}{\pi r^2}, \tag{2.9}$$

where,τ_{f} is the fluorescence lifetime. They showed that when using pulsed excitation, the effects of photobleaching are exaggerated, which results in a lower probability of long ON fluorescence blinking events and leads to shorter fluorescence lifetimes compared to CW excitation at the same wavelength and average intensity. However, the spectral wandering, biexciton quantum yields, and power law exponents that describe fluorescence blinking are largely unaffected by the type of laser excitation used.

2.2 Single–Photon Emission in a Quantum Dot

There are various types of QDs, and they are classified into various types according to the manufacturing process and the materials used. Here we limit ourselves to solid–state QDs [28], in particular, indium–gallium–arsenide (InGaAs) QDs.

QDs are artificial atomic systems —microscopic semiconductor particles that are typically a few nanometers in size— and because of their small size, they are strongly affected by quantum mechanics. Like electrons bound in an atom, electrons trapped in a QD show different optical properties from

those of large particles, and this depends on the size of the QD. Due to strong electric confinement in all three dimensions, electrons in the QD have discrete energy states in the semiconductor energy band gap [29, 30]. (The band gap is the range of energies in a solid in which electronic states are forbidden, and usually represents the energy difference between the top of the valence band and the bottom of the conduction band of insulators and semiconductors. Thus the band gap is the energy required to induce an electron bonded to an atom to become a conduction electron).
The mechanism responsible for generating single-photons in the QD is spontaneous emission [8]. When the QD is excited with the laser, the electrons can be promoted to one of these discrete energy states leaving a hole in the valence band. This electron-hole pair, also known as an *exciton*, recombines through spontaneous emission of a single-photon [31].

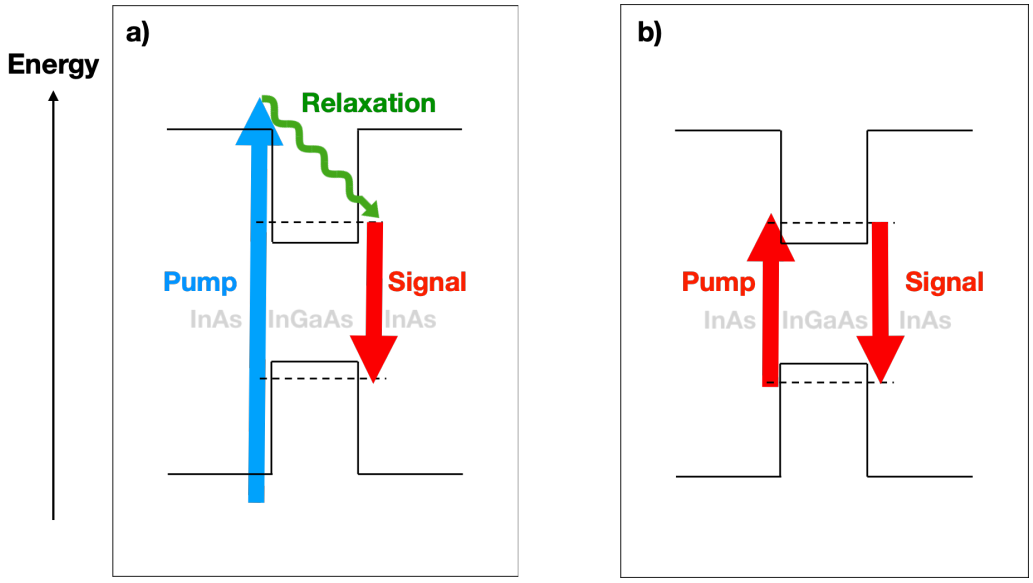


Figure 2.2: Two typical excitation methods of the QD system to generate single-photon. a) Above-band excitation: electrons in the valence band absorb the energy of the pulse laser (blue arrow) and are excited to go to the conduction band. Since the electron has absorbed energy greater than the energy band gap of the electron, it changes to the excited state of the electron trapped in the QD through energy loss due to heat and vibration (green arrow). Electrons in the excited state emit single photons through spontaneous emission (red arrow) and return to the ground state. b) Resonant excitation: Since the energy of the pump pulse (left-hand side red arrow) matches the energy band gap of the electron trapped in the QD, the excited electron comes down to the ground state by emitting a single photon through spontaneous emission (right-hand side red arrow).

To obtain spontaneous emission we use optical excitation with a pulsed laser pump. There are different ways to excite this system with laser pulses to obtain single photons. The easiest way is to use a pump laser with energy above the band gap and wait for the electrons to decay to the state of the QD as shown in Figure 2.2 a). However, since an electron is excited by receiving energy greater than the energy gap forming an exciton, there is a waiting time until it loses energy in the form of heat or phonon. This process has an additional impact on dephasing because the emission of the photons occurs randomly within the relaxation process [32]. Representative papers using this QD excitation method are Ref. [33, 34, 1].

We can also use resonant excitation where we pump the QD directly to the excited state as shown in Figure 2.2 b). This way we can avoid dephasing, allowing us to obtain higher indistinguishability single-photons, which is key for quantum optical information processing. Representative papers using this excitation method refer to Ref. [33, 1, 35].

Note that it can be said that the resonance pumping method is advantageous in increasing indistinguishability compared to above-band excitation. This is because the resonant pumping method provides only enough energy to raise the QD to the lowest excited state without any extra energy, so after only one electron-hole pair (exciton) is created, it decays and emits a single photon. This means that we can avoid the situation when there are spectral mismatches between the pump and the cavity, and we have a large source of noise due to backscattering. This is an undesirable additional source of noise, considering we need to remove the pump laser from the single-photon signal. This noise affects the performance of the source, in particular the $g^2(0)$ and HOM-visibility. This is a big problem if we consider the scalability of our sources. Ref. [36] from our collaborators from the Pascale Senellart group shows that multi-photon noise is detrimental and reduces HOM-visibility even more than dephasing. This result supports that the resonance excitation of the source can increase the indistinguishability of single-photons, compared to the above-band excitation.

2.3 Cavity Quantum Electrodynamics with Quantum Dots

The interaction between discrete photon modes of optical cavities with a high-quality factor (Q-factor) and two-level (ground and the lowest excited state) atomic system can be explained by cavity quantum electrodynamics (CQED) [37]. An optical cavity can be formed in our case due to the micropillar surrounding the QD. This micropillar has an alternating structure of two semiconductor materials with different refractive indices. When the QD is located at the centre of this optical cavity, the electrons captured in the QD rise to the lowest excited state in the conduction band by absolving the energy provided from the outside of the micropillar. As a result, a hole is left in the balance band, leading to the creation of an exciton (electron-hole pair). When this electron falls to the ground state and recombines with the hole, a single photon can be emitted. Typically, single photons generated from QDs spread in random directions. However, the structure surrounding the QD creates an optical cavity, which allows us to benefit from spontaneous emission with a specific direction. Moreover, according to the resulting formula of the master equation, the spontaneous emission is amplified due to the optical cavity. Understanding the physical properties of single photons generated from a source requires a basic theoretical background in CQED.

2.3.1 Spontaneous Emission Rate

Spontaneous emission is the process by which a quantum mechanical system, such as a molecule, atom, or subatomic particle, transitions from an excited energy state to a lower energy state, releasing a quantised amount of energy in the form of photons.

There are various methods —— the Gorini–Kossakowski–Sudarshan–Lindblad equation (GKSL: quantum optical master equation) [38, 39], using Wegner-Weisskopf theory [40] and Fermi's Golden Rule [41] ——to drive the spontaneous emission rate, here we briefly introduce the master equation approach.

In general, if we say an open system is a quantum system $\mathbb{S}$, another quantum system $\mathbb{E}$ which is the environment of the quantum system $\mathbb{S}$, the total system can be denoted as $\mathbb{S}+\mathbb{E}$. The Hilbert space of the total system is given by the tensor product space, $\mathscr{H} = \mathscr{H}_{\mathbb{S}} \otimes \mathscr{H}_{\mathbb{E}}$, where, $\mathscr{H}$ is the Hilbert space of the total system, $\mathscr{H}_{\mathbb{S}}$ is the Hilbert space of the quantum system, $\mathscr{H}_{\mathbb{E}}$ is the Hilbert space of the environment. Then, the Hamiltonian of the total system can be written as, $H = H_{\mathbb{S}} \otimes I_{\mathbb{E}} + I_{\mathbb{S}} \otimes H_{\mathbb{E}} + \hat{H}_{\mathbb{I}}$, where, $H_{\mathbb{S}}$ is the self–Hamiltonian of the open system $\mathbb{S}$, $H_{\mathbb{E}}$ is the free Hamiltonian of the environment, $I_{\mathbb{S}}$ is the identity operator in the Hilbert space of the open system, $I_{\mathbb{E}}$ is the identity operator in the Hilbert space of the environment, $\hat{H}_{\mathbb{I}}$ is the Hamiltonian describing the interaction between the system and the environment. Considering this total Hamiltonian in the quantum master equation in Ref.[39], we can describe the dynamics of the system and the environment. By Neglecting the Lamb shift and the Stark shift terms in the quantum master equation, the time-dependent of the reduced density matrix of the open quantum system is governed by the spontaneous emission rate, γ_0 is the spontaneous emission rate. This γ_0 can be expressed as,

$$\gamma_0 = \frac{4\omega_0^3 \left|\vec{d}\right|^2}{3\hbar c^3} \tag{2.10}$$

Therefore, the dissipator of the master equation describes spontaneous emission processes (rate γ_0) as well as thermally induced emission and absorption processes (rates γ_0 N). The total transition rate can be denoted by $\gamma = \gamma_0(2N+1)$, where $N = N(\omega_0)$ is the Planck distribution at the transition frequency.

2.3.2 Modification of Spontaneous Emission Rate

The modification of spontaneous emission in a cavity can be understood by replacing the density of modes for free space with a cavity-modified density of modes. The effective density of modes is given in Ref. [42],

$$\mathbb{D}(\omega) = \frac{\kappa}{2\pi V} \frac{1}{(\frac{\kappa}{2})^2 + (\omega_c - \omega)^2}, \tag{2.11}$$

where, κ is the resonator damping rate, V is the effective mode–volume in a cavity, ω_c is the frequency of the cavity, $\omega = ck$. The quality factor: Q-factor is defined as,

$$Q = \frac{\omega_c}{\kappa} \tag{2.12}$$

Depending on the detuning between the cavity frequency and the atomic transition frequency, the spontaneous emission from the cavity can be expressed using the Q–factor and the spontaneous emission in free space.

Firstly, enhanced spontaneous emission for a QD in resonance with the cavity;

$$\gamma_c \simeq \gamma_f \left(\frac{\lambda_0^3}{V}\right) Q. \tag{2.13}$$

Secondly, suppressed spontaneous emission for a QD off-resonance with the cavity;

$$\gamma_c \simeq \gamma_f \left(\frac{\lambda_0^3}{V}\right) Q^{-1}, \tag{2.14}$$

where, $\lambda_0 = 2\pi c/\omega_0$, γ_f is the free space spontaneous emission rate.

The coupling between QD and cavity mode can be quantitatively classified into two categories—weak-coupling regime, and strong-coupling regime—using the three coupling parameters. The first is the dipole-coupling constant between the atom and the cavity mode; g— Note that the coupling strength depends on the magnitudes of the transition dipole moment of the excitons $|\mu|$, the cavity field $|E_0|$, and their relative orientation [43] —, the second is the decay rate of this mode; κ, and the third is the rate of spontaneous emission into the vacuum modes of the electromagnetic field; γ', which differs from the free space spontaneous emission rate γ_f due to the reduction of the solid angle in which the atoms see the vacuum.

The weak-coupling regime is characterized by $g \ll \gamma'$, κ for open cavities and $\gamma' \simeq 0$ for closed cavities. In this scheme, the upper electronic state population undergoes a simple exponential decay at the rate, of $\gamma = \gamma' + \gamma_0$, where,

$$\gamma_0 = \left(\frac{2g^2}{\kappa}\right) \frac{1}{1+2(2\delta/\kappa)^2)} \tag{2.15}$$

where, $\delta = \omega_c - \omega_0$ is the QD-cavity detuning. In the particular case of a closed microcavity — $\gamma' = 0$, $\delta = 0$ — Equation 2.16 can be written explicitly,

$$\Gamma_{max} = \left(\frac{3\lambda_0^3}{4\pi^2}\right) \frac{Q}{V} \gamma_f \tag{2.16}$$

Note that the term $3\lambda_0^3 Q/4\pi^2 V$ is called, Purcell factor [44]. Equation 2.19 explains the enhancement of spontaneous emission rates of QDs when they are incorporated into resonant cavities.

On the other hand, the strong–coupling regime is characterized by $g \gg \gamma'$, κ, δ for open cavities. In this regime, the coupling between the QDs and the cavity mode is strong, so there is a high probability that the emitted single photons will be reabsorbed before escaping. Also, the decay curve will consist of oscillations at the vacuum Rabi frequency.

Chapter 3

Source property and Alignment

This chapter introduces the QD single–photon source we used and describes the setup we used to generate single–photons via resonant excitation by using a pulsed pump laser.

3.1 Electrically tunable solid–state QD single–photon sources

In this thesis, we work with a single–photon source based on QD embedded in a micropillar which is fixed on a chip of about 1cm$\times$ 1cm finger size.

Figure 3.1 a) shows the chip contains QD single-photon sources. This chip is placed and secured on a 3-axis positioning chip-holding post, stored inside a cryostat (Montana Instruments) at a temperature of $\sim$ 4K. The holding post is connected by wire to a 3-axis (x, y, z) position adjustment device (AttoCube) outside the cryostat. Depending on the values entered into AttoCube, the chip holder can be independently controlled in three spatial coordinate axes (x, y, z), allowing the chip to be controlled to be pumped according to the incident beam. The chip itself is connected to an external power supply, electrical bias can be applied to adjust the energy transition of the QD, ensuring spectrally accurate alignment between the pulsed pump laser and the QD.

Figure 3.1 b) shows an enlarged view of this chip. There are about 17 yellow island structures (ship-shaped), and several islands are connected by black lines connected to an external voltage source. As can be seen in the picture, not all yellow island structures are connected to an external voltage source, and some micropillars are independent and not connected to the yellow island structure.

Figure 3.1 c) is an enlarged view of the yellow square in Figure 3.1 b). Only the part where the micropillars are well connected to the yellow structure is enlarged, and the yellow circle represents a specific island structure where eight micropillars are connected.

Figure 3.1 d) shows an enlarged view of the particular island structure in Figure 3.1 c). it shows the top-view structure of the micropillars, each micropillar is connected to the cylindrical frame, and the crossroads bridges connect the pillar and the outer frame. The yellow circle, numbered 1 indicates

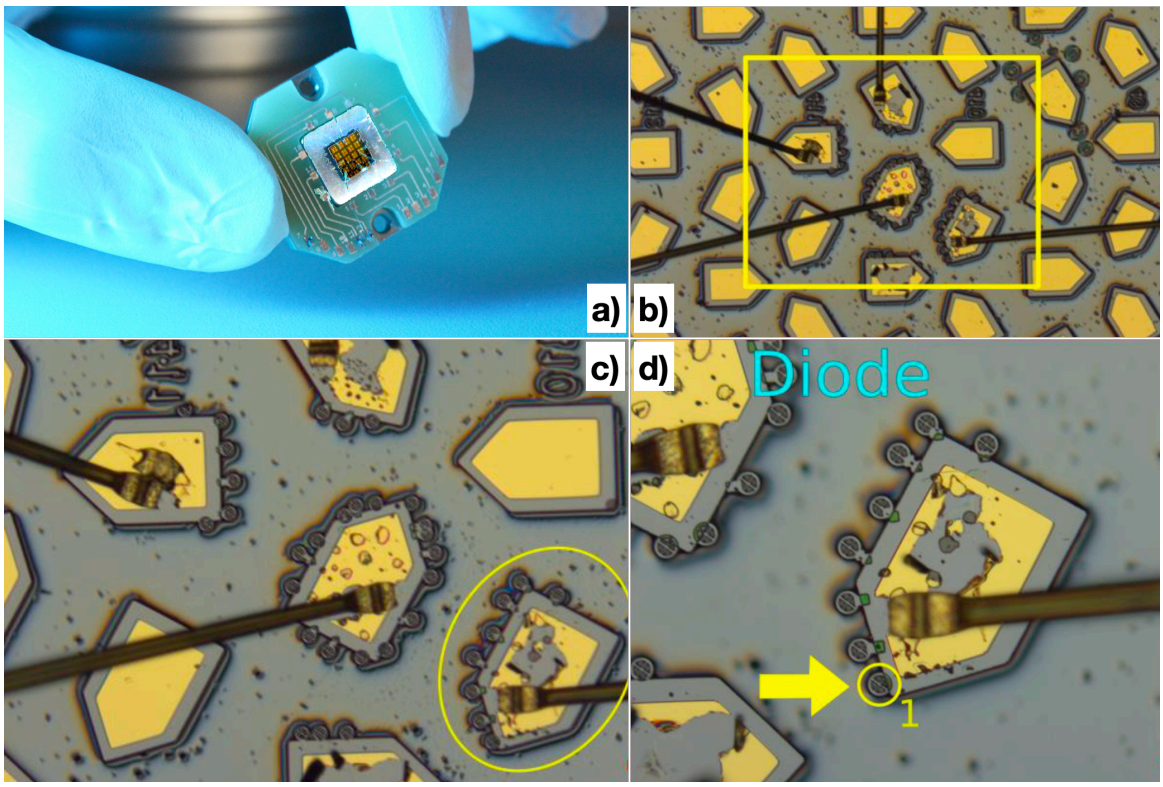


Figure 3.1: Photon source: semiconductor photonic–chip. a) A finger-sized chip containing dozens of micropillar-shaped QD single photon sources. b) Several diodes are distributed in a chip of size about 1cm$\times$ 1cm. Wires are connected to the top of each diode. The enlarged image of the yellow rectangular area is shown in c). c) In the photo area, about 30 or more micropillars are connected to the tubular outer frame, and these frames are connected with diodes. The enlarged image of the yellow circled area is the same as d). d) A diode with eight micropillars located in the centre of the picture. One of the micropillars marked with the yellow number 1 represents QD-33, which is used as the single-photon source in this thesis. [Images courtesy of Quandela].

the location of the micropillar that we are researching in the thesis. Note that the micropillar indicated by the number 1 is equivalent to the single-photon source called QD-33 studied in this thesis.

A QD made of InGaAs appears bright yellow in the wetting layer made of InAs, as shown in Figure 3.2 a). In transmission electron microscopy images, the size of QD appears to be smaller than 20 nanometers. The upper and lower parts of the wetting layer are surrounded by layers composed of GaAs in a sandwich shape. A schematic representation of the QD source is shown in Figure 3.2 b). The micropillar cavity [45] surrounding the QD consists of layers of distributed Bragg reflectors (DBR) [46] formed by alternately stacking two materials with different refractive indices. The thickness of a DBR is designed to be $\sim \lambda/4$ to achieve the best reflection [47], where λ is the wavelength of the light of interest. More details about the DBR can be found for instance in Refs. [48, 49, 50].

As we mentioned in Section 2.3.2, coupling the QD into the cavity leads to spontaneous emission enhancement and also directs the photons into a preferential emission mode (cavity–mode) [51]. Additionally, the Purcell effect [44] reduces dephasing, which helps to improve single-photon indistinguishability. For details on the fabrication processes to obtain these sources can be found in Refs. [52, 53, 1].

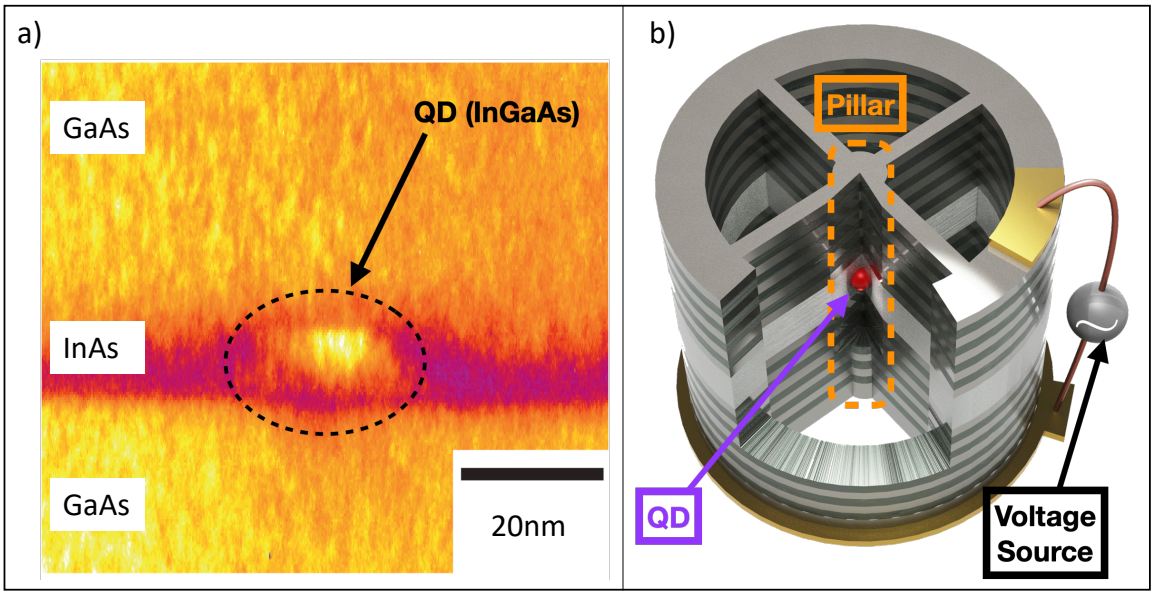


Figure 3.2: Solid-state QD single-photon source (micropillar structure). a) Transmission electron microscopy image of a single self-assembled indium–gallium–arsenide (InGaAs) QD. ∼20nm size QD embedded in an indium–arsenide (InAs) layer between gallium–arsenide (GaAs) layers. Image from Ref.[8]. b) A single micropillar cavity comprises the GaAs/InAs layers. The layers are alternately stacked. In general, the layers under the micropillar are thicker than the top, so that the bottom side acts as a fully reflective mirror and the top side acts as a partially reflective mirror. This micropillar is designed and produced to locate the QD in the optimal position to couple with the micropillar cavity mode. Micropillar structure connected to the outer frame, the energy transition bandgap of the QD can be adjusted by applying a voltage. [Images courtesy of Quandela].

3.2 Source Alignment

Source alignment can be roughly divided into three steps to obtain the highest quality single photons. 1. ***Pump–beam preparation***, 2. ***QD–source excitation*** and 3.***Single–photon collection***. In addition, a sample–imaging system for alignment between the cavity position and the pump laser is essential and is used temporarily during QD-source excitation. This imaging system connects to the excitation and the collection path.

Figure 3.3 is a schematic illustration showing the pump beam preparation, excitation, collection, and imaging system and the optical elements required for setup to optically excite a QD single-photon source located in a sealed cryostat. HWP2 and BS, drawn as dashed boundaries in the figure, are inserted only when using an imaging system that takes into account the alignment of the QD and the excitation beam and is not used while exciting the QD to generate a single-photon.

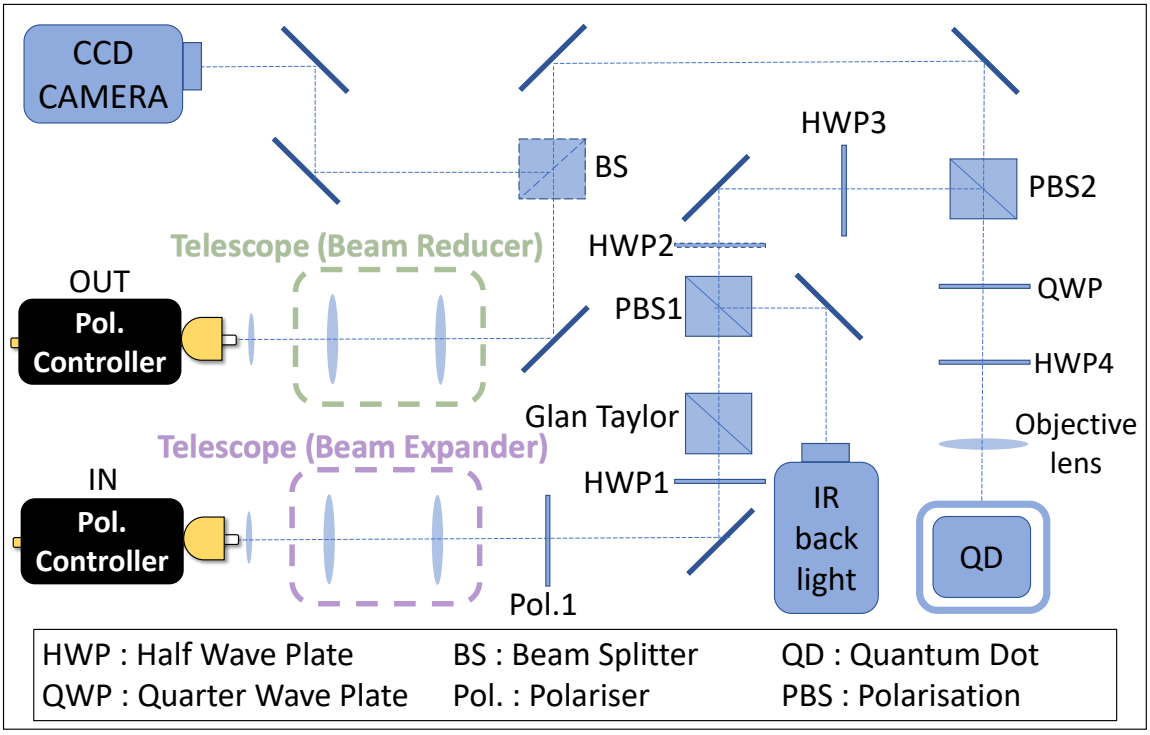


Figure 3.3: Overview of actual configuration of three steps (1. ***Pump–beam preparation***, 2. ***QD–source excitation***, 3. ***Single–photon collection***) to obtain single photons from QD. These three steps are shown in Figure 3.4 a)-b) and Figure. 3.5 a). ***Sample–imaging system*** is shown in Figure 3.5 b).

3.2.1 *Pump–beam preparation, QD-source excitation, Single-photon collection, and Imaging system*

Pump–beam preparation

Optical resonant excitation requires tailoring both the spatial and spectral properties of the pump laser. The excitation laser is provided by a Ti: Sapphire laser (Spectra Physics Tsunami). The laser output is coupled into a single-mode fibre and redirected to the cryostat by a combination of optical elements.

Figure 3.4 a) shows the beam path of the pump-beam preparation. A well-collimated pulsed pump beam provided through a fibre coupler increases in beam diameter through a telescope (beam expander). This enlarged beam passes through Pol.1 and is polarized in a specific direction. The pump beam passes through HWP1, Glan-Taylor, PBS1, HWP2, and HWP3 in order and arrives at PBS2. The pump beam, which has a vertical polarisation direction by adjusting HWP3, is reflected vertically in PBS2, passes through QWP, HWP4, and Objective lens, then passes through the glass window at the top of the cryostat and is focused on the top of the micropillar located inside To reduce the beam waist so that the beam is coupled to the upper part of the micropillar, a large beam size must pass through an objective lens with a large magnification. Therefore, the beam emitted from the single-mode optical fibre is collimated in free space using a lens, and then the size of the beam is increased using a telescope (beam expander, f = 35mm convex, f = 75mm biconvex).

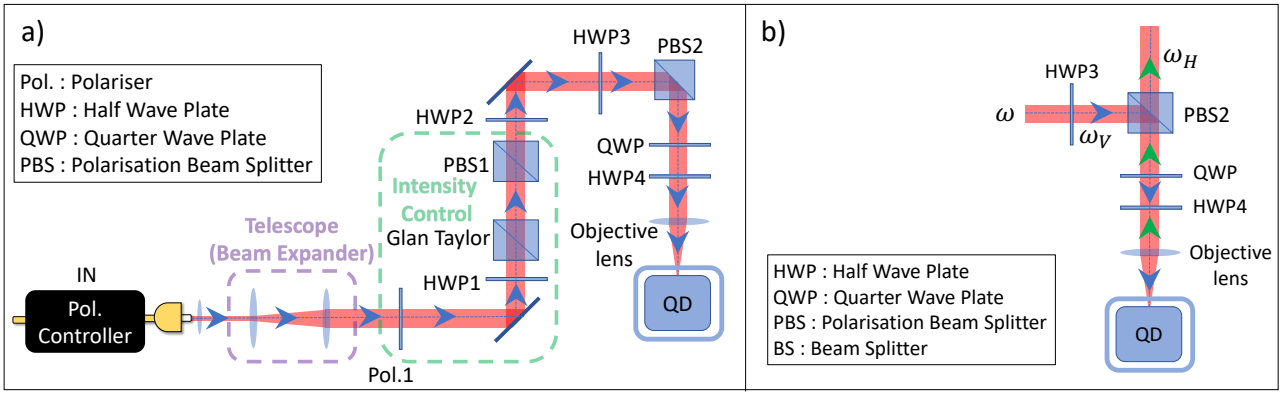


Figure 3.4: Pump preparation and source excitation. a) Pump-beam preparation. A well-collimated pulsed pump beam provided through a fibre coupler increases in beam diameter through a telescope (beam expander). This enlarged beam passes through Pol.1 and is polarized in a specific direction. The pump beam passes through HWP1, Glan-Taylor, PBS1, HWP2, and HWP3 in order and arrives at PBS2. The pump beam, which has a vertical polarisation direction by adjusting HWP3, is reflected vertically in PBS2, passes through QWP, HWP4, and Objective lens, then passes through the glass window at the top of the cryostat and is focused on the top of the micropillar located inside (PBS1 and HWP2 are Essentially used to control the infrared (IR) backlight used by imaging systems). b) QD–source excitation. The pulsed pump beam frequency is equal to the frequency of the output single photons. HWP3 and PBS2 are used to separate the pump beam and single photons. QWP and HWP4 are used to match the polarization direction between the pump laser and the micropillar cavity.

Setting the laser wavelength in resonance with the QD transition, we excite the with a π-pulse—a short pump pulse that has the area to excite the QD system with nearly unity probability, which results in the emission of a single-photon wave-packet with high probability. The response of the QD-single photon source to different pulse areas is described in more detail in Ref. [54]—, reaching the objective lens as nearly a planar wavefront. This procedure is employed to minimise optical aberration during propagation through the objective.

The infrared (IR) backlight is used in the imaging system to check the intensity of the pump laser and the position of the cavity in the process of aligning the source. This is to control the intensity of the IR backlight independently. When using only PBS1, the pump laser passes through PBS1 and has H-polarisation, and the backlight is reflected inside PBS1 and bent to have V-polarisation when the back-light is irradiated onto the cavity. Since the polarisation directions of these two beams are perpendicular to each other, the pump laser cannot be seen at the maximum brightness of the backlight to secure the view.

QD–source excitation

Our system collects single photons by pumping the QD using a resonance excitation method: the frequency of the pump laser and the collected single photons is the same. Accordingly, it is impossible to remove the pump laser using a spectrum filter as used in other optical excitation methods, e.g., above-band excitation or phonon-assisted excitation. We use cross-polarisation excitation: the polarisations of the pump laser and single-photon signal are perpendicular to each other.

Figure 3.4 b) shows the beam path of the QD-source excitation. We set the pump laser to have linearly polarised light in a specific direction using HWP3, and then reflect it from PBS2. The reflected beam passes through QWP and HWP4, and is focused on the micropillar located in the cryostat through the objective lens (OLYMPUS LCPLN20XIR). Since the micropillar cavity has a polarisation axis in a specific direction, the combination of QWP and HWP4 can match the polarisation direction between the pump laser and the micropillar cavity. This step is accompanied by the use of a sample–imaging system and serves to ensure that the position of the sample and the focus of the pump beam are well aligned.

The reason for using the polarising filters together— Glan-Taylor and PBS1 —is to input infrared used in the imaging system, as well as being able to check the intensity of the pump laser and the position of the cavity in the process of aligning the source. When using only PBS1, the pump laser passes through PBS1 and has H-polarisation, and the H-polarised backlight is reflected from PBS1 and shared onto the cavity. Since the polarisation directions of these two beams are perpendicular to each other, the pump laser cannot be seen at the maximum brightness of the backlight.

Single–photon collection

The single–photons in our system are due to spontaneous emission in the QD inside the cryostat and are then coupled via a single-mode fibre. Note that, with the Purcell effect, the majority of single photons are emitted through the top surface of the micropillar cavities (65%: the photon extraction under non–resonance excitation, 16%: polarised brightness in the first lens under resonance excitation. More details about the source property are in Ref. [1]). The rest of the single photons are absorbed or emitted via the sides of the pillars.

Figure 3.5 a) shows the beam path for single photon collection. A single photon emitted from the top of the micropillar cavity surrounding the QD passes through the glass window of the stage cover inside the cryostat (transmittance: 99.0$\pm$ 0.3%). It then passes the stage cover through an external glass window on top of the cryostat vacuum chamber (transmittance 97.0$\pm$ 0.3%). The single photon that exits the cryostat passes through the objective lens, HWP4, QWP, and PBS2 in order. Then, the single-photon is coupled to a single-mode optical fibre through a telescope (beam reducer). The beam diameter of a single-photon after passing through PBS2 in free space is 4.25 $\pm$ 0.05mm. The beam diameter passing through the telescope (beam reducer) in the collection path is 2.10$\pm$ 0.05mm.

Single photons coupled to single-mode fibre are detected by connecting to an Avalanche Photo-Diode (APD) single photon detector or a Superconducting Nanowire Single-Photon Detector (SNSPD) (Commercially available SNSPDs are often niobium nitride-based, but in our model, the material is not specified due to commercial secrecy) [1]. At very low temperatures, the metal turns into a superconducting material, and as a benefit of its properties, the cooling time it takes to cool back to its original state after it absorbs photons is remarkably short ($<$100 ps). SNSPDs are the fastest single photon

[1] Such detectors were developed only about 20 years ago by Gol'tsman *et al* [55, 56], along with energy decomposition superconducting detectors operating at temperatures close to absolute zero— the transition edge sensor (TES) [57]; the superconducting tunnel junction (STJ) [58]; and the kinetic inductance detector (KID) [59].

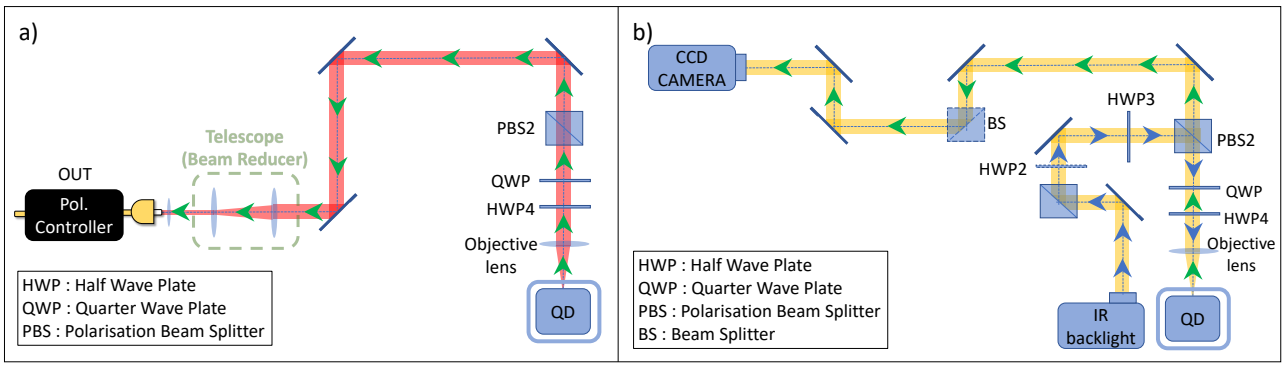


Figure 3.5: Single-photon collection and the imaging system. a) Single–photon collection. The single photons emitted to the top of the QD-micropillar structure pass through the cryostat glass windows and the objective lens. The photons are randomly polarised: therefore at most half pass through PBS2. A beam reducer is used to couple the photons into the single-mode fibre. b) Sample–imaging system. An IR backlight source that emits infrared light and a CCD camera that detects the image of the sample is installed, which are used for spatial alignment of the pump laser's focusing position and the micropillar cavity. The QD chip holder supporting the sample can be controlled in 3 axes (x, y, and z-axis), and the image on the top of the micropillar must be visible in the process of controlling its position. The removable BS is installed on a magnetic stand and is used only when imaging is required.

detectors. In addition, since it has a high detection rate and low dark count rate, it provides much more efficient and accurate single photon detection compared to commonly used APDs. A detailed review of SNSPD is provided in Ref. [60].

Note that due to the rejection of photons polarised orthogonally to the collecting mode, using a cavity with small birefringence in a cross-polarisation arrangement limits the first lens and fibre brightness to 50% maximum [61], but it can be overcome using polarised cavities ($\sim 65\%$) [62]. Also, the trion and exciton occupation probabilities further affect the average first lens brightness. It is mentioned that in Ref.[61], in a cross-polarised arrangement with almost degenerate cavity modes, they predict a maximum first lens brightness of 32% for their devices with a cavity extraction efficiency of 65% and a large enough numerical aperture. Trion-based sources with perfect control over occupation probability should be able to go close to this 32% limit. Bright exciton-based sources, on the other hand, necessitate a close to 45° angle between the cavity polarisation axis of V and the dipole orientation of the eigenstate $|V'\rangle$, as well as a substantial fine-structure splitting (FSS) to approach the 32% brightness limit.

Note that this out-coupling process is the most important step in determining the brightness of the source. Even if the source itself has good brightness, the source brightness is not good if the power loss of the acquisition process (including all mirrors and lenses in the acquisition path) is high or fibre coupling efficiency is low. Finally, the detection efficiency of the single photon detector also affects the brightness measurement.

Sample–imaging system

Spatial alignment between the target micropillars and the pump laser beam essentially requires an imaging system that allows direct viewing of the micropillars. In controlling the three-axis (x, y, z-axis) transformation stage supporting the sample, it is necessary to align the image on the top of the micropillar to obtain a sharp-clear image of our sample. This imaging system is in a position that overlaps with all three paths of source alignment (pump–beam preparation, QD–source excitation, and single–photon collection), so that can help the alignment of the source.

Figure 3.5 b) shows the beam path of the sample imaging system. Prepare an LED light source (940L3M00559297, Thorlabs) that emits infrared rays in cooperation with an LED driver (LEDD1B M00566913, Thorlabs). This IR backlight travels in a nearly planar waveform and is focused on the top of the micropillar through an objective lens to illuminate the sample. The IR backlight reflected from the sample surface passes through the objective lens again and then through HWP4 and QWP. The IR backlight passes through the PBS2, reflects onto a removable BS (mounted on a magnetic stand and used only when imaging is required), and is collected by a CCD camera (USB2.0 digital camera D1024G13C, Thorlabs). Meanwhile, the pump laser is also collimated to allow a larger beam waist via a beam expander and focused onto the top of the micropillar via an objective lens. Therefore, obtaining a clear image of the sample means that the pump laser beam being observed at that moment is almost focused on the top surface of the micropillar.

Chapter 4

Manually Improving Quantum Dot Single Photon Sources

This chapter introduces various methods to improve the performance of QD single-photon sources and the quality of the single photons. First, we employ a spectral pulse shaping setup to reduce the spectral bandwidth of the pulsed pump laser, resulting in the suppression of multi-photons and increasing the single-photon indistinguishability. Our spectral pulse shaper uses a spatial light modulator (SLM) as an essential component to demonstrate programmable spectral pulse formation. And then, we discuss its principles, pros and cons, and limitations. Second, we employ a programmable deformable mirror to improve the source brightness by improving the collection efficiency of single photons into the single-mode fibre. Lastly, we introduce the optical pulse multiplexing setup to increase the repetition rate (RR) of the pulsed pump laser, ultimately increasing the count rate of single photons generated from the source. Additionally, different excitation methods are introduced and demonstrated. The pros and cons of each method are discussed.

4.1 Suppressing multi-photon generation

One of the criteria for judging the quality of a single-photon source is the single-photon purity, that is how many multi–photon emissions are present in each pulse output, as discussed in Chapter 2. Low multi–photon emission is necessary to perform a series of experiments, including boson sampling [63, 64], as well as to develop high–performance optical quantum information processing technologies. For instance, quantum key distribution (QKD) between satellite and ground [65], QKD using entangled photons generated by QDs [66] and optical quantum computing [67].

When the QDs are excited by laser pulses at intervals longer than the spontaneous emission decay time and with intensities below saturation, the likelihood of producing multi–photon emission is extremely low. In this case, the major source of multi–photon noise comes from the laser itself. Achieving high multi–photon suppression thus requires minimising the scattering of the laser into the single–photon mode. In particular, if we employ resonant excitation, where QD emission and the

pump laser have the same wavelength, removing the laser background requires polarisation filtering, which leads to a reduction in the source brightness [68]. One way to reduce laser backscattering is to employ an excitation laser pulse with bandwidth matching the micropillar resonator.

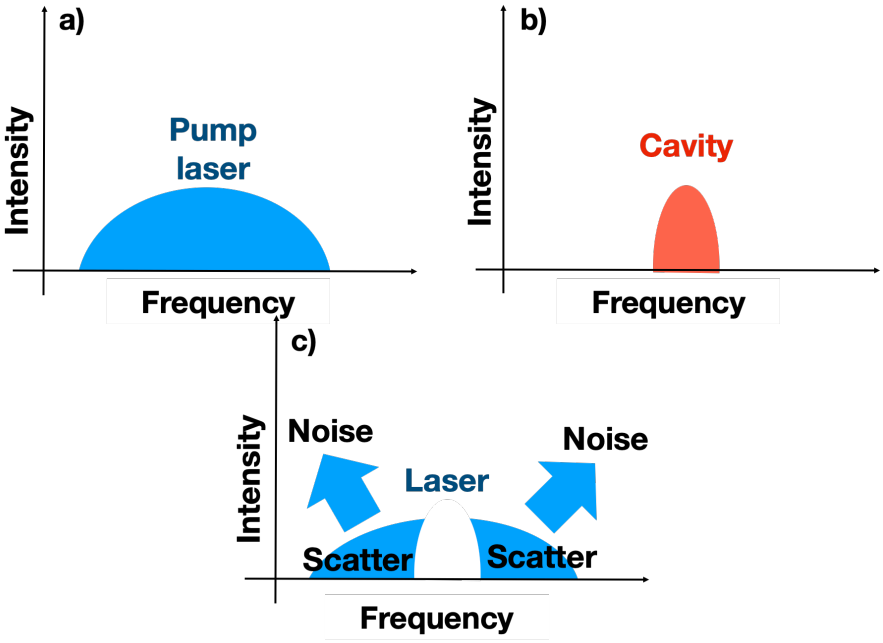


Figure 4.1: Spectral mismatch between pulse-pump laser and cavity mode: a) The blue region represents the spectral profile of the pulse-pump laser. b) The red area represents the spectral profile of the cavity mode. c) The two separated blue regions represent the spectral profile of a pulsed pump laser uncoupled from the cavity mode. When there is a spectral mismatch between the pump and the cavity, we have a large noise source due to backscattering. This is an undesirable additional noise source, considering we need to remove the pump laser from the single-photon signal. This noise affects the performance of the source, in particular single-photon purity and indistinguishability ($g^{(2)}(0)$ and HOM visibility).

Figure 4.1. shows the problem in our pump scheme, spectral mismatching between the pulse pump laser and the cavity mode. The problem is that the lasers available in the QTLab have a ∼88GHz bandwidth (∼5ps) as depicted in Figure 4.1 a). In contrast, the micropillar resonators surrounding the QDs have, ∼22GHz bandwidth as depicted in Figure 4.1 b). Any light outside this range is therefore scattered by the pillar as depicted in Figure 4.1 c). We can obtain laser pulses matching the micropillar's spectrum by employing a technique called frequency pulse shaping. In detail, we modulate (or shape) the spectral profile of a laser pulse using a diffraction grating and a phase and/or amplitude mask. Also, this procedure makes better use of the excitation laser power. Although the polarised filter removes a large fraction of laser scattering, if we need to increase the pump power to obtain better coupling we will eventually start to see laser noise.

4.1.1 Spectral pulse-shaping

Optical pulse shaping has been used in many areas, the most notable application is chirped pulse amplification, introduced in mid mid-1980s which awarded Donna Strickland and Gérard Mourou

the Nobel Prize for Physics in 2018. Their work demonstrated how to obtain high-intensity ultrafast laser pulses with the help of pulse shaping techniques [69].

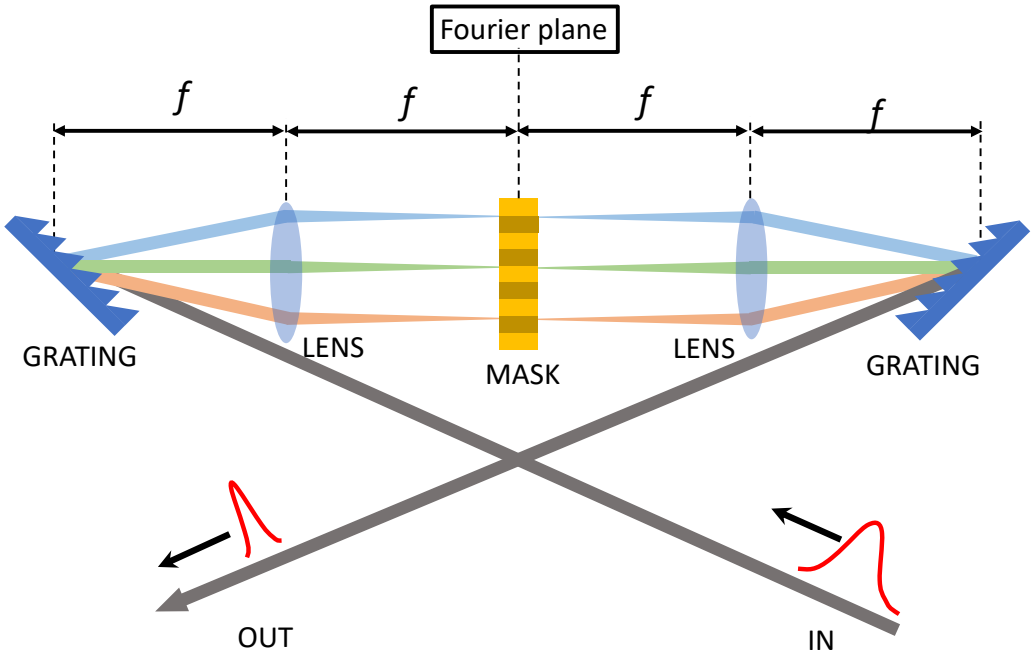


Figure 4.2: A typical ultra-short pulse-shaping setup. This setup consists of two lenses of the same focal length, two diffraction gratings and a mask. The distance between the first grating and the second grating is four times the focal length. The pulse's Fourier spectrum can be modified by spatially patterned amplitude and phase masks.

Figure 4.2 shows a typical ultrashort pulse shaping setup that uses two lenses of the same focal length, with the distance between the first and second gratings being four times the focal length. The principle of modulation of the pulsed laser spectrum in this setup is the following. A well-collimated pulsed laser with a broad spectral spectrum enters the first diffraction grating. This diffraction grating diffracts the incident pulse laser. In general, the grating equation is known as,

$$n\lambda = d(sin\theta + sin\theta'), \tag{4.1}$$

where n is the order of diffraction, λ is the diffracted wavelength, d is the grating constant (the distance between grooves), θ is the angle of incidence measured from the normal and θ' is the angle of diffraction measured from the normal. One of the higher-order beams diffracted from the first grating is selected to pass through the first lens. For a variety of higher-order beams diffracted by a grating and spread out in space, the frequency components are broadly distributed as the mode order increases, but the power drops sharply as a trade-off. One higher-order beam passing through the first lens is focused at the mask location (Fourier plane). Depending on how to apply a mask (amplitude mask, phase mask, or both), the spectral shape of the laser pulses can be modified. Then, the modified pulsed beam passes through a second lens— which is identical to the first lens and is then recombined at the surface of a second diffraction grating—which is identical to the first diffraction grating. Then all the frequency components are recombined and are coupled to the collection output. More Detailed

explanation of the settings for the optical pulse shaper according to the 4–f configuration can be found in Ref. [70, 71].

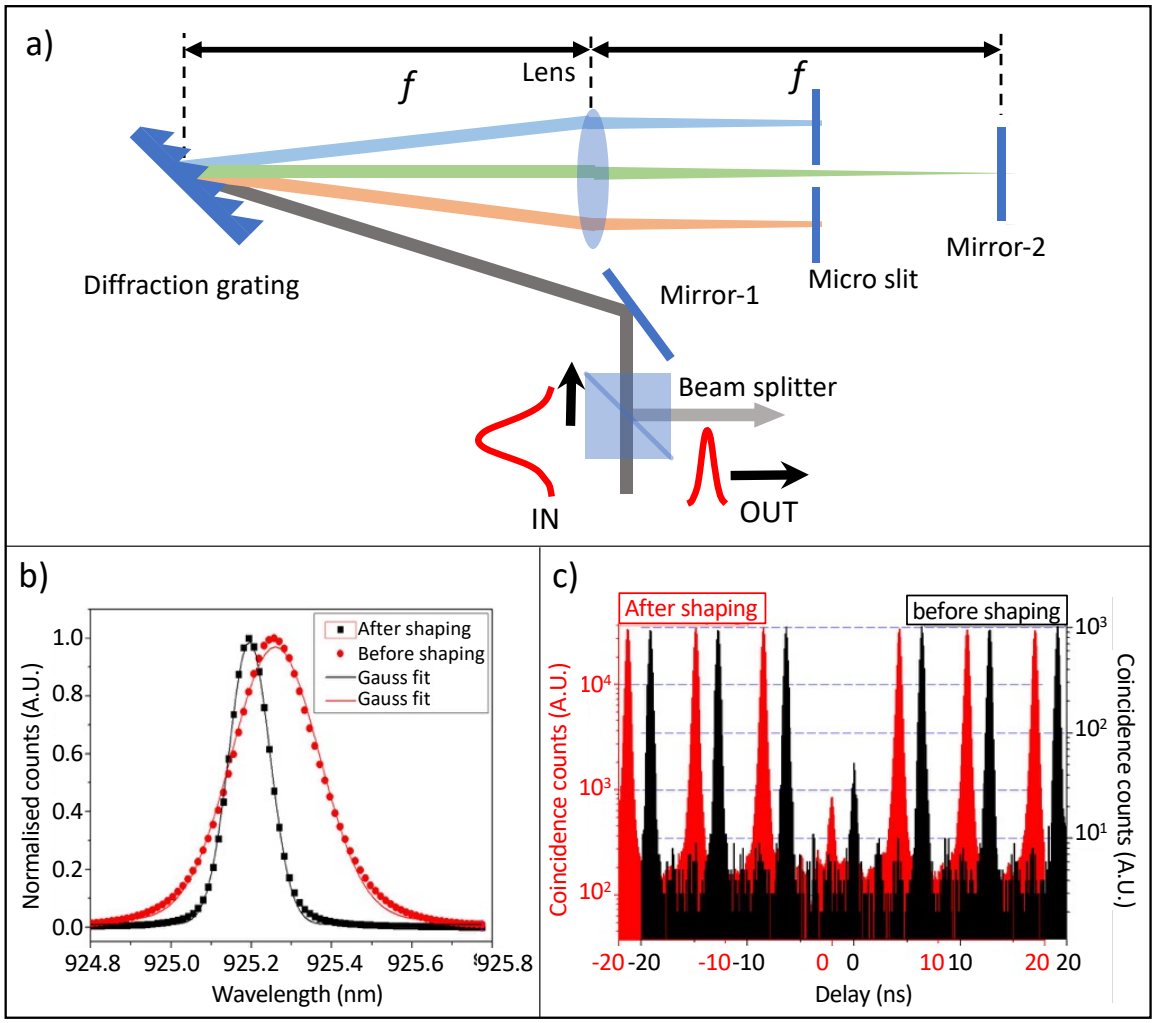


Figure 4.3: Preliminary pulse laser spectrum shaping by using a micro–slit. a) Conceptual drawing of the spectral pulse laser shaping set-up using a micro-slit. A well-collimated 3ps tsunami-pulse laser is passed through a 50:50 beam splitter, is reflected at Mirror-1, and then is diffracted by the diffraction grating. The diffracted beam from the diffraction grating is scattered into various orders, and then, one of the orders is collimated through the lens and reaches Mirror-2 placed at the mask position. The most of spectral components of the collimated beam after the lens are filtered at the micro-slit which is located between the lens and the second mirror. The reflected beam from the second mirror returns to the diffraction grating and is diffracted again to return to the beam splitter. b) Excitation laser spectrum before (circles) and after (squares) pulse shaping. The spectral bandwidth of the pulsed pump laser is reduced from 0.26 $\pm$ 0.005nm to 0.120 $\pm$0.005nm—(about 54% reduction). c) Comparison of second-order correlations for the single photons between before (black) and after (red) the pulse shaping, $g^2(0) = 0.033 \pm 0.001$ (without pulse shaping) and $g^2(0) = 0.018 \pm 0.01$ (after pulse shaping) are recorded—(about 45% reduction). Avalanche Photo-Diodes (APDs) are used to count single photons and a time tag module is used for the coincidence counts between two detectors.

To preliminarily test this idea, we consider a folded configuration pulse shaper setup. Our approach has two main effects. 1. Space efficiency: Our setup reduces space by 50% compared to the Shaper setup following the 4-f configuration presented in the original. 2. Fewer optics: Our setup

reduces by 50% the number of optics needed to create a shaper setup that closely follows the original 4-f configuration.

Figure 4.3 a) shows a conceptual drawing of the spectral pulse laser shaping setup using a micro-slit. This setup consists of a single micro–slit (VA100/M, Thorlabs) and a diffraction grating (Echelle Gratings GE2550-0363, Thorlabs). A well-collimated 3ps tsunami-pulse laser is passed through a 50:50 beam splitter, is reflected at Mirror-1, and then is diffracted by the diffraction grating. The diffracted beam from the diffraction grating is scattered into various orders, and then, one of the orders is collimated through the lens and reaches Mirror-2 placed at the mask position. The most of spectral components of the collimated beam after the lens are filtered at the micro-slit which is located between the lens and the second mirror. The reflected beam from the second mirror returns to the diffraction grating and is diffracted again to return to the beam splitter.

Figure 4.3 b) shows the reduction of the bandwidth of the pulsed pump laser (from the full-width-half-maximum (FWHM) 0.260 ± 0.005nm to FWHM 0.120 ± 0.005nm by employing this setup), the red circles are the spectral profile of the pulsed pump laser before using the pulse–shaping, the black squares are the spectral profile of the pulsed pump laser after the pulse–shaping. Note that the spectral profile shown here is taken with the default software setting (1800Grooves/mm, not specified angle) of the spectrometer (CCD camera: Andor iDus 401 series, Oxford Instrument), the value that we read on the spectrometer may be slightly mismatched with the theoretical value, we expect $\sim$88GHz and we measure $\sim$91.1GHz. This modulated pump pulse is used to excite our QD single-photon source.

Figure 4.3 c) shows the $g^2(0)$ value comparison between the before and after pulse shaping. Generated photons are collected via single-mode fibre. The resonant frequency emission spectrum of the QD is measured after exciting the QD by using this narrowed pulsed pump laser, finding FWHM of 0.065 ± 0.005nm. $g^2(0)$ is measured by using the Hanburry Brown and Twiss setup— using 50:50 fibre beam splitter (FBS) is used —the results is shown in $g^2(0)$ value of our QD source is reduced from 0.033 ± 0.001 to 0.018 ± 0.001, leading to better multi–photon suppression.

However, there are some problems caused by the array of pulse shaper which does not follow the exact 4–f configuration. The location of the second mirror is in the Fourier plane, but the location of the micro–slit that acts as an amplitude mask is not itself in the Fourier plane. Therefore, fundamentally, the setup itself is not a process of 4–f pulse shaping collected by spatially spreading and transforming the distributed spectral elements and then recombining temporally again. Instead, this setup spreads spectral elements in space, and then the final spectral element is coupled into the single-mode fibre. In the process, it can be expected that the centre wavelength of the pulse laser obtained varies depending on the difference between the beam size and the lens size, and is shown in Figure 4.3 b). Additionally, if the configuration uses a 50:50 beam splitter in the beam path to extract the output beam, the modified pulse being collected loses three-quarters of its power.

Temporarily, the bandwidth of our pulse laser was converted to $\sim$55GHz (8ps) by replacing the Gires-Tournois Interferometer (GTI), a component in our laser system which ultimately defines the pulse temporal width [72]. Figure 4.4 shows the second-order correlation measurement of the single–photons obtained using the bandwidth $\sim$55GHz (8ps) pulsed laser as a pump. In this case, we

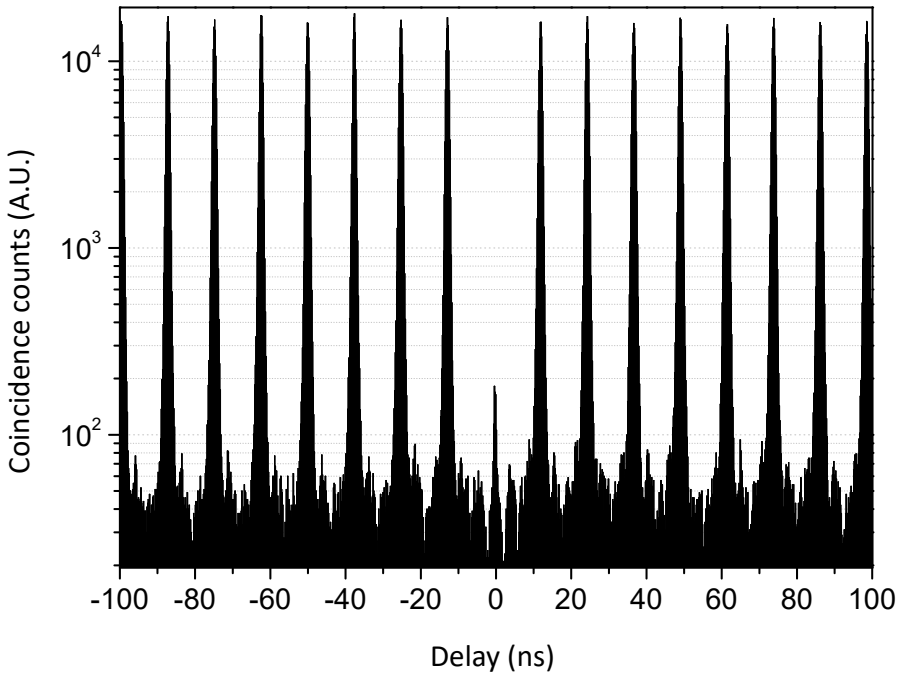


Figure 4.4: Second-order correlation measurement of the single–photons obtained using the bandwidth $\sim 55GHz$ (8ps) pulsed laser as a pump. $g^2(0) = 0.013 \pm 0.001$ is measured by resonantly excite the QD. Note that no spectral filtering and no background noise removal have been done in the single-photon collection path. Avalanche Photo-Diodes (APDs) are used to detect single photons, a time tag module is used for coincidence counts.

obtain the value of $g^{(2)}(0) = 0.013 \pm 0.001$.

Summarising the results in Figures 4.3 b) and 4.3 c), A narrow linewidth pulsed pump laser is manipulated to excite QD resonantly, it can reduce the bandwidth mismatching between the pulsed pump laser and the cavity mode of the QD-embedded micropillar. As a result, lowers the probability of multiphoton emission from the QD single-photon source by eliminating the dephasing.

We remark that spectral modulation of pulsed light by using spatial light modulators (SLMs) is not new. Revisiting the symmetrical shape 4-*f* configuration, the mask can be replaced by SLM. Note that "applying amplitude mask" means simply turning on/off a particular pixel on the window of SLM."applying phase mask" means how much voltage is applied on a particular pixel on the window of SLM so that the nematic liquid crystal molecules and be arranged in different configurations. It has been studied by using different types of SLMs— transparent [73, 74], reflective [75] —, adapting different types of experimental configurations of setups (symmetrical shape 4-*f* configuration, folded shape of 4-*f* configuration) to shape the spectrum of the pulsed laser. Particularly, for the folded shape of 4-*f* configuration, researchers began exploring methods for shaping femtosecond pulses in space and time using a two-dimensional SLM [76, 77] in the early 2000s, followed by a zero-order pulse shaping scheme was introduced and compared to the first-order scheme, using a liquid crystal on silicon 2D SLM in 2007 [75]. In their approach, the spectral components of the pulse are spread across the horizontal dimension, while the vertical direction is used to modulate both spectral phases and amplitudes, achieving better light efficiency— 67% —with the zero-order approach compared

to the first-order approach— 43% —, and the first-order scheme had a superior dynamic range of amplitude modulation. Based on the research results of previous researchers on spectral pulse shapers, we especially focus on deformation and tunability. Our idea introduces spectral modulation of pulsed light to optimise the spectrum for resonant excitation of QDs. We go further and attempt automatic optimisation through machine learning, eliminating the need for human assistance. We will discuss this in Chapter 5.

Figure 4.5 a) shows the modified setup configuration which does not use a 50:50 beam splitter and uses an SLM (LCOS-SLM x10468-03, Hamamatsu), to solve the issues— 1. 75% pump laser power reduction at the beam splitter, 2. Central wavelength mismatching between the before and after the shaping. At this time, the mirror at the mask position of 4-f configuration is replaced by the reflective SLM. The liquid crystal display window on the SLM consists of 480,000 pixels (800$\times$600 pixels). Incorporating re-configurable optical devices such as SLMs allows us to implement an active pulse–shaping setup. Note that this second attempt doesn't follow the exact 4–f configuration. Because we plan to spread the beam through the cylindrical lens as much as possible. If we select a spectrum with the narrowest bandwidth by turning on a specific pixel column in the SLM window, we can expect that the final collected pulse spectrum after using the pulse shaper will also be the narrowest. The modes created at the surface of the grating experience follow. Horizontally focuses the spread diffracted modes from grating to the particular point in the space. One of the higher-order beams is then collected using a plano-convex cylindrical lens (LJ1277L2-B, f=250.00mm, Thorlabs). The distance from the diffraction grating to the cylindrical lens is 90.0 $\pm$ 0.5cm, and the distance from the cylindrical lens to the SLM is 9.0 $\pm$ 0.5cm.

Here's how to utilise our SLM to create narrowband pump pulses: First, we form a vertical sawtooth pattern in the SLM window of our spectral pulse shaper. We then consider making the 16-pixel columns in the centre of the SLM window programmable. One thing to note here is that the diameter of the pump laser beam that closes the SLM window must be smaller than the width of the 16-pixel columns. Only the middle three vertical pixels of the 16-pixel columns are turned on, while the remaining pixel columns are turned off. The optical components are fine-tuned and aligned so that the middle pixel of the three vertical pixels matches the centre of the pump laser beam that on the SLM window. As a result, we get a narrowband pulsed pump laser.

Note that Figure number 4.5 a) shows the setup in a two-dimensional plane. It shows the beam exits the "4-f" line at a certain angle to the frequency dispersion axis. The difference between the incident and exit beams is the path of the beam, which has an angle in the vertical direction and an angle in the horizontal direction and is drawn on a two-dimensional plane. Several modes dispersing from the diffraction grating are distributed on a horizontal line. and then several modes distributed in the SLM window are distributed along a vertical line. To avoid overlap between the multiple modes distributed in the SLM window and the modes distributed in the diffraction grating, a vertical sawtooth pattern was formed in the SLM window, and displacement was applied in the vertical direction by tilting the SLM up and down.

Note that we estimate that the collected mode from the diffraction grating is the mode between

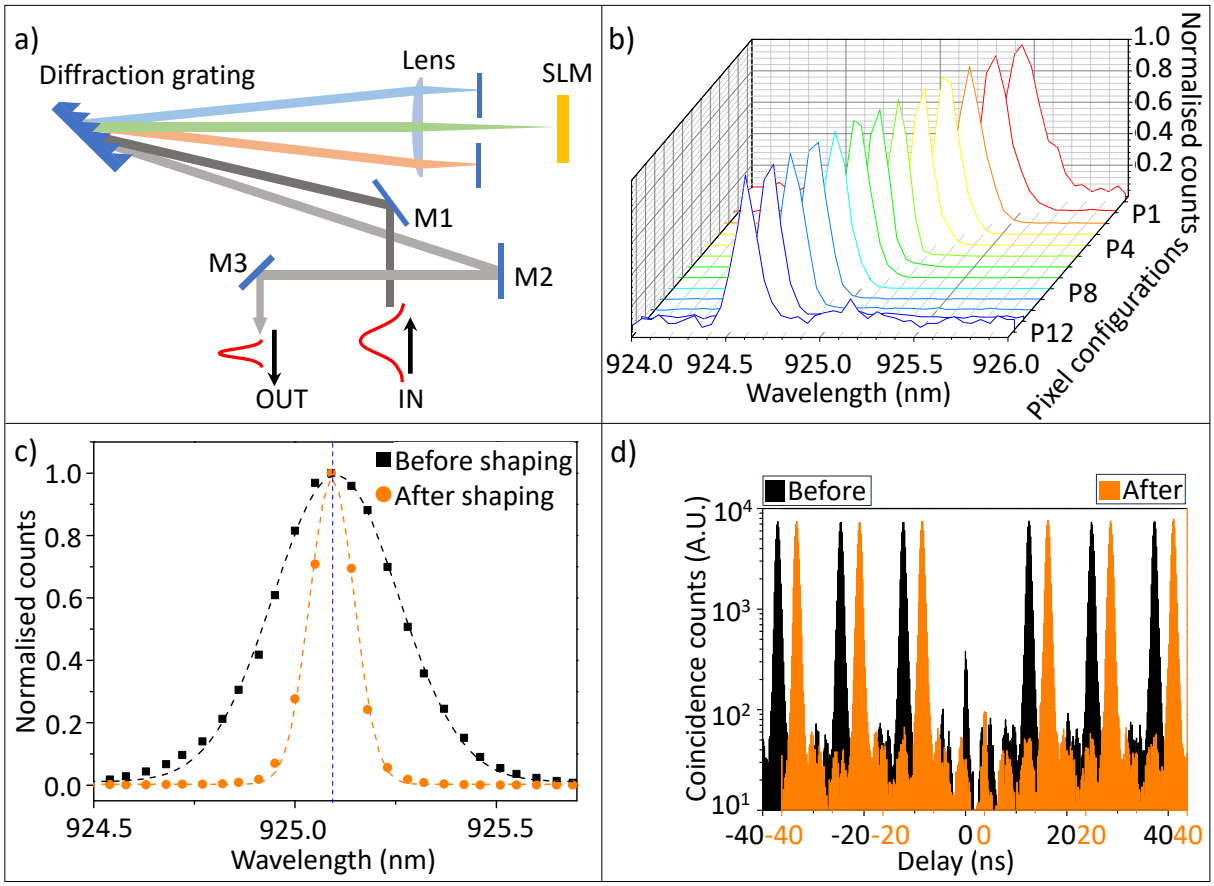


Figure 4.5: Pulse laser spectrum shaper employing an SLM (LCOS-SLM x10468-03, Hamamatsu). a) Conceptual drawing of the spectral pulse laser shaping setup employing an SLM. A collimated 3ps tsunami pulsed laser is reflected from the first mirror (M1), and then diffracted by the diffraction grating. One of the horizontally diffracted modes is focused through the cylindrical lens and then selected to reach the surface of the window on the spatial light modulator (SLM). The phase and amplitude of the liquid crystal material in the window can be programmed and adjusted, and are used to make a particular pattern, e.g. a sawtooth shape in the vertical direction. One of the vertically diffracted modes from the window of SLM is selected, is sent back to the grating, and then bounces back to the beam path which is similar to the entry beam path. This beam is coupled into the single-mode fibre through the second mirror (M2) and the third mirror (M3). Note that this setup doesn't follow the exact 4–f configuration. b) Spectral variability of the pulse shaper. The spectrally narrow pulsed pump laser is tuned while maintaining the spectral width of ∼0.14nm. The detuning range is 0.880 ±0.005nm (from 924.580 ± 0.005nm to 925.46 ± 0.005nm). c) Reduction of the spectral bandwidth of the pulsed pump laser. Before (black squares) and after (orange circles) pump pulse shaping are compared. The bandwidth is reduced from 0.360 ± 0.005nm to 0.13 ± 0.005nm (about 64 % reduction), and the blue dotted line represents the target spectrum line which is the QD transition line to emit single photons. d) Improving the purity of single photons. The second-order correlation function between the without pulse shaping (black) and after the pulse shaping (orange) are compared. $g^2(0)$ = 0.0202 ± 0.0004 (without pulse shaping) and 0.0068 ± 0.0004 (after pulse shaping) are measured—(about 66% reduction). Both $g^2(0)$ data were measured based on similar cumulative times. Note that these results are achieved without using an etalon–filter before the detector for the background correction. Avalanche Photo-Diodes (APDs) are used to detect single photons, and a time-tag module is used to measure the coincidence count.

65th and 75th. This is because the overlap between higher-order modes occurs in a very narrow two-dimensional cross-section, and it is impossible to distinguish the exact mode. Note that in the alignment process selecting a particular diffracted higher-order mode is extremely difficult because of the following reasons. First, hard to see the beam with the naked eye. Since the beam we align is the wavelength in the infrared region, an infrared-sensitive card has to be always accompanied to find the particular mode. Second, both requirements are met: the pulse pump obtained after spectral pulse shaping has a beam intensity sufficient to pump QDs and sufficient spatial spread of spectral elements in the high-order beam after the pulse pump laser is diffracted from the diffraction grating.

Note that there are two reasons for using a cylindrical lens instead of a general one in our spectral pulse shaper. First, the damage threshold of the SLM. When a general lens is used, the power of the pulsed laser is concentrated in a narrow area of the SLM window, which may cause damage to the liquid crystal material inside the device or the device itself. Second, horizontal focus on spectral components of the selected mode is only needed. Since the pattern on the window of SLM spreads the collected higher-order mode from the diffraction grating vertically, vertical focusing of the higher-order mode is not needed to contribute to actual modulation at the end. We cannot practically use a one-pixel column array on the SLM window as a pump source to excite the QD due to the low light diffracted. We require more than one-pixel column line arrays on the SLM window to secure sufficient output power, even if it results in a certain amount of bandwidth increase. Therefore, we use a three-pixel column line configuration to modulate a pulsed pump laser that satisfies both sufficient power and narrow bandwidth. This setup produces spectrally narrow pump pulses and can modulate the wavelength of the pulsed pump laser while keeping the bandwidth unchanged.

In our setup, the window of SLM consists of 480,000 pixels (800×600). Since a specific vertical pixel column can be turned on and off by a computer, we can select a specific spectrum by adjusting the number of pixel columns that are turned on to use it as a variable phase or amplitude mask. The SLM window can be used as an amplitude mask by turning on or off a specific pixel line. In experiments, entering a value of '0' or '1' in a particular line results in 'minimum amplitude' or 'maximum amplitude.' The voltage applied by the SLM driver to the same pixel line can change the reflectance of the nematic liquid crystal material between the two glass plates. It causes a phase difference between the spectral components of the pulsed laser that hits the SLM. In experiments, a value of '0' or '7' at the same specific pixel line— the line to which amplitude mask is applied —can achieve 'phase minimum' or 'phase maximum.' This programmable and flexible spectral modulation is not only the resonance transition of QDs that we focus on but can also be flexibly applied to realize other types of excitation methods.

Figure 4.5 b) shows the spectral controllability of this spectral pulse shaper. According to the code input, the three-pixel column lines— sawtooth patterned pixel columns in the vertical direction —on the screen of the SLM are gradually shifted in the direction perpendicular to the pixel column to select specific spectral elements. The variability of the pulse centre wavelength of our pulse shaper has a tremendous advantage in the optical resonance excitation of QD. The energy transition/single photon emission of QD we currently use shows a centre wavelength of 925.090 ± 0.005nm. A

single photon is generated at this central wavelength, and this value is in principle dominated by the size and material of the QD. Since QDs are artificially created atoms, not all QDs have the same size. Therefore, our pulse shaper can compensate for slightly different energy transitions caused by variations in the size of QD through its wavelength variability.

Figure 4.5 c) shows the comparison between before and after using the spectral pulse shaper. The narrowest spectral pump pulses are obtained by using a precise beam alignment in the pulse shaping protocol (single-mode fiber coupling efficiency at the output, rotation angle of the diffraction grating holder, and rotation angle of the SLM holder). Black squares represent the data without employing the pulse shaping protocol. Orange circles represent the data employing the shaping protocol. The spectral bandwidth is reduced from FWHM 0.360 $\pm$ 0.005nm to 0.130 $\pm$ 0.005nm. The default software setting (1800 Grooves/mm, not specified angle) of the spectrometer is the same setting as the preliminary setup.

Figure 4.5 d) shows $g^2(0)$ comparison between before and after using the spectral pulse shaper to check the performance of the spectral pulse shaper, $g^2(0)$ is measured to compare the original pulse laser and shaped pulse laser as an optical pump for the source, QD–33. The $g^2(0)$ measurement is performed as follows. First, we prepare single photons that are periodically generated and coupled to a single-mode optical fibre. These single photons are provided to one of the two input ports of the 50:50 fibre beam splitter. Connect the two output ports of this beam splitter to two single photon counters to detect single photons. The two counters are connected to the time tag module and measure events in which single photons are simultaneously detected between the two counters. Note that QD–33 is embedded in the micropillar–1 as shown in Figure. 3.1 d). $g^2(0)$ =0.0202 $\pm$ 0.0004 (without pulse shaping), 0.0068 $\pm$ 0.0004 (after pulse shaping) are measured.

Table 4.1 summarises and compares the $g^2(0)$ measurement among 7 different QD single-photon sources. We measure $g^2(0)$ for the source QD-33 with both APD and SNSPD. Our results are compared with the results of QD1, QD2, QD3, and QD4 in Ref. [1], the result of elliptical micropillar in Ref. [62], the result of elliptical bullseye in Ref. [62]. This result is remarkable, since the $g^2(0)$ reported in Ref. [1] which is the result from the same type of single–photon source (electrically controllable micropillar structure) is used to produce single–photons, $g^2(0)$ = 0.1241 $\pm$ 0.0007 (without etalon–filter) by using the sample QD3, $g^2(0)$ = 0.095 $\pm$ 0.004 by using the sample QD4 (without etalon–filter). From the same samples, $g^2(0)$ = 0.28 $\pm$ 0.12% (with etalon–filter) by using the sample QD3, $g^2(0)$ = 0.35 $\pm$ 0.4% (with etalon–filter) by using the sample QD4 has been reported. Note that Ref. [1] used 3GHz bandwidth etalon filter before detection. Ref. [62] used 5GHz bandwidth etalon filter before detection to remove the phonon sideband, which reduces the single photon count by $\sim$ 30% due to the filtering and the transmission rate of the etalon.

Figure 4.6 shows further investigates the performance of our spectral pulse shaper. $g^2(0)$ values of the single-photons are measured by using SNSPD, resulting in $g^2(0)$ = 0.0096 $\pm$ 0.0003 (without pulse shaping), 0.0026 $\pm$ 0.0002 (after pulse shaping), as shown in Since our SNSPD is located apart from where the QD single-photon source is, we used long single-mode fibres to connect them. Note that, in the calculation of $g^2(0)$ by using our SNSPD, removing the background noise from the data

		Without etalon	With etalon	Background correction	Detector
	source	$g^2(0)$	$g^2(0)$	—	—
This thesis	QD–33	0.0068 ± 0.0004	—	No	APD
	QD–33	0.0026 ± 0.0002	—-	No	SNSPD
Ref. [1] (2016)	QD1	—	0.024 ± 0.007	Yes	APD
	QD2	—	0.047 ± 0.009	Yes	APD
	QD3	0.1241 ± 0.007	0.0028 ± 0.0012	Yes	APD
	QD4	0.095 ± 0.004	0.0035 ± 0.0040	Yes	APD
Ref. [62] (2019)	elliptical micropillar	—	0.025 ± 0.005	Yes	SNSPD
Ref. [62] (2019)	elliptical bullseye	—	0.009 ± 0.003	Yes	SNSPD

Table 4.1: Comparison of $g^2(0)$ values among the QD single–photon sources. APD: Avalanche Photo-Diode, SNSPD: Superconducting Nanowire Single-Photon Detector. Our result of $g^2(0)$ measurement which doesn't use the etalon filter is nearly equivalent to other's results of $g^2(0)$ measurement which uses the etalon filter. This means our source is much brighter than any other QD single-photon source since there is no spectral filtering loss imposed by an etalon.

is not considered. Because our SNSPD is located 3 doors away from where the QD single-photon source is, a few fibre adapters for the single-mode fibre are used to deliver the single-photons from the QD source to the detector, a couple of back-reflections between the end tip of the single-mode fibres results in the background noise in the $g^2(0)$ measurement data histograms. However, the average height of the background noise count histograms is similar to the height of the coincidence counts at zero delay. While our result doesn't use an etalon filter on the collection path, still achieves the $g^2(0)$ value equivalent to the best-achieved result using an etalon filter by other groups shown in Table 4.1. This means our source is much brighter than any other source since no spectral filtering loss is imposed by an etalon in the collection path of single photons.

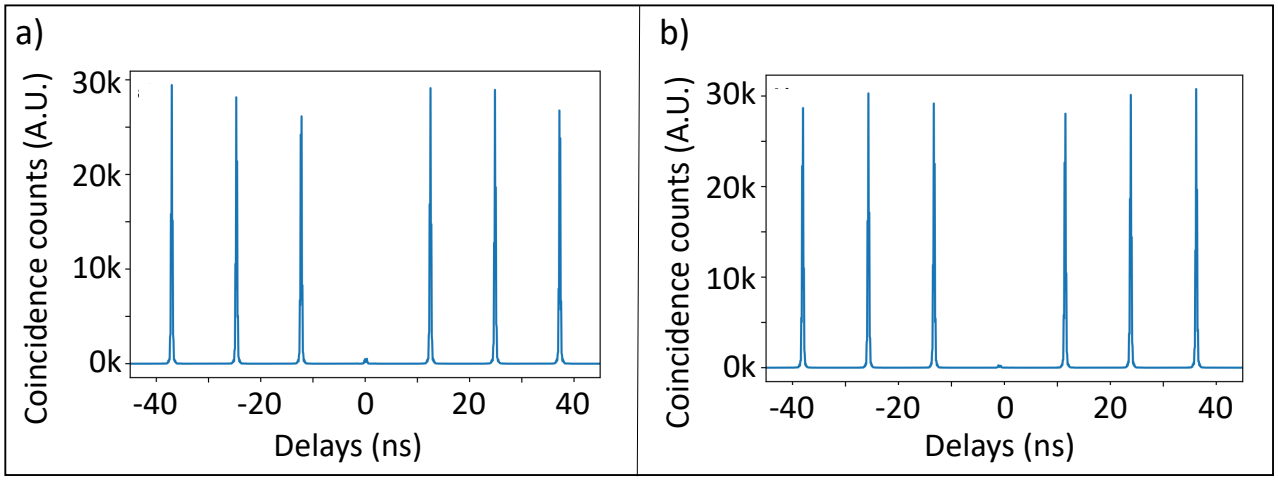


Figure 4.6: Second order correlation function measured with superconducting nanowire single-photon detector (SNSPD): a) Coincidence count histograms between the two detectors when the pulse shaping is not used, $g^2(0) = 0.0096 \pm 0.0003$. b) Coincidence count histograms between the two detectors when the pulse shaping is used, $g^2(0) = 0.0026 \pm 0.0002$. Any spectral filtering (etalon–filter) is not used, background noise correction is applied, for both results.

4.2 Improving single-photon indistinguishability

One of the criteria for judging the quality of a single-photon source is the single-photon indistinguishability—how every single photon generated sequentially is identical to each other—which is quantified by the Hong-Ou-Mandel (HOM) visibility, as discussed in Chapter 2. Photonic quantum circuits and photonic quantum computers require identical single photons to convey quantum bits—qubits—of information. It is very desirable to have a source that produces indistinguishable single–photons at the desired frequency.

A recent study [36], shows that improving the multi-photon suppression—and hence reducing background noise—improves the single photon indistinguishability. Recall that we employ resonant excitation, pumping the QD with a laser pulse tuned to the QD transition. This excitation method minimises the dephasing process in the QD since it doesn't require any additional time to relax the energy of an electron and consequently, the single photons created are nearly indistinguishable in frequency. Note that the drawback of resonant excitation is the laser and emitted photons have the same wavelength. Separating the QD emission from the laser background requires polarisation filtering, as described in Ref. [1] and in Chapter 2 of this thesis. Therefore, a dynamic pulse shaping described here can also enhance single-photon indistinguishability, as pulse shaping to match laser and cavity bandwidths consequently reduces back-scattering.

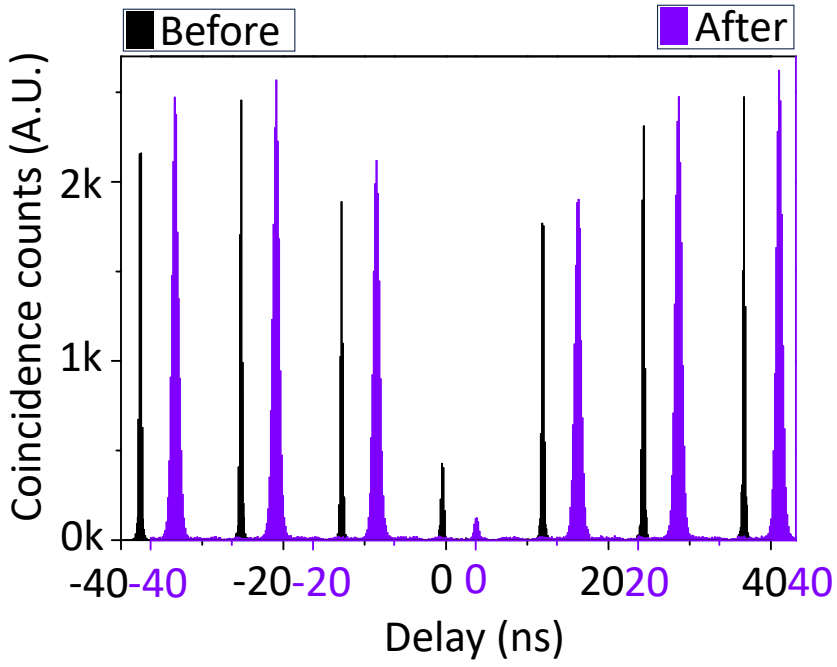


Figure 4.7: Two-photon interference single–photon coincidence counting histograms when pulse shaping is not used (black) and used (violet). HOM-visibility is 0.7291 ± 0.0024 (without pulse shaping), 0.9468 ± 0.0003 (after pulse shaping). Note that these results also don't use an etalon–filter on the single-photon collection path before the detector. Avalanche Photo-Diode (APD) single–photon detectors are used to measure the coincidence counts.

Figure 4.7 shows the HOM-visibility comparison between before and after using the spectral pulse

shaper. The pulsed pump laser is spectrally shaped by using the pulse shaper as shown in Figure 4.5 a). Narrow-band pulsed pump laser is used to excite the QD resonantly to generate single photons. Collected single photons are used to measure HOM–visibility by employing an unbalanced Mach-Zehnder interferometer. HOM-visibility 0.7291 $\pm$ 0.0024 (without pulse shaping). and 0.9468 $\pm$ 0.0003 (after manual pulse shaping) are recorded (30% increase of indistinguishability). Note that spectral filtering on the collection path of single photons before the SNSPD detectors is not used. However, background noise correction is applied for both results since the .

4.3 Pump–power characterisation

To efficiently drive a particular single-photon source (QD-33), it is handy to establish a systemised control of the pump power. In our system, we can adjust the intensity of the pump laser by rotating the polariser (Pol.1 in Figure 3.4). By knowing the relationship between the angle of the polariser and the resulting single-photon counts, we can optimise the single-photon counts for maximum effectiveness. This method saves time and ensures a more efficient use of resources.

Figure 4.8 a) shows the characterising the pump-laser power dependency of the QD–33 is performed by using the pump-beam preparation setup. Photodiode power sensor (S120C, Thorlab) connected with a digital optical power meter (PM100D, Thorlabs) is installed between Pol.1 and HWP1 in Figure 4.8 a), and the intensity of the pump laser is tuned by the rotation angle of Pol.1. Here, the polarisation direction before the pump laser reaches Pol.1 always has the same polarisation direction by using the Pol—controller at the beginning. Figure 4.8 b) shows the correlation between the polariser angle and laser power. The single photon count is measured using APD based on the properties of the system shown in Figure 4.8 b). Typically, the excitation path uses a pump power between 1nW and 1.5nW. Figure 4.8 b) shows that the intensity of the pump pulse laser changes depending on the rotation angle of Pol.1, and that the number of single photons collected is not linearly related to the intensity of the pulse laser.

4.4 Enhancing single-photon production rates

The brightness of the QD single-photon source is important as it allows faster information throughput, but achieving the higher brightness is challenging. On average, for example, one of seven pump pulses produces a single-photon in our system when we drive our source with a pulsed pump laser. Assuming that all the photons can be detected with unit efficiency, the 80MHz excitation laser pulse leads to a photon rate of about 11MHz. Further increasing the single–photon count rate is achievable by increasing the pump rate for the QD single-photon sources.

Figure 4.9 shows the temporal pulse multiplexing setup as a way to achieve higher pump rates. This setup can be used to increase the RR of the pulses in the temporal multiplexing scheme [78]. Using a PBS and a HWP allows us to tune the power distribution, an advantage over the 50:50 BS. In our system the amount of transmitted and reflected light in each port can be adjusted by using a HWP

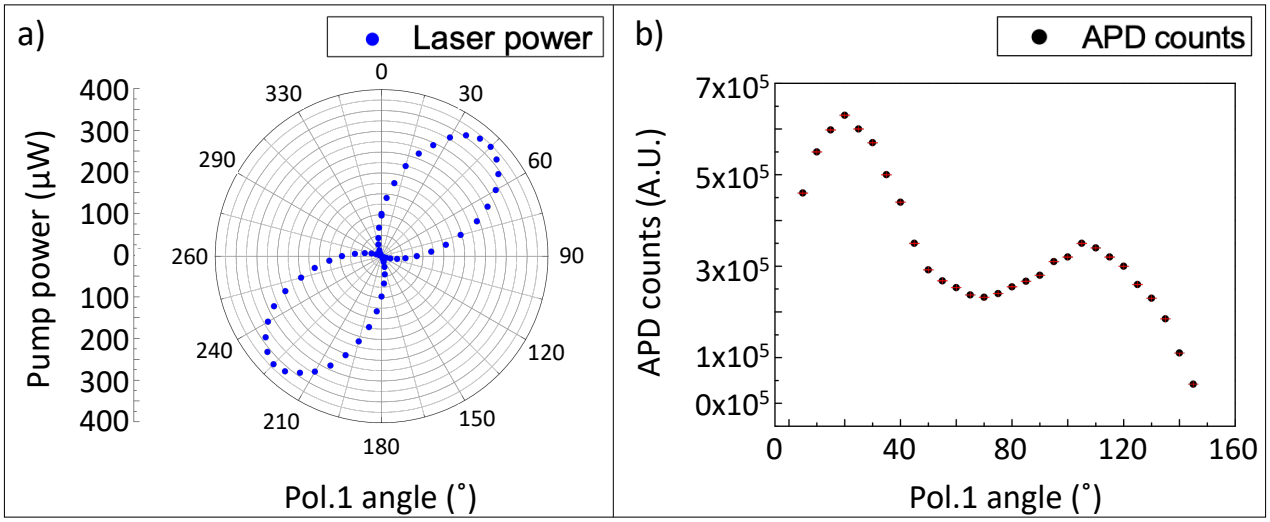


Figure 4.8: Correlation between pump-power and single–photon count–rate. a) Characteristics of pump power change according to the rotation of Pol.1 in the pump-beam preparation setup (Figure 3.4). We rotate the polarisation from 0 degrees to 360 degrees to characterise the maximum and the minimum pump power. b) Single–photon counts depend on the pump power (the rotation angle of the Pol.1 changes the pump power). Error bars are within the size range for each data point.

to set the effective splitting ratio at the next PBS. To briefly describe the process of multiplexing an applied pulse, we consider the RR of the initial pump pulse laser to be 80MHz; the intervals between pulses are 12.5ns. A pulse arrives at the first PBS and is separated into two paths, one of the separated pulses is delayed by 6.25ns and recombined with the other separated pulse at the second PBS. Pulse frequency has been doubled. We can further reduce the separation between the pulses by adding further appropriate delay lines. The setup shown in Figure 4.9 allows me to increase the original RR of the pump laser by a factor of 8. Lifetime decay was recorded under pulsed resonant excitation, extrapolated decay time ∼175ps. However, a complete emission— from the moment of starting emission to the zero-emission intensity —takes more than 1.2ns, as reported in Ref. [79]. Thus we are limited to pumping at RR $\geq$ 1.5ns to prevent re-excitation of the QD during its relaxation process. The inset graph of Figure 4.9 shows the doubling of the RR of the pulsed pump laser. This result shows evidence that our temporal pulse multiplexing setup has a promising potential to increase the production rate of the single photons from the QD single-photon source.

Increasing the rep-rate of pump pulses through the delay lines of Figure 4.9 has the advantage of reducing multi-photon emission by reducing the single pulse intensities while keeping the power high without incurring unwanted effects. In this sense, this can clearly be seen as a way to increase the brightness. Also, in this setup, achieving better coupling efficiency in the single-mode output fibre coupler allows the use of additional delays (3.12ns and 1.51ns) and exciting the QD single-photon source with more frequent cycles, resulting in a brighter single-photon source.

Note that this setup can be combined with a single-photon demultiplexing setup and applied to prepare input states for multichannel input/output optical circuits. Here, the demultiplexing setup is a passive process, a router consisting of PBS, HWP, and a delay line that takes time-spaced single

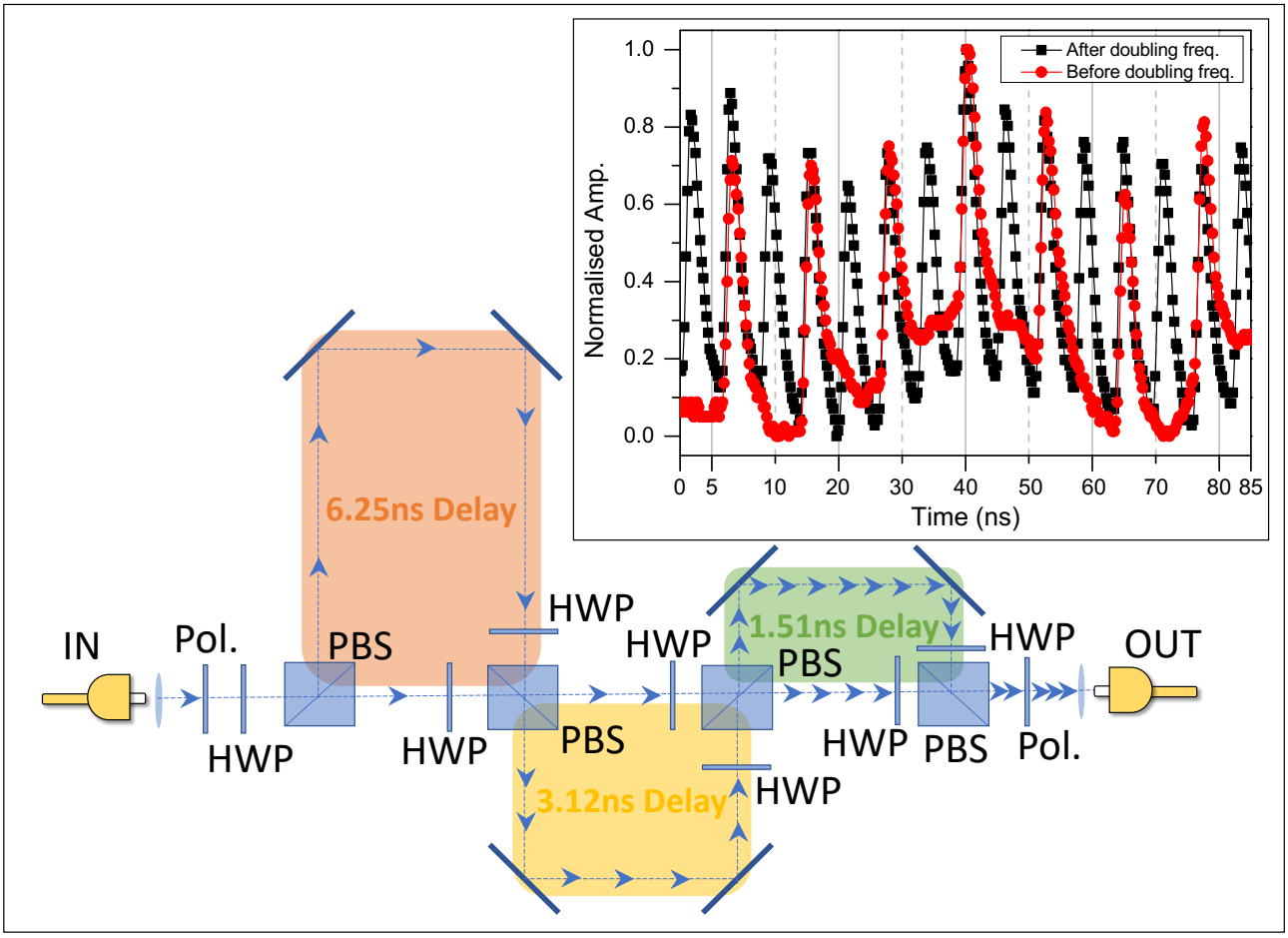


Figure 4.9: Temporal pulse multiplexing setup. The idea is adapted from Ref. [78]. The RR is increased by utilizing delay loops, where each delay decreases in length by 1/2 of the previous one. This design increases the RR by a factor of eight, while only decreasing the pulse intensity by half. The inset graph shows the RR doubling of Tsunami pulsed pump laser. Using a 6.25ns free space delay, the original 12.5ns (80MHz) RR was modulated to a 6.25ns (160MHz). Increase the iteration rate by using a delay loop where the length of each delay is halved compared to the previous delay.

photons as a single input and produces spatially separated single-photon outputs. Active demultiplexing can be achievable by using an electro-optical modulator (EOM) that provides sufficiently fast switching in the demultiplexing setup. A recent study [80] reported having eight demultiplexed single photons through active demultiplexing of single photons using a single EOM.

4.5 Different QD–excitation methods

In addition to the above band and resonant excitation introduced in Chapter 2, QD single-photon sources can be optically excited by other methods. For example, phonon-assisted excitation, or coherently driven two-colour excitation, has attracted attention in academia in recent years and has been actively studied. This section briefly introduces these methods and demonstrates them using our QD single-photon sources.

4.5.1 Phonon–assisted excitation

Phonon–assisted excitation of QD is an optical excitation method to excite the QD using a slightly detuned laser pumping from the resonance fluorescence wavelength [81, 82, 83, 84]. Since cross-polarisation filtering used in the resonant excitation is not required in this pump spectral region, a spectral filter can be used to remove the pump laser from the single-photon signal to improve the source brightness. During the duration of the excitation pulse, a strong occupancy of the excited state is obtained through adiabatic cooling mediated by the emission of longitudinal acoustic (LA) phonons. Through new theoretical studies [85, 83] after the first observation [86] of this phonon-assisted excitation, predicted that this excitation system should also provide almost unity single–photon purity, indistinguishability, and occupancy probability. This phonon-assisted excitation scheme with the use of a QD linear dipole was recently reported in Ref. [87].

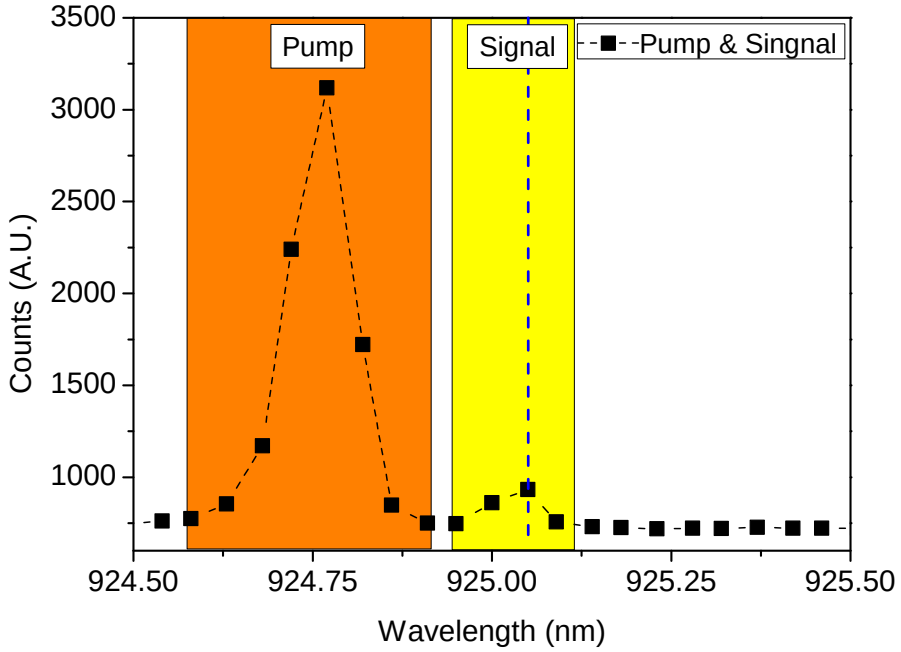


Figure 4.10: Phonon-assisted excitation of QD. A spectrally narrow–band pump pulse (centre wavelength 924.720 $\pm$ 0.005nm, FWHM 0.140 $\pm$ 0.005nm)—orange area—is created through the pulse shaper, used to excite the QD to obtain the resonant fluorescence signal)—yellow area—the pump and the resonant fluorescence signal together are shown (black squares). The vertical dotted line indicates the single photon emission wavelength.

Figure 4.10 shows the demonstration of the phonon–assisted excitation method by employing our spectral pump pulse shaper. We obtained a pulsed pump (central wavelength = 924.720 $\pm$ 0.005nm, bandwidth FWHM = 0.140 $\pm$ 0.005nm)through the spectral pulse shaping. With this modulated pulse pump laser, our QD single-photon source is driven to an exited state, a resonant fluorescence signal (central wavelength = 925.09 $\pm$ 0.005nm, bandwidth FWHM = 0.070 $\pm$ 0.005nm) is obtained.

Note that the excitation pump laser can be sufficiently removed by applying a band-pass filter centred at 925.09nm for collecting the single photons only. Note that this excitation method requires

increased pump power compared to resonance excitation, which increases the probability of multi-photon generation.

4.5.2 Two-colour excitation

The two-colour excitation method refers to an optical excitation method that produces a resonance excitation effect by precisely controlling the phase difference of dichroic lights detuned by $\pm\Delta\omega$ around the QD transition frequency; ω_T. We introduce a brief theoretical background of the experiment demonstrated by He *et al.* [88].

Figure 4.11 a) shows the concept of the coherent overlapping of two different colours of lasers, targeting the QD's energy transition in the centre, a blue-shifted pump laser and a red-shifted pump laser can be combined coherently to excite QD.

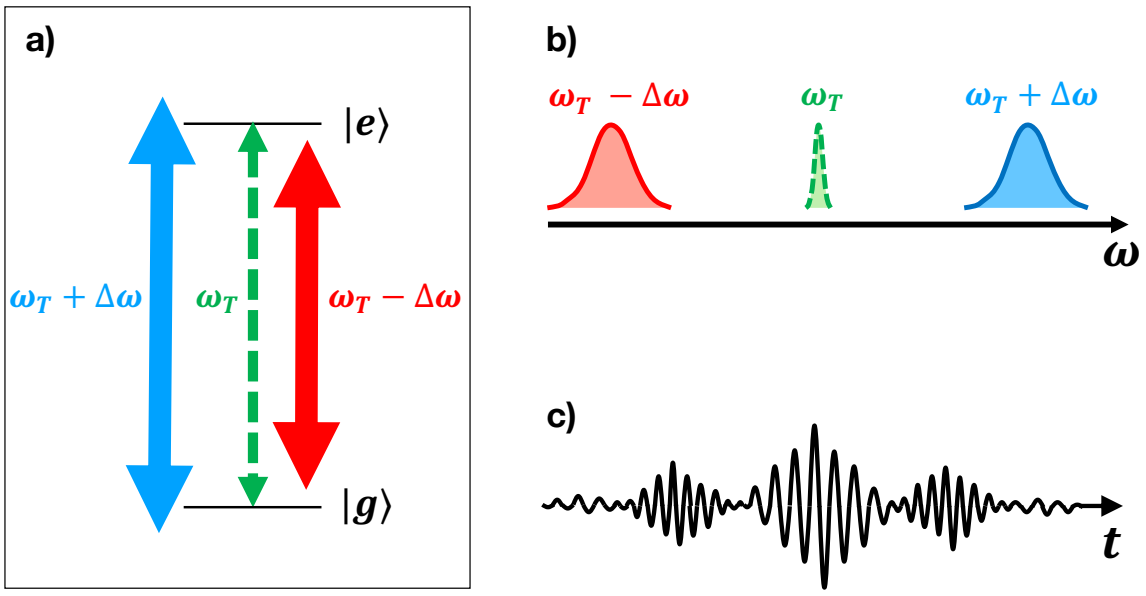


Figure 4.11: Concept of the coherent two-colour excitation method of a two-level system. a) the ground state: $|g\rangle$ and the excited state:$|e\rangle$ of the two-level system, the transition frequency between the two levels; ω_T. Relative energy diagram of two-colour pulses modulated by $\pm\Delta\omega$ beside ω_T. b) Distribution relationship between two-colour pulses and transition frequencies in the frequency domain. c) The shape of coherently combined two-color pulses in the time domain.

The sum of two-colour pulses modulated by $\pm\Delta\omega$ beside ω_T can be written as follow,

$$\frac{\varepsilon(t)}{2}\cos\left((\omega_T+\Delta\omega)t+\delta\phi\right)+\frac{\varepsilon(t)}{2}\cos\left((\omega_T-\Delta\omega)t\right) \tag{4.2}$$

$$=\varepsilon(t)\cos\left(\Delta\omega t+\frac{\delta\phi}{2}\right)\cos\left(\omega_T t+\frac{\delta\phi}{2}\right) \tag{4.3}$$

where, $\varepsilon(t)$ is the pulse envelope, $\delta\phi$ is a fixed phase difference. By effectively cancelling the detunes, we can consider a resonant pulse with a new envelope as follows,

$$E(t)=\varepsilon(t)\cos\left(\Delta\omega t+\frac{\delta\phi}{2}\right) \tag{4.4}$$

Note that this mathematical result can be expanded by considering the phonon effect, which can be found in Ref. [89]. They considered the Bloch equations on the x, y, and z axes and the parameter values considered in the Bloch vectors of the two-level system.

The strength of the signal in this excitation method is closely related to two things. One is how accurately the spectral spacing of a two-colour pump laser can be narrowed and widened, and the other is how artificially the phase difference between the two colours can be adjusted. We demonstrate this excitation method by using our spectral pulse shaper.

The preparation process of the pump pulse laser for two-colour excitation in Ref. [88] is divided into two main categories. The first step is to remove the middle part from the Gaussian spectral profile of the pulse pump by using the 4-*f* pulse shaping setup, but by installing a 'block' in the mask located in the Fourier–plane (Figure 2., Ref. [88]). In this process, two diffraction gratings, two identical lenses, and four mirrors are required to build a 4–*f* pulse shaper. Next, in the second step, phase control is performed using a Sagnac interferometer [90] for accurate phase control between the different two-colour pulse pump lasers (Figure 4 a., Ref. [88]). In this process, two bandpass filters, one phase shifter, three mirrors, and one beam splitter are required for each of the two colours.

This excitation method can be realized more efficiently using the programmable pulse shaper (Figure 4.5 a). This is because we use specific parameter control in Python code to control the spectral spacing of the two-colour pump laser by turning on and off specific liquid crystal pixels in the SLM window. The amplitude and phase of each pixel can be controlled independently, enabling coherently driven QD single-photon sources by adjusting the appropriate amplitude and phase of each pixel in the SLM window.

Here's how to utilise our SLM to create sideband pump pulses: First, we form a vertical sawtooth pattern in the SLM window of our spectral pulse shaper. We then consider making the 16-pixel columns in the centre of the SLM window programmable. One thing to note here is that the diameter of the pump laser beam that closes the SLM window must be smaller than the width of the 16-pixel columns. Similar to the method used to generate narrowband pulses, only the middle three vertical pixels of the 16-pixel columns are turned on, while the remaining pixel columns are turned off. The optical components are fine-tuned and aligned so that the middle pixel of the three vertical pixels matches the centre of the pump laser beam that closes the SLM window. Next, turn off the three vertical pixels in the middle, and turn on the 13-pixel rows on either side of the row, maintaining the sawtooth pattern. As a result, we get a pulsed pump laser with only the middle part of the Gaussian spectral shape having no spectrum.

For preliminary experiments, we apply different pixel combinations on the SLM window to create different peak-to-peak (the wavelength difference between the centre of two different spectral peaks on the blue side and the red side around the QD transition spectrum) separations of the two colours pulsed pump laser. Not that it is necessary to investigate how much the peak-to-peak interval of the sidebands can be adjusted by turning on/off specific pixels, and how much the noise level between the peaks changes according to the change in pump power. A pixel combination on the SLM window having a peak-to-peak interval of 0.410 ± 0.005nm was obtained around the QD transition wave-

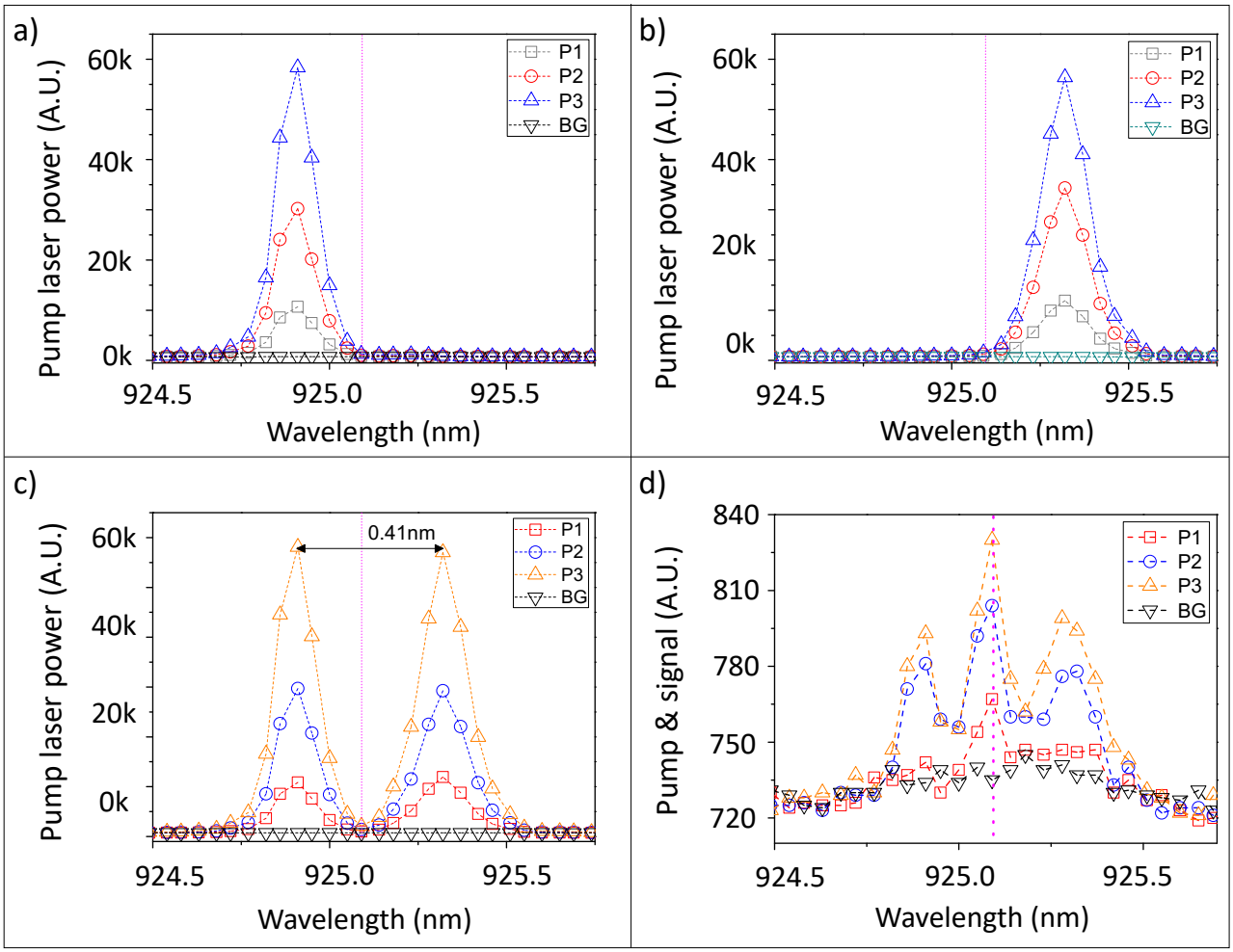


Figure 4.12: Spectral change according to the strength of the sidebands (the blue–to–red peak distance: 0.410 ± 0.005nm) pulse pump laser. The pink dotted lines indicate the central wavelength of single–photon emission. a) The spectrum of the longer wavelength side is removed by turning off specific pixels on the SLM window, leaving only the shorter wavelength side, and the pump power was changed to give 10k, 20k, 30k, and 65k based on the signal strength counted by the spectrometer, and compared with the background noise (BG). b) The spectrum of the short wavelength side is removed by turning off specific pixels on the SLM window, leaving only the long wavelength side, and the pump power was changed to give 10k, 20k, 30k, and 65k based on the signal strength counted by the spectrometer. c) Pump power dependency of the pulsed pump laser spectrum. The peak-to-peak separation between the two colours of the pulsed pump laser is 0.410 ± 0.005nm, pink dotted line indicates the resonant frequency d) Two-colour laser pulse pump and QD signal change with pump power. The pink dotted line indicates the position of the single photon emission wavelength 925.090 ± 0.005nm.

length. In this process, to more reliably remove the wavelength in the region between the peaks, a very thin wire was inserted vertically in front of the SLM window to further lower the background noise. Since the spectrometer is saturated with an input power of about 1nW, the pump power was attenuated to give 10k, 30k, and 65k based on the counts displayed by the spectrometer.

Figure 4.12 a) shows the spectrum variation of the blue–side pump laser depending on the pump power. Figure. 4.12 b) shows the spectrum variation of the red–side pulsed pump laser depending on the pump power. Figure 4.12 c) shows the spectrum variation of both sides together depending on the

pump power. Figure 4.12 d) shows the pulsed pump and resonant fluorescence together depending on the pump power. This test shows that the QD transition wavelength is not directly affected by the two sidebands within the pump power of the intensity enough to be saturated by the spectrometer.

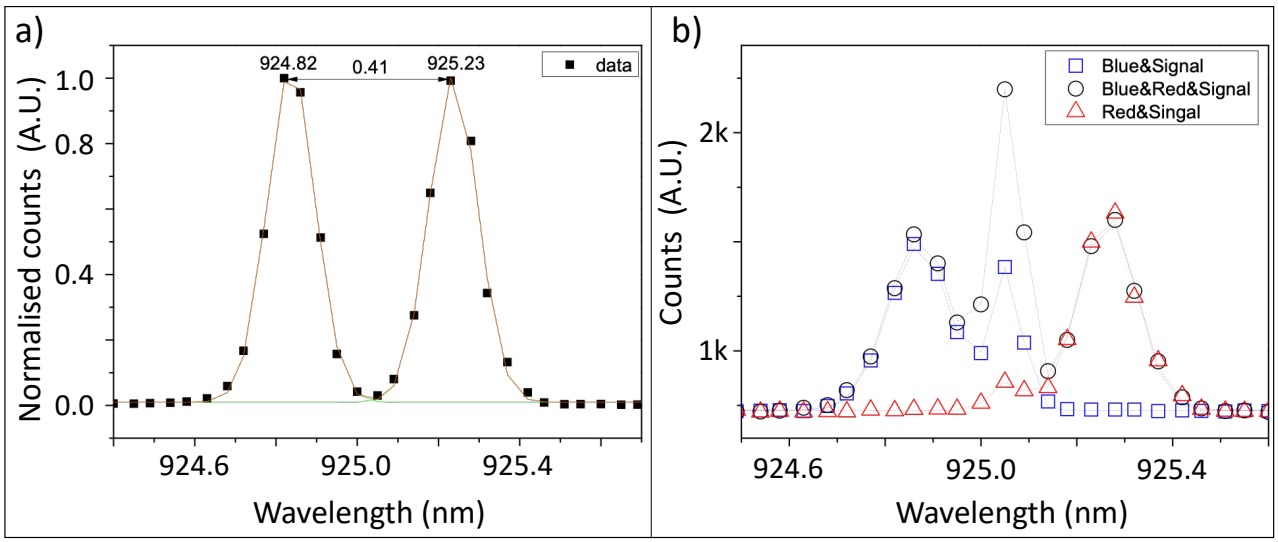


Figure 4.13: Near coherent driving QD with two-colour laser pulses. a) Spectral profile of a sideband pulse pump laser. Using the QD transition wavelength: 925.050 ± 0.005nm as a reference, two sideband excitation pump pulses are obtained which are separated 0.410 ± 0.005nm and are generated by simply turning off specific pixels in the pulse shaper's SLM window. b) Spectrum and resonance fluorescence (RF) of the two-colour pump. The peak wavelengths of the two-colour pump pulse lasers are separated by 0.410 ± 0.005nm based on the QD-atomic transition line. The blue-side pump and RF (blue squares), the red-side pump and RF (red triangles), the blue-side pump and the red-side pump together with RF signal (black circles).

Figure 4.13 a) shows the spectrum of two colour pulsed pump lasers manipulated by using our programmable spectral pulse shaper, the peak-to-peak of the spectrums are separated by 0.410 ± 0.005nm, centred at the resonant transition wavelength of the QD, 925.050 ± 0.005nm. The two-colour pumping method is demonstrated by the near-coherent combination of the two-colours of the pulsed pump laser. The amplitude and phase parameters of SLM pixels are manually combined by assigning specific values to the pixel array. It's not a perfect coherence, but it's enough to show the phenomenon of the coherently driven QD single-photon source by using a two-colour pulsed pump laser. In Figure. 4.13 b), we compare the spontaneous emission signal when each colour is applied individually to excite the QD and when the two colours are coherently applied to excite the QD. The measurement of the signal at the central wavelength of 925.050 ± 0.005nm where single photons are generated when only the blue-side pump laser is used can be understood as the phonon-assisted excitation (Figure 4.10). However, in Figure 4.13 b), a small signal is measured at the central wavelength of 925.050 ± 0.005nm where single–photons are detected when the red-side pump laser is solely applied to pump the QD. Note that ideally, it should not be any single-photon signal when the red-side pump laser is applied. In other words, some of the spectral components of the red-side pump pulse affect the QD excitation directly. Nevertheless, it can be seen that the two-colour excitation is

sufficiently reliable.

Note that the spectral spacing between the two colours can be completely separated by using metal wires of different thicknesses for more accurate blocking. In the pulse-shaping setup (Figure 4.5 a), blocking the intermediate region between the cylindrical lens and the SLM by installing thin metal wire vertically— the blocked area overlaps with the inactive pixels of the window of the SLM —helped to remove the central spectrum. The reason for this can be thought that the configuration (Figure 4.5 a) is not an exact 4-f configuration, the spectral elements radiating from the reflective grating do not propagate parallel to each other through the cylindrical lens. As a result, the spectral elements either converge or spread at some angle until they reach the SLM. Better quality results can be obtained by configuring the pulse shaper according to the exact 4-f configuration and attaining the non-overlapping spectral region between the QD-cavity mode and the bi-colour pulse pump laser

When the QD is excited by using only one colour, the signal of the pump laser is larger than the QD signal. However, the coherent combination of the two colours can create a much stronger QD signal. We remark that the condition to achieve this coherent combination between two different colours is found manual by simply changing the phase parameters of the SLM pixel with integer numbers, this combination is not such a precise phase matching condition to drive the QD coherently with two colours pulsed pump laser. Nevertheless, it clearly shows the phenomenon of the excitation of QD by using a near-coherent two-colour combination of pulsed pump laser. Suppose employing an appropriate band-pass filter and securing a precise phase matching between two colours of the pulsed pump laser, this excitation method can be used as an alternative way to drive the QD to achieve sufficiently high-quality deterministic single–photon sources. In addition, it is expected that machine learning can find the precise phase matching between the two sidebands since determining the phase parameter of each pixel on the window of SLM by humans is limited.

Figure 4.14 shows a further investigation to confirm whether the QD signal at the centre of the image in Figure 4.13 b) is the spontaneous emission. The idea is that while using the resonant two-colour excitation method for these QDs, we gradually apply an electric field to this QD externally, starting from 0V and going up to 1.9V, to observe changes in the spontaneous emission signal. Not that we limit the applicable voltage to less than 2V to prevent damage to our source. Remind that our QD single-photon source is coupled to a micropillar structure, and the top and bottom of this micropillar are connected to the outer voltage source that can supply an electrical bias. Figure 4.14 a) shows the evolution of the QD signal mixed with the two-colour pump laser when different voltages are applied from $\sim$0V to $\sim$1.9V. 20 different voltages— 0 ± 0.005, 0.104(5), 0.205(5), 0.305(5), 0.405(5), 0.504(5), 0.605(5), 0.705(5), 0.805(5), 0.905(5), 1.005(5), 1.105(5), 1.205(5), 1.305(5), 1.405(5), 1.505(5), 1.605(5), 1.705(5), 1.804(5), 1.905(5). As a result, it was observed that the wavelength of the central peak shifted from 925.05 $\pm$ 0.005nm to 925.12 $\pm$ 0.005nm, as shown in However, strictly speaking, it may not be considered as a perfect two-colour coherent excitation. Because the gap between the two peaks in Figure 4.13 a) might not be large enough to prevent overlapping with the bandwidth of the cavity.

Figure 4.15 shows a further investigation of the two-colour excitation method of QD when we

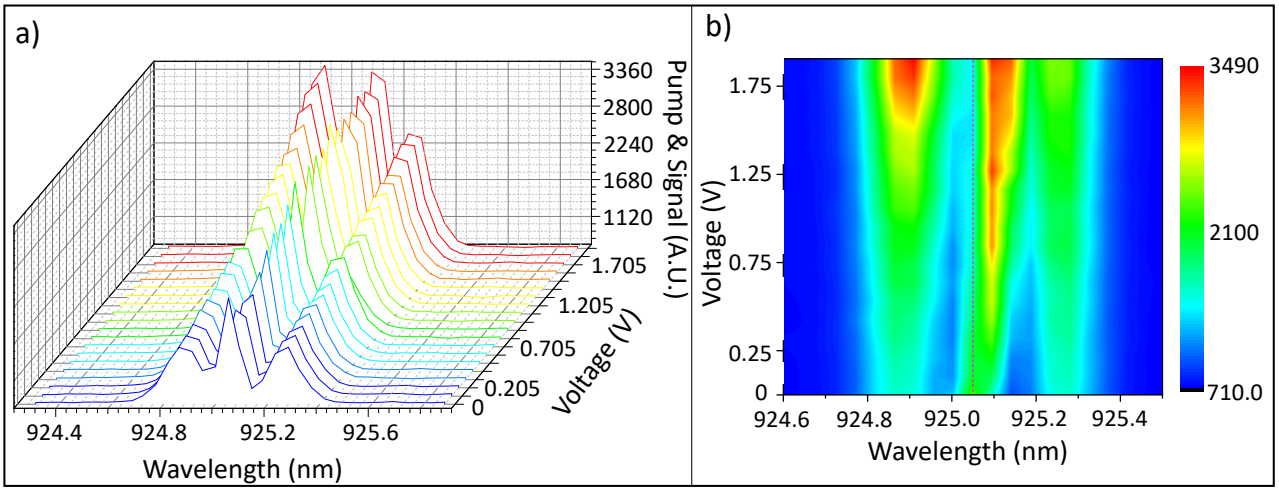


Figure 4.14: Evolution of the QD signal mixed with the two-colour pump laser when different voltages are applied. 20 different voltages— 0 ± 0.005, 0.104(5), 0.205(5), 0.305(5), 0.405(5), 0.504(5), 0.605(5), 0.705(5), 0.805(5), 0.905(5), 1.005(5), 1.105(5), 1.205(5), 1.305(5), 1.405(5), 1.505(5), 1.605(5), 1.705(5), 1.804(5), 1.905(5) —are applied to the cavity of the QD, consecutively. a) Red-shifting of the single-photon signal while driving QD with two-colour laser pulses when voltages are applied from 0V to 1.905V. b) Spectral profiles of the pump laser and QD signal when the QD is semi-coherent driven with two-colour laser pulses when voltages are applied from 0V to 1.905V. The emission signal peak shifts from 925.05 ± 0.005nm to 925.12 ± 0.005nm. A very thin dotted line in the middle of the image indicates the QD transition line when there is no electric field applied.

use the peak-to-peak distance 0.710 ± 0.005nm. This time we create the sideband pump pulses by turning on or off of particular pixel columns on the SLM window. A very thin metal wire is installed vertically at the position between the cylindrical lens and the SLM (in this case, we installed the thin metal wire closer to the SLM window to remove unwanted spectrum components. Figure 4.15 a) shows the spectrum variation of the blue–side pulsed pump laser depending on the pump power. Figure 4.15 b) shows the spectrum variation of the red–side pulsed pump laser depending on the pump power. Figure 4.15 c) shows the spectrum variation of both, red and blue sides pulsed pump laser depending on the pump power. Figure 4.15 d) shows the pulsed pump laser and resonant fluorescence together depending on the pump power. Driving QD resonantly with two colours by using the peak-to-peak separation between 0.710 ± 0.005nm doesn't show clear evidence of a coherent combination between the reside and the blue side of the pulsed pump laser. In Figure 4.15 d), the intensity of the resonant frequency signal decreases sharply, depending on the pump power of the laser, seems like the excitation of QD is mostly contributed by the blueside pump pulses. In addition, driving the QD with a coherent combination of two-colour pulsed pump lasers is much harder than the case of the peak-to-peak separation 0.410 ± 0.005nm. We assume that this is because the phase matching between the two colours is not precise enough, resulting in the faint single–photon signal using the combination of the two pump pulses. Again, as a way to achieve more precise coherent driving of the QD in the future, one of the solutions is to find the exact phase match between the two sidebands using machine learning. To realise this scenario, an appropriate bandpass filter is required to be installed in

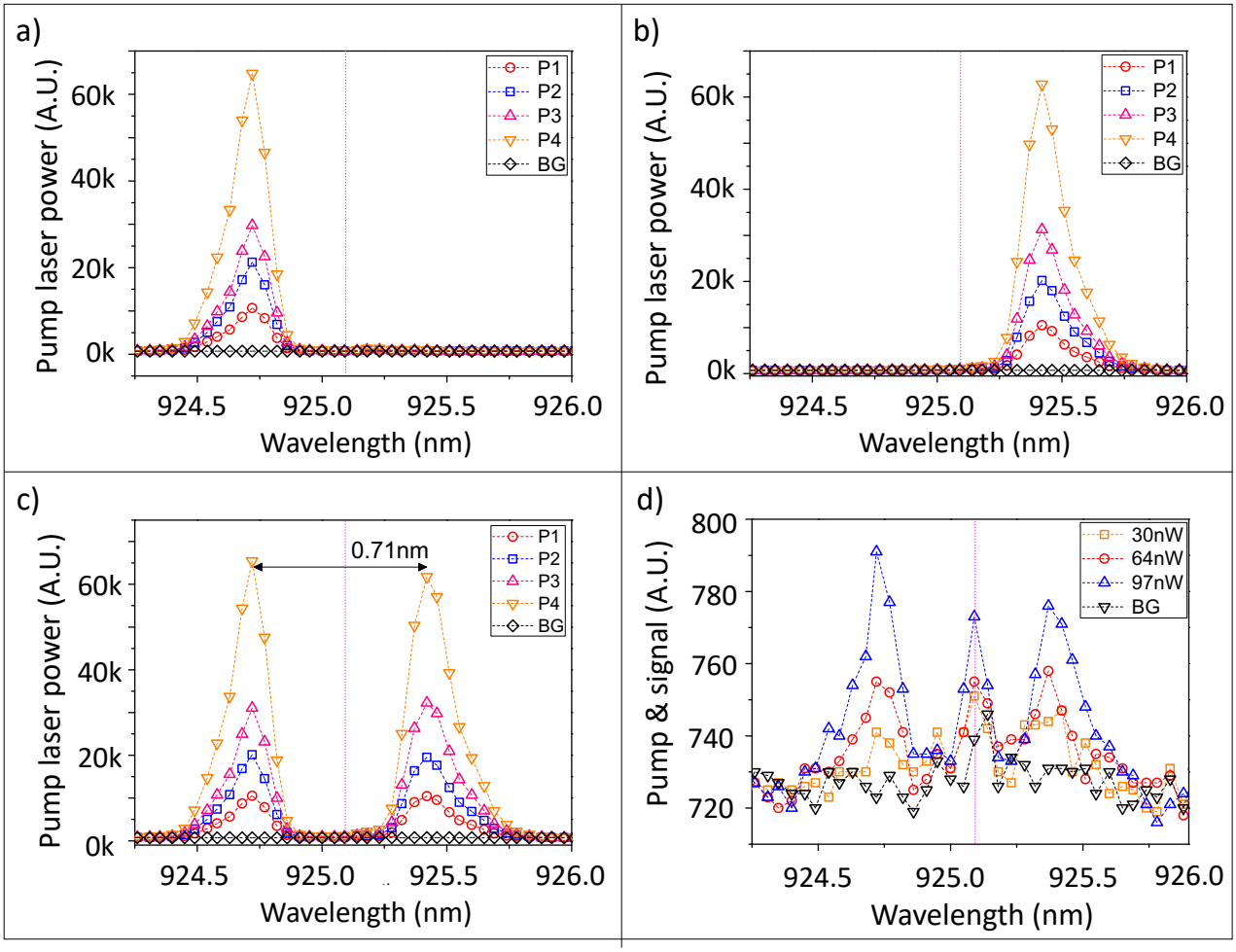


Figure 4.15: Spectral change according to the strength of the sidebands (the blue–to–red peak distance: 0.710 $\pm$ 0.005nm) pulse pump laser. The pink dotted lines indicate the central wavelength of single–photon emission. a) The spectrum of the longer wavelength side is removed by turning off specific pixels on the SLM window, leaving only the shorter wavelength side, and the pump power was changed to give 10k, 20k, 30k, 65k based on the signal strength counted by the spectrometer, and compared with the background noise (BG). b) The spectrum of the short wavelength side is removed by turning off specific pixels on the SLM window, leaving only the long wavelength side, and the pump power was changed to give 10k, 20k, 30k, and 65k based on the signal strength counted by the spectrometer. c) Pump power dependency of the pulsed pump laser spectrum. The peak-to-peak separation between the two colours of the pulsed pump laser is 0.710 $\pm$ 0.005nm, pink dotted line indicates the resonant frequency d) Two-colour laser pulse pump and QD signal change with pump power. The pink dotted line indicates the position of the single photon emission wavelength 925.090 $\pm$ 0.005nm.

the collection path of single photons so that the filter can filter out the two-colour pulsed pump laser from the single–photon signal. Once the bandpass filter is secured, the machine learning optimisation process can be performed to the $g^2(0)$ and HOM–visibility measurements. The advantage of this method is the cross-polarisation excitation— the method we use in the resonant excitation which is. the polarisation directions of the pulse pump laser and the polarisation of the generated single photons are perpendicular to each other by using PBS —is not required anymore, which means the collection efficiency of single–photons can be improved by avoiding the 50% loss— the loss occurs in the PBS

—of single photons.

4.5.3 Conclusion

We have shown the performance of our programmable spectral pulse shaper employing the SLM. We demonstrate resonant and phonon-assisted excitation of QDs using a modulated narrowband pulsed pump laser. Additionally, two-color excitation of QDs is performed using modulated sidebands. Here, "sideband" means that the wavelengths of two different colour pulse-pump lasers are aligned and centred around the QD's resonance wavelength. We remark that the realisation of all the different optical excitation methods of the QD to generate single photons is demonstrated simply by employing different programmed patterns on the window of the SLM, to modify the spectral configuration of the pulsed pump laser. This multi-functional feature of our spectral pulse shaper has a huge potential to be used in any other field that uses the pulsed optical pumping method.

Note that all different optical excitation methods to pump the QD have their pros and cons, it is hard to say which one is better in general.

In the case of resonance excitation using a narrow–band pulsed pump laser, the highest level of multiphoton suppression and single photon indistinguishability is obtained without using a spectral filter— etalon-filter —to remove the pump laser in the collection path. Employing the spectral filter in our system would boost the level of multiphoton suppression and single photon indistinguishability. Using SNSPD instead of APDs, better multi–photon suppression is measured although there was background noise due to the greater collection efficiency of the detector.

In the case of phonon-assisted excitation, if an additional precise spectral filter is applied, there is no need to use the PBS used to apply the cross-polarisation—the set-up in which the pump laser and the collected single photons have polarisation directions perpendicular to each other— Therefore, it is possible to increase the single photon collection efficiency, and it is expected that sufficiently bright single–photons can be obtained.

In the case of the coherently driven two-colour excitation, we show a result that is not a perfect coherent combination of two colours. However, it appears that the two-colour excitation is sufficiently implemented as evidence that a single–phonon signal responds to an externally applied voltage bias. If we obtain a sufficiently well-separated two-colour pulsed pump laser without overlapping with the micropillar cavity mode of our source and apply an appropriate bandpass filter that can pass only a single–photon emission line in the single–photon collection path, the two-colour excitation method can be implemented in an experimental setup with a much more compact size compared to the size of the setup performed by He *et al.* [88]. Also, this excitation method implements a PBS-free setup in the excitation path, much better single-photon collection efficiency compared to the resonant excitation method is achievable. Ultimately, it is expected that machine–learning optimisation to the window of SLM would allow us to achieve more accurate phase matching between two colours.

Chapter 5

Automatic Optimisation of Quantum Dot Single Photon Sources

This chapter explains how machine learning (ML) is used to enhance the quality of single photons. Firstly, we utilise an ML algorithm to automatically optimise the single-photon purity and indistinguishability by manipulating the spatial light modulator (SLM), a key component of the spectral pulse shaper setup. This method enables us to find the appropriate pulsed pump laser to excite a particular QD single photon source. Secondly, we apply an ML algorithm to the deformable mirror (DM), which is one of the key components of the single photon collection path, to automatically optimise the single-photon brightness. This helps us to find the best mirror configuration to achieve the highest possible coupling efficiency of single photons into the single-mode fibre.

5.1 Introduction

Classification of machine learning

In general, there are four main categories of machine learning: supervised learning, unsupervised learning, semi-supervised learning, and reinforcement learning.

Supervised learning means that humans provide input and output values to learn. In other words, a machine learns data containing a problem and the correct answer and predicts the correct answer when given such a problem later. For example, if we give data with a picture of a koala (input value) and an output value (whether it is a koala or not), the machine will learn based on the picture of a koala and the information that the picture is a koala. Later, when the machine receives a photo, it can tell us whether the photo is a koala or not.

Unlike supervised learning, unsupervised learning does not involve humans providing problems and correct answers. We need to provide data to the machine, which will find specific patterns or shapes. For example, if we give a machine a lot of photos of koalas and kangaroos, the machine will categorise the photos and group photos with similar characteristics. Remind that In supervised

learning, a machine can find out which photo is a koala, but in unsupervised learning, a machine cannot tell whether a photo is a koala or not, and only groups photos with similar characteristics.

Semi-supervised learning uses a mixture of supervised and unsupervised learning.

Reinforcement Learning is a process in which a machine learns to achieve the maximum reward by performing the optimal behaviour in a given environment. The process involves four steps. First, the machine explores the current environment and situation. Second, it selects and executes the optimal policy based on its judgment. Third, the machine applies rewards or penalties based on the results of the execution action. Fourth, the policy is modified if necessary. The process is repeated from the beginning to create the optimal policy. For instance, a toy drone can learn to fly circularly on a closed tube-shaped track by finding the right path on its own. The policy states that if the drone moves forward according to the policy set by the drone and hits a wall, the propeller should be bent slightly to the left. Then, the process is repeated from the beginning, and the policy is revised to say that if the drone hits the wall again, the propeller should turn a little more to the left. By repeating this process, the drone can learn to complete the track without hitting anything.

Algorithms used in machine learning

In supervised learning, there are three representative algorithms. 1. Binary classification: classifies into two results depending on the input value. It is mainly used to classify true/false. For example, when a photo is entered, it checks whether it is a koala or not. 2. Multi-class classification: classification of inputs into three or more outcomes, more than binary classification. For example, input number images can be classified as 1 to 9. 3. Regression: Being able to predict by looking at the relationship between two or more variables.

In unsupervised learning, there are four representative algorithms used. 1. Clustering: a method of classifying input data. Data that is close in distance is classified into each cluster. 2. Abnormal detection: finding data that shows patterns that are significantly different from expected among data. 3. Association rule mining: used to discover meaningful rules in specific data. For example, to find rules for how often a person who buys milk also uses eggs or bread. 4. Dimensionality reduction: a method of reducing the amount of data according to a specific purpose. This is utilised because as the amount of data is reduced, complexity is reduced.

Minimising the time to find the local optimum by implementing an algorithm is a big challenge. ML cannot only minimise the time which is consumed in the process of optimisation of certain parameters but also overcome the limitations of human ability in a particular task. It has had a huge impact on most of academia and industry in recent years. Examples showing the use of ML are the following, the optimisation of two-photon absorption [91], optimisation of the two-photon-induced photo–luminescence counts [92], and optimisation of an atomic magneto-optical trap (MOT) compression stage [93].

Note that the optimisation algorithm code; M-LOOP [94] of operating the ML for this work is open-source, based on the Broyden–Fletcher–Goldfarb–Shanno (BFGS) algorithm [95]— a technique for solving unconstrained nonlinear optimisation problems iteratively to determine the descent

direction by preconditioning the gradient with curvature information of the relevant cost function —, applied to the optimisation of an atomic magneto-optical trap (MOT) compression stage at Australian National University by Tranter *et al.* [93]. We optimise our spectral pulsed pump to excite QD resonantly by using Tranter *et al.*'s [93] algorithm, allowing us to find the best spectral pulsed pump laser to reach a better performance than the human optimisations process. Before reporting our results in the next sub-section, we would like to introduce the concept of the underlying ML algorithms associated with our approach.

5.1.1 Gaussian Process

Gaussian Processes (GPs) are nonparametric models used for supervised learning, which can be employed to solve regression and probabilistic classification problems. The main advantages of GPs are that they provide a flexible and powerful way to interpolate the observations while allowing for uncertainty quantification. Hence it is a flexible ML model that encompasses other models. For instance, Kernel machines— a machine uses the kernel method which is a mathematical technique used for analysing data in ML. This method utilises a kernel function that maps data from one space to another —can learn in a principled and practical way by using Gaussian processes, which provide a probabilistic approach. The optimisation algorithm— stochastic neural network —we used in our work is based on this Gaussian process, detailed explanations and definitions of the Gaussian process are covered in great detail in the following literature [96, 97].

5.1.2 Artificial Neural Network

An artificial neural network (ANN) is a type of ML algorithm inspired by the neural networks found in animal brains. [98]. ANN closely mimic the human brain, which consists of tens of millions of simple processing nodes that are tightly interconnected [99].

Figure 5.1 shows a conceptual diagram of an artificial neural network. Each node can be connected to multiple nodes in the lower tier that receive data and nodes in the upper tier that send data [100]. In most artificial neural networks used today, data flows through nodes in only one direction [101]. A node assigns a number—known as a "weight"— to each incoming connection for data. When the network is up and running, the nodes will receive different data for each connection, and multiply by the given weight values. Next, they add all the calculated values to get a single number. If the obtained number is below the threshold, the node does not pass data to the next layer. If the obtained number exceeds the threshold, the node forwards the data to the next connected nodes. All of its weights and thresholds are initially set to random values while the neural network is trained. The input layer receives the training data which then passes through subsequent layers until reaching the output layer. Throughout the training process, the weights and thresholds are constantly fine-tuned until the model can consistently produce similar results for training data with the same labels.

Like other ML methods, ANNs—which learn from data—are generally used to solve a wide range of problems that are difficult to solve with rule-based programming. There are many trade–offs

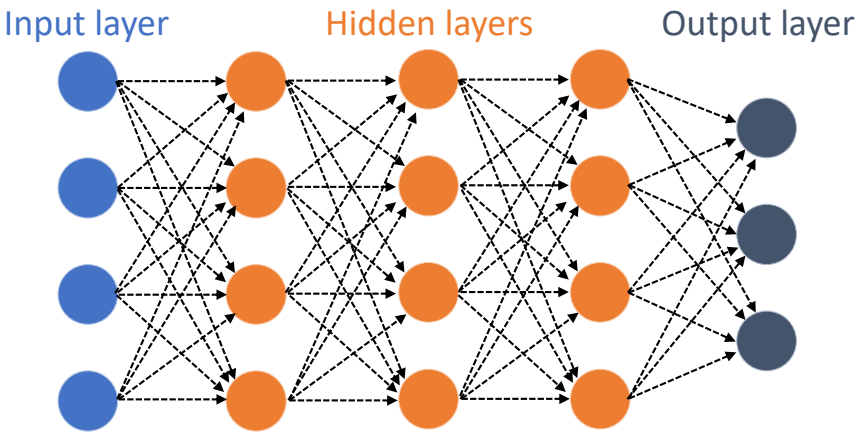


Figure 5.1: A conceptual diagram of an artificial neural network. The flow of information proceeds from left to right in the figure. For information input to the input layer represented by blue circles, each node of the input layer is connected in parallel to the nodes of the next layer represented by the following orange circles. In the same principle, each node in the next layer is connected to the previous layers, and the number of hidden layers can be arbitrarily increased. When the learning process is completed in the hidden layers, information arrives at the output layer represented by dark grey circles. When the number of these hidden layers is very large, it is commonly called deep learning.

among neural network learning algorithms, and they work well with the right hyperparameters for training on specific data sets. It takes considerable experimentation to select and adjust the learning algorithms on unknown data.

Stochastic neural network

Stochastic neural networks (SNNs) are a special kind of artificial neural networks (ANNs) that have stochastic components in their architectures, allowing the estimation of uncertainty of their predictions. In particular, a Bayesian neural network (BNN) is a type of stochastic artificial neural network that is trained using Bayesian inference [102, 103]. In the case of BNNs, the network parameters θ are considered probabilistic, which enables the networks to simulate multiple model parameter configurations according to their associated probability distribution $p(\theta)$. BNNs train multiple models that make predictions combined into probabilistic distributions. This prevents overfitting and allows estimating prediction uncertainty.

5.2 Preliminary Optimisations

5.2.1 Preliminary Optimisation: $g^2(0)$

To apply an ML algorithm for optimising the spectral pulse shape to excite the QD resonantly, we employ the spectral pulse shaper which is introduced in Figure 4.5 a) in Chapter 4. This spectral pulse shaper is programmable, the pattern on the widow of the SLM can be changed randomly, resulting in

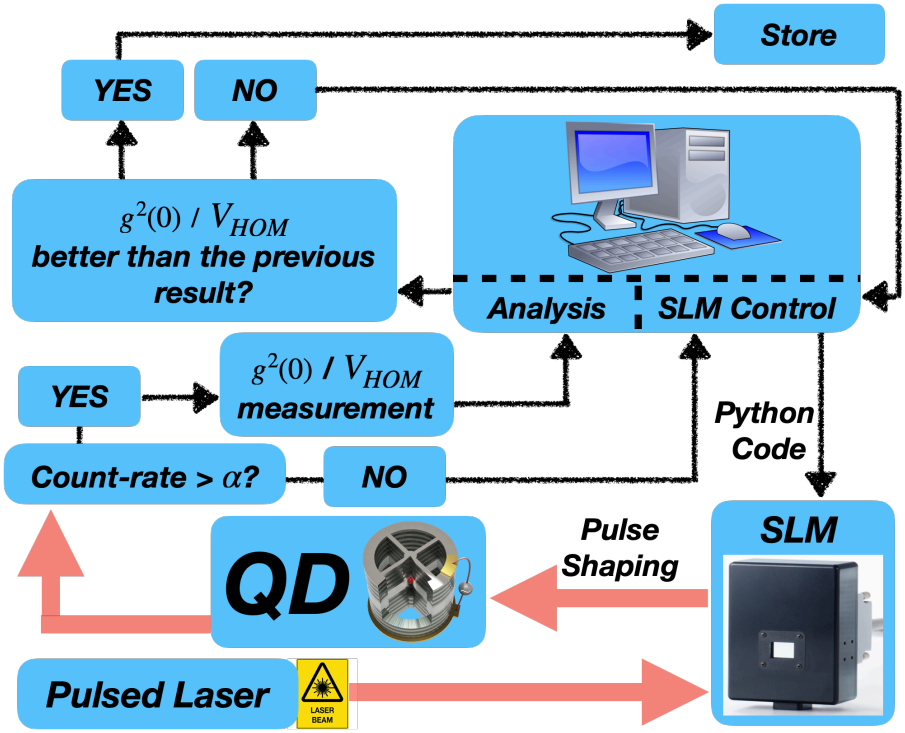


Figure 5.2: Logical flow chart of the machine learning process for pulse pump laser optimisation. Red arrows indicate optical signals and black arrows indicate electrical signals. The spectral profile of the pulsed pump laser is modulated by using a programmed initial pattern on the SLM surface in the pulse shaper. This modulated pulsed laser beam is used to pump the QD and emitted single photons are collected by a single-mode optical fibre. A 50:50 fibre beam splitter is used to split the single photons. Two avalanche photodiodes (APDs) are collected to the output of the fibre beam splitter to detect single photons. A time tag module is connected to the APDs to count single photons. If the count rate of single photons does not exceed a certain value alpha, the machine does not start the $g^2(0)$— the second-order autocorrelation function at zero delay —measurement and then forms different patterns on SLM. If the count rate of single photons exceeds the value alpha, the machine starts the $g^2(0)$ measurement to verify the single-photon purity. The measured $g^2(0)$ value and the pattern array on the window of the SLM pattern are saved on the PC. Based on the stochastic neural network algorithm, different patterned arrays on the window of the SLM are predicted and encoded, resulting in the optimisation process of the spectral pulse shaping being conducted to find the optimal pulsed beam profile to use resonantly excite the QD. If a better value is obtained compared to the previously recorded best value, the better one is saved. If a better value is not obtained compared to the previously recorded value, it is not saved and the next pattern is created. A specific operation time for each run or specific accumulated single-photon counts for each run of measurement is seated. This optimisation process can be automated by setting a particular iteration. This algorithm is also used for optimising HOM–visibility measurement.

the random modulation of the spectral shape of the pump pulses. Implementation of the dynamical pulse shaping is considered by employing a feedback–loop procedure to obtain optimal multi–photon suppression in my QD sources.

Figure 5.2 illustrates the logical flow chart of the machine learning process for pulse pump laser optimisation. Red arrows indicate optical signals and black arrows indicate electrical signals. The optimisation process is as following. A 3ps pulsed laser (Tsunami, Spectra–Physics), centred at

925.090 $\pm$ 0.005nm is prepared. This pulsed laser is coupled to the single-mode fibre to be used as the input to the spectral pulse shaper. The spectral profile of the pulsed pump laser is modulated by using a programmed initial pattern on the SLM (LCOS-SLM x10468-03, Hamamatsu) window in the pulse shaper. This modulated pulsed laser beam is used to pump the QD and emitted single photons are collected by a single-mode optical fibre. A 50:50 fibre beam splitter is used to split the single photons. Two avalanche photodiodes (APDs) are collected to the output of the fibre beam splitter to detect single photons. A time tag module is connected to the APDs to count single photons. If the count rate of single photons does not exceed a certain value alpha, the machine does not start the $g^2(0)$— the second-order autocorrelation function at zero delay —measurement and then forms different patterns on SLM. If the count rate of single photons exceeds the value alpha, the machine starts the $g^2(0)$ measurement to verify the single-photon purity. The measured $g^2(0)$ value and the pattern array on the window of the SLM pattern are saved on the PC. Based on the stochastic neural network algorithm, different patterned arrays on the window of the SLM are predicted and encoded, resulting in the optimisation process of the spectral pulse shaping being conducted to find the optimal pulsed beam profile to use resonantly excite the QD. If a better value is obtained compared to the previously recorded best value, the better one is saved. If a better value is not obtained compared to the previously recorded value, it is not saved and the next pattern is created. A specific operation time for each run or specific accumulated single-photon counts for each run of measurement is seated. This optimisation process can be automated by setting a particular iteration. This algorithm is also used for optimising HOM–visibility measurement.

Note that the reason behind choosing only 16 vertical pixel arrays on the window of the SLM is that the actual beam size on the screen of the SLM is much smaller than the total area of the SLM window, 16 vertical pixel arrays are large enough to cover the actual beam size. We program a patterned window on a PC and shift the patterned window on the screen of the SLM. This can be done by setting the screen of the SLM as the second monitor of our PC. Note that, in theory, we could consider a setup in which we could spread the diffracted beam further so that it covers the entire pixel arrays on the surface window of the SLM. However, there are two issues raised in this case. First, the larger the size of the spectral pulse shaping setup, the less power efficiency at the end of the fibre-coupled pump pulses, caused by the exponentially decreasing beam intensity after each diffraction. Second, lots of unwanted interferences caused by the unwanted obstacles— micro dust or water vapour —in the beam path may increase. Hence, achieving a narrow spectral pulse pump is targeted with an appropriate level of beam expansion, even if the entire SLM window is not covered. As shown in Figure 4.5 c) of Chapter 4, we found that using three vertical pixel columns in the centre of the effective area on the SLM window can produce the smallest spectral (bandwidth FWHM = 0.13 $\pm$ 0.005nm) of the pulsed pump laser.

Note, the reason we considered the diffraction in the vertical direction by forming a sawtooth-pattern on the SLM window is that the first pattern of diffraction grating (Echelle Gratings GE2550-0363, Thorlabs) used in the 4–f pulse shaper uses a sawtooth-pattern in the horizontal direction. This is because we are well aware of the phenomenon of diffracting the pulse beam to spread the spectral

elements. Second, since diffraction in the same direction as the beam diffracted from the grating can be avoided, spatial separation from the incident beam is easily possible in the process of collecting the final diffracted beam. FWHM 0.140 $\pm$ 0.005nm Obtains the spectral bandwidth of the pump laser. This bandwidth-related vector array parameter generates the pixel pattern configuration of the SLM window and is used as a seed for the training process during the entire ML process.

We start ML by providing a seed value with the sawtooth patterned mask on the SLM window that produces pulses with a narrow spectral bandwidth. We program a Python code that calculates the $g^2(0)$ value based on the measured coincidence count histogram graph. In the graph, we consider the areas of the five peaks at the different time delays (-25ns, -12.5ns, 0ns, 12.5ns, 25ns). This time delay represents the gap between the single-photon arrival time in the two detectors— avalanche photodiode (APD: Perkin-Elmer SPCM-AQR-14-FC) —after going through the BS.

If we measure the second-order correlation function: $g^2(0)$ by using a fibre–based HBT interferometer, we have histogram peaks around the zero delays. Since we use 12.5ns pulse duration pump pulses, the produced single-photons are separated by 12.5ns in sequence. Let's define the area of the single–photon coincidence count peak at –25ns, –12.5ns, 0ns, 12.5ns, 25ns as A_0, A_1, A_2, A_3, A_4. Then, the value which is used in the ML process is obtained by following a comparison of peak areas, $A_2/((A_0+A_4)/2)$. This ratio is also used for measuring two-photon interference.

$g^2(0)$ is measured by analysing the coincidence counting in the time tagging module (TTM: TTM8000, Austrian Institute of Technology) which is connected with the two APDs. We set $g^2(0)$ not to be measured unless the total single–photon count rate exceeds 35kHz, and another pattern is set to form on the SLM. If the single–photon count rate is 35kHz or more, $g^2(0)$ is measured until the cumulative single–photon count of each measurement is 5 million. We set the 50 times initial run— training run —at the beginning of the ML. $g^2(0)$ is measured in this initial 50 times by forming random patterns on the SLM window to explore the parameter space so the machine can learn. In the subsequent ML process, pattern generation predicts the optimisation value by adjusting various parameters based on the results learned in the 50 times initial run (training run). Based on the predicted value, similar parameter combinations around it are explored, and the $g^2(0)$ value is measured under conditions above a certain count rate and compared with previously measured values. In our experiment, we set 300 iterations for the optimising run. Once the total 350 times of $g^2(0)$ measurements—50 times of initial run and 300 times of the learning process— are completed, the optimisation process is finished. Note, that we set the bar at 5 million accumulated counts to start a measurement. There are two main reasons, 1. More statistical consideration of each measurement: by increasing the number of measured samples, the variance of the sample–mean is minimised. 2. Efficiency of a whole ML process and pump laser drifting: the measurement of each $g^2(0)$ needs to have a finite time period. This also ensures a time range that is not affected by the natural drifting of the pump laser in a well-controlled laboratory environment (temperature, humidity, vibration, etc.). Thus, a practical limitation is placed on one measurement.

Figure 5.3 shows the preliminary optimisation result to find the minimum $g^2(0)$ by implementing the algorithm drawn in Figure 5.2. To show the progress of ML, we define some parameters and graph

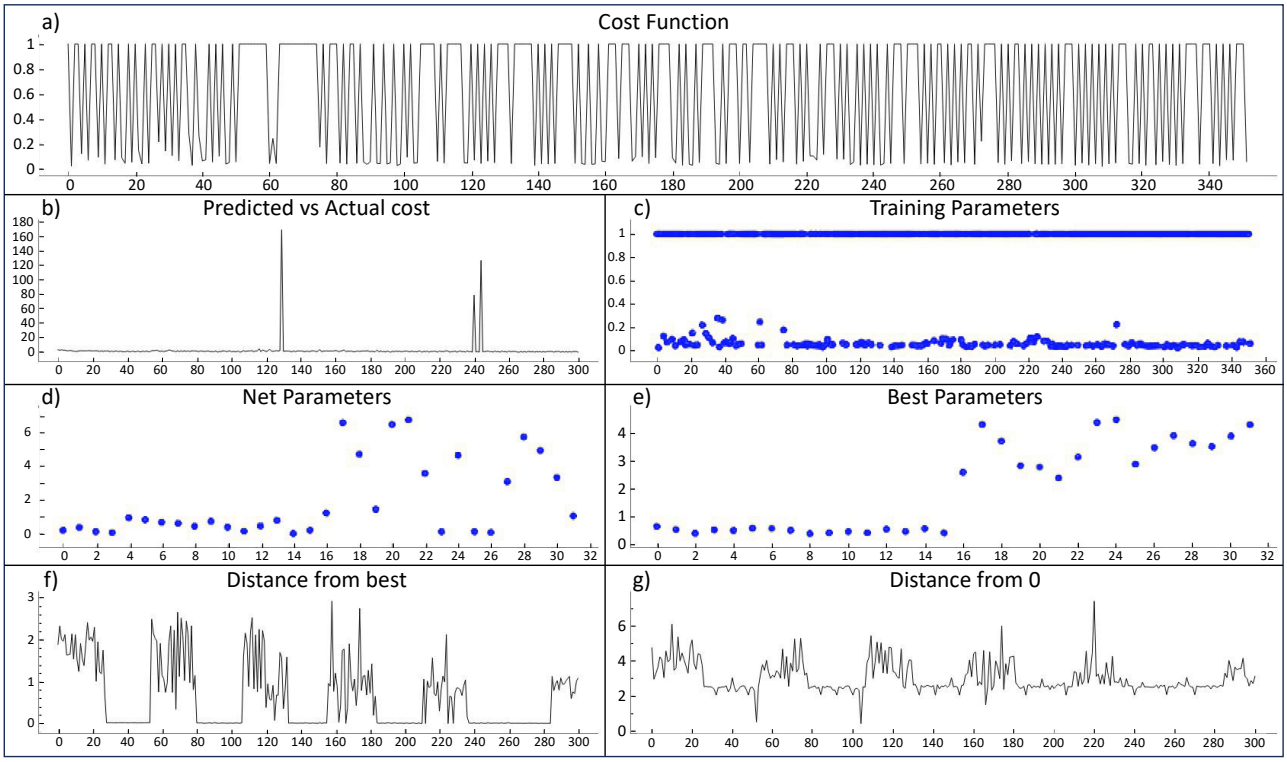


Figure 5.3: Preliminary test run of the machine–learning (ML) for $g^2(0)$ measurement. a) Cost Function. The history of the recorded costs for an entire run. the value of the cost representing the $g^2(0)$, can be used to track the progress of the learner. b) Predicted vs Actual Cost. The value is (measured cost - predicted cost), how "surprised" the learner is. As the learner determines the next best point to try, it will generate a prediction of the cost as well from its internal model. This shows how accurately the model is predicting the space. c) Training Parameters. This shows the current set of training parameters. d) Net Parameters. The current set of parameters is being passed to my experiment for trial. e) Best Parameters. The current best-known parameters observed so far. f) Distance from Best. This takes a measure of the distance in parameter space from the current set of parameters being tried to the current known best, i.e. is the net moving away or staying relatively close? g) Distance from 0. This takes a measure of distance in parameter space regarding the centre of the bounds (so-called 0 for symmetric bounds). this is used to see the absolute position of the learner.

them. 'Cost Function', which is a function used to derive a hypothetical function with the smallest error from the original value. 'Predicted vs Actual cost', is a value that represents the difference between the expected cost and the actual cost, the larger the value, the more startled the learner. We can use it to monitor how accurately your model predicts space. Next, 'Training Parameters', which means the current training parameter set, and when graphed, each variance of the cost function is represented by blue dots. 'Net Parameters', is the current set of parameters passed to my experiment for testing. 'Best Parameter', which means the best-known parameter observed to date. 'Distance from best', is the distance in the parameter space from the current set of parameters being tried to the currently best-known one. 'Distance from zero', refers to the distance in the parametric space concerning the centre of the boundary, in the case of a symmetric boundary it represents the so-called zero value, which can be used to see the absolute position of the learner.

Note that we define four learners— Explorer, Learner-1, Learner-2, and Learner-3—to carry out

the optimisation process. These four learners are the multiple models in the BNN, that can make predictions combined into probabilistic distributions (See page 50). We define a vector array in our Python code. This vector array is formed by 32 digital numbers. The first 16 numbers are assigned to adjust the amplitude of a specific pixel column in the SLM window, and the remaining 16 numbers are assigned to adjust the phase of the pixel columns assigned to adjust the amplitude in the SLM window. When performing machine learning optimization, we set the 7th, 8th, and 9th parameters of this vector array to 1 to provide the maximum amplitude. Setting the 25th, 26th, and 27th parameters to 5 provides the maximum phase for the assigned pixel row. The combination of these conditions allows the creation of narrowband pulsed pump lasers. This vector array is provided to the machine as a "Seed" parameter, and training and optimization runs are performed based on this seed.

Note that the position of the third '1' is aligned with the centre of the laser beam. These parameters create a sawtooth pattern on the specific pixel columns on the window, resulting in a narrowband pulse pump to excite the QD. These 32 numbers are assigned to the 16-pixel columns in the middle area of the SLM window. The first 16 numbers of the vector array represent the independent amplitude control of each pixel column, and the 16 following numbers of the vector array represent the independent phase control of each pixel column. We set the range of the amplitude value between 0 and 1, and the range of the phase value between 0 and 7. Note that, to test the performance of the ML code, the amplitude and phase values assigned to each pixel column were provided in different locations instead of matching them. Basically, in the process of optimising with a large number of runs, the machine will apply and combine numerous amplitude and phase values to each pixel column, and eventually find the most suitable combination of amplitude and phase values. Therefore, the initially given amplitude and phase values to a specific pixel column may slightly increase the time it takes to find the final optimisation value, but it is not a big problem.

We set the initial 50 times run as the training run to explore the parameter space. The optimising runs are set to 300 times after the initial runs. The machine undergoes the trials to find the optimal $g^2(0)$ value, as a result, two $g^2(0)$ values— the estimated $g^2(0) = 0.023$ is discovered by the Explorer, and the estimated g2(0) = 0.021 is discovered by Learner-3 —are found with corresponding the amplitude and the phase parameters.

The cost function which is shown in Figure 5.3 a) and c), that is the value can be regarded as the value of $g^2(0)$. The optimisation process of this cost function in Figure 5.3 a) shows that the ML optimising process is not operating properly. This poor performance can be analysed for a few reasons. First, if the total single–photon count rate is less than 35kHz, the cost function is set to output 1 no matter what value of $g^2(0)$ is measured, resulting in inaccurate prediction on the cost function. Second, the stability of the Tsunami pulsed–pump laser can drift. The pumping wavelength we use for common excitation is in the 925.09nm region, which is in the wavelength region where stabilisation is the most difficult to obtain in the pulsing of a Tsunami laser. This is because of the characteristics of the Ti-Sapphire laser. The strength of the water-absorption line of Ti-Sapphire crystal is very weak in the wavelength range between 840nm and 1000nm, the pulse stability can be secured only by continuously supplying nitrogen gas to the laser cavity for a long time. For a detailed description

of the stabilisation technique for the Ti-Sapphire laser, refer to Chapter 7 in the user manual of the Spectra-Physics Tsunami laser.

From now on, among the visualised machine learning process graphs, only the cost function graph is presented to view the optimisation trend.

5.2.2 Preliminary Optimisation: HOM–visibility

The HOM-visibility optimisation is performed by using the same code which is used to calculate the $g^2(0)$. Strictly speaking, to calculate an accurate HOM visibility value we need to compare the coincidence count ratio between the single–photon coincidence count peak at 0ns delay and the average of all other single–photon coincidence count peaks except for the $\pm$12.5ns delay. However, statistically sufficient single–photon cumulative counts are considered, and all other single–photon coincidence count peaks except for the single–photon coincidence count peak at $\pm$12.5ns delay are mostly similar in size. In practical terms, the HOM visibility can be measured by using the same peak ratio calculation code which is used to calculate $g^2(0)$.

To measure HOM-visibility, the reflectance ($\mathscr{R}$) and the transmittance ($\mathscr{T}$) of a fibre beam splitter (FBS) used for two-photon interference were measured. When a beam is incident on an input port called A and power is measured at each of the two output ports, $\mathscr{R}$: $\mathscr{T}$ = 0.5012:0.4987. When a beam is incident on another input port B and power is measured at each of the two output ports, $\mathscr{R}$: $\mathscr{T}$ = 0.4951 : 0.5048. We average the value of both cases to get $\mathscr{R}$: $\mathscr{T}$ = 0.4981 : 0.5018. Note that the ideal FBS used in the two-photon interference experiment has $\mathscr{R}$: $\mathscr{T}$ = 0.5 : 0.5. The visibility is calculated by Equation 5.1, which is considered in Ref. [34].

$$V = \frac{\mathscr{R}^2 + \mathscr{T}^2 - A_2/((A_0 + A_4)/2)}{2\mathscr{R}\mathscr{T}} \tag{5.1}$$

We test the automated optimisation by implementing the same algorithm— Figure 5.2 —to find the optimal HOM–visibility. Free–space Hong-Ou-Mandel interferometer and a 50:50 FBS are used to measure the HOM visibility.

Figure 5.4 a) shows ML optimisation of HOM-visibility by implementing the algorithm (Figure 5.2). We employed the same ML optimisation algorithm that is used for $g^2(0)$ ML optimisation algorithm. As a result, eight stepwise optimisation values are found, and eight estimated HOM–visibility values— 0.838, 0.886, 0.887, 0.901, 0.907, 0.911, 0.918, 0.920 —are obtained. This estimate can have a mean error of $> \pm 0.026$ due to time-varying variations of the coincidence count peaks. The parameters obtained from the 8 steps found in the ML optimisation of HOM-visibility optimisation.

Figure 5.4 b) shows the evolution of HOM-visibility through ML optimisation. Using the machine-found parameter combinations of vector arrays, the 8 different shapes of the pump pulse are reproduced. Then they are used to excite the QD resonantly to measure the HOM-visibility of each optimisation step. 350k accumulated single-photon counts for each measurement are set to measure HOM visibility again. These confirmation measurements have relatively smaller accumulated single-photon

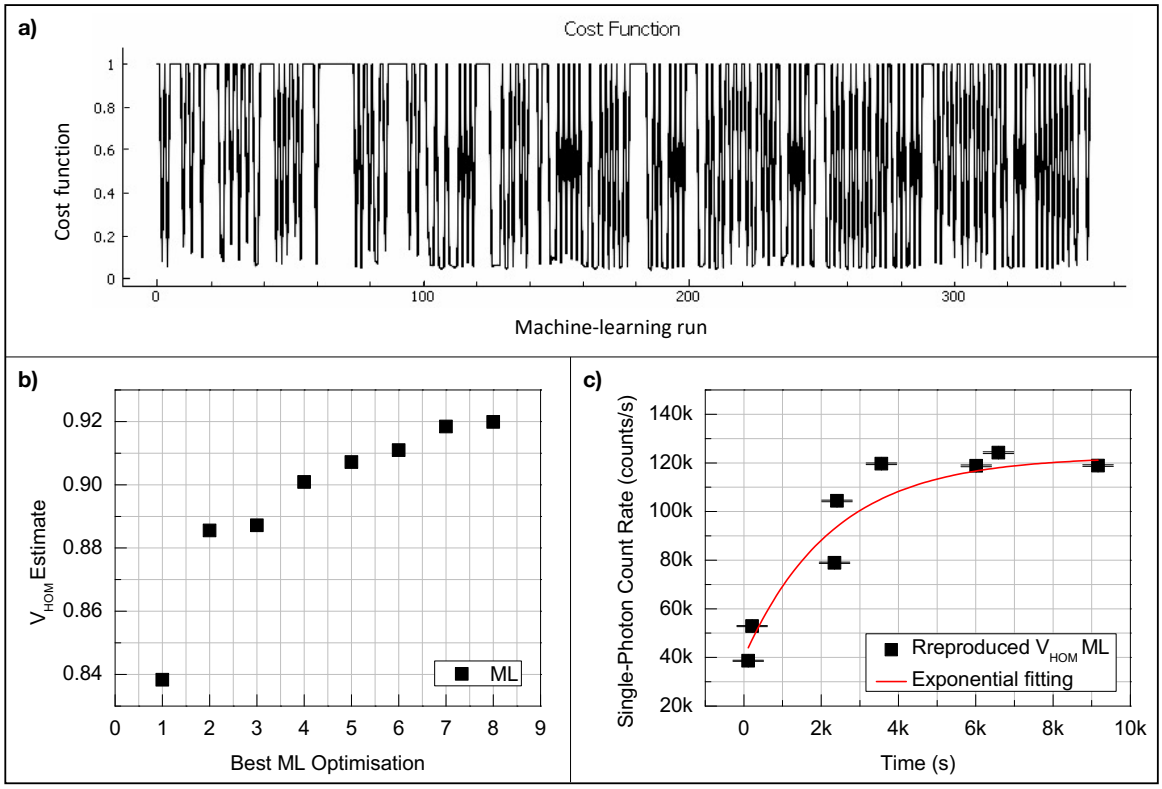


Figure 5.4: Preliminary test run of ML optimisation of the HOM–visibility measurement. a) Cost Function. The value of the cost representing the 1-(HOM–visibility). b) Evolution of HOM–visibility in the process: 5 million accumulated counts in each data dot of the ML process (black squares). HOM-visibility can be easily calculated by 1–(cost function). Estimated HOM-visibility = 0.838 is used as the seed value, and estimated HOM-visibility = 0.920 is found as the optimum at the end. The difference between measured and ideal visibility, $1 - V_{HOM}Est.$, drops by a factor of two, from $>$0.16 to 0.08. This estimate can have a mean error of $> \pm 0.026$ due to time-varying variations of the coincidence count peaks. c) Evolution of the single-photon count–rate. With 7 SLM configuration parameters that gradually achieved the HOM-visibility optimisation found through ML, the HOM-visibility measurement was reproduced using TTM8000 software. In this process, the single-photon count rate for each SLM configuration parameter was simultaneously measured. Note this increases by more than 3 times.

counts per each HOM-visibility measurement than the setting used in the ML process. The process shows the trend of optimising HOM-visibility

Figure 5.4 c) shows the evolution of the single–photon count rate in the ML optimisation process of HOM-visibility. These are measured simultaneously when HOM–visibility values are measured again. The single-photon counting rates are measured in 5s, 12 times measurements are performed and averaged. The count rate increases exponentially, reaching a plateau, as expected when the QD emission reaches saturation. The variation in the count rate can be thought of as the result of either the unstable pump power of the pulsed laser or the nature of resonant excitation.

Remark that Figure 5.4 b)-c) shows that our ML algorithm exponentially improves the optimization of HOM-visibility and single-photon count rate, and despite the instability of the pulse pump laser, its performance is highly resistant to changes in the external environment.

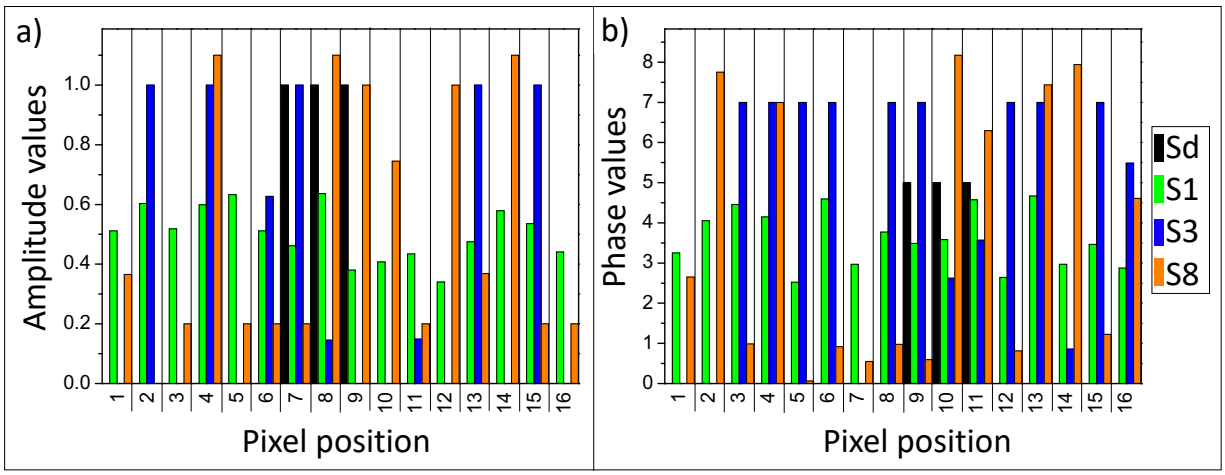


Figure 5.5: Comparison of amplitude and phase changes of SLM pixels through the machine–learning (ML) process. The array of parameters in the SLM that are used to generate the first (green), third (blue), and eighth (orange) optimisation pulses found in the ML process, respectively. The manual setting of parameters is denoted as Seed (black). Of the 16 vertical pixels on the SLM in the useful middle area, the amplitude values are set to 1 (in pixels 7, 8, 9) and the phase values are set to 5 (in pixels 9, 10, 11). This combination allows us to form the narrowest spectral bandwidth to achieve the best $g^2(0)$ and HOM–visibility in the manual pulse shaping.

Figure 5.5 shows three representative parameters (amplitude and phase combinations) found in the HOM visibility optimisation step for 16 pixel-columns in the SLM window. The size of the pump laser beam hitting the SLM window is smaller than 16-pixel columns and is accompanied by careful alignment so that pixel number 8 matches the centre of the pump laser beam. The minimum and maximum amplitude values are 0 and 1, and the computer can randomly select values in the range between them. The maximum and minimum phase values are 0 and 7, and the computer can randomly select values in the range between them. To test how quickly the machine can optimise without having to give it exact values, we intentionally provided the machine with slightly deviated amplitude and phase values. That is, in the process of providing the initial seed parameters, pixel numbers 7, 8, and 9 are input with an amplitude value of 1, and the remaining pixel numbers are input with an amplitude value of 0. At the same time, set pixel numbers 9, 10, and 11 to have a phase value of 5 and input them, and set the remaining pixel numbers to have a phase value of 0 and input them. These settings provide a seed value to guide the machine's optimisation process. Nevertheless, our algorithm shows results that perform the optimisation process without difficulty. In addition, looking at the evolution of the amplitude and phase values in Figure 5 a) and b), it is difficult to find a clear pattern, and the changing pattern of the machine optimisation process shows a direction that is difficult for humans to predict. Additionally, one unexpected result is that a phase value greater than 7 appears in the 8-stage optimisation result data, which shows a result that is outside the range of the maximum value we set. It is thought that the computer recognizes the phase from 0 degrees to 2 pi as one cycle, and the computer recognizes the phase from 0 to 7 as one cycle. Values greater than 7 are predicted to represent the phase after one cycle is completed, but additional experiments and research are needed.

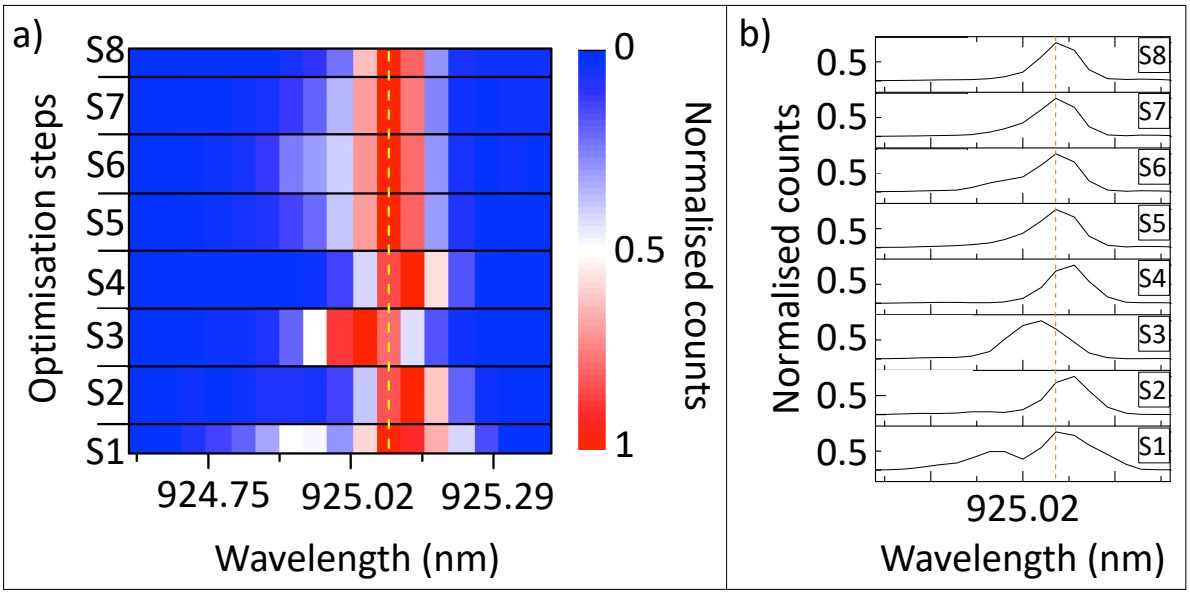


Figure 5.6: Evolution of spectral shapes showing the results of HOM-visibility evolution by ML optimisation. The evolution process of the normalised spectral signals of the shaped pulses from the first discovered optimised spectrum (S1) to the last found optimised spectrum (S8). The eight optimised spectra (S1-S8) were found by the machine. a) The spectrum of shaping pulses tends to become increasingly narrow with the ML process. The yellow dashed line indicates the central wavelength position of the QD resonance fluorescence signal. b) The central wavelength of the QD resonance fluorescence signal is indicated by the orange dashed line.

Figure 5.6 a) and b) shows the evolution of eight pulsed laser spectra obtained through the ML optimisation process for HOM visibility. In the first optimisation step (S1), a spectrum with two peaks was optimised, and as optimisation is achieved, the bandwidth of the central wavelength of the pump laser tends to decrease. Additionally, the central wavelength does not remain constant but tends to fluctuate. Presumably, the instability of pulse-pump lasers has a significant impact on the shift of the central wavelength. If the pump pulses do not stabilise, the reference point will continue to change during the optimisation process. This can confuse the machine if the reference point changes during optimisation based on information already obtained during the learning process. In addition, it is expected that the amplitude and phase values of the seed parameters are provided instead of being applied to the same pixel column, increasing learning time.

Once again, we see that our algorithm has a strong tolerance to changes in the experimental environment and exhibits exponentially faster optimisation performance even when incorrect initial values are entered during the optimisation process.

5.3 Machine-Learning Optimisation

So far, we have assumed that the shape of the pulse spectrum needed to resonantly excite our QD single-photon source is narrowband, and have adjusted the pixels in the SLM window to generate

narrowband pulses. Additionally, optimisation through machine learning proved that the optimised pump pulse we assumed was narrowband. Nevertheless, the beam propagation mechanism in the pulse shaping setup is unclear, and the pump power of the laser achievable in the collection after pulse shaping is insufficient.

Therefore, we set the rationale for using ML to find the spectrum of the optimised pulsed pump laser required to generate optimised single-photons through resonance excitation of the QD. In our preliminary experiments, we inferred that, in principle, a pulse pump in a narrow band region could be achieved by dispersing the spectrum as much as possible and extracting only spectral elements using only the fewest number of pixels among the pixels on the SLM, and optimised through ML. We used ML to check whether the results were consistent with our inferences. However, we cannot guarantee that the optimised pulse pump spectrum shape used when generating optimised single photons through resonance excitation of our QD is necessarily a narrowband pulse pump spectrum. In addition, even if we know the optimised pulse pump spectrum used to generate optimised single photons through resonance excitation of our QDs, it must also be considered whether that spectrum simultaneously satisfies the optimised pump power. Therefore, we abandoned the preliminary experimental setup and recreated an accurate 4-f pulse shaper capable of generating sufficient pump power, using ML with a larger effective area on the SLM window.

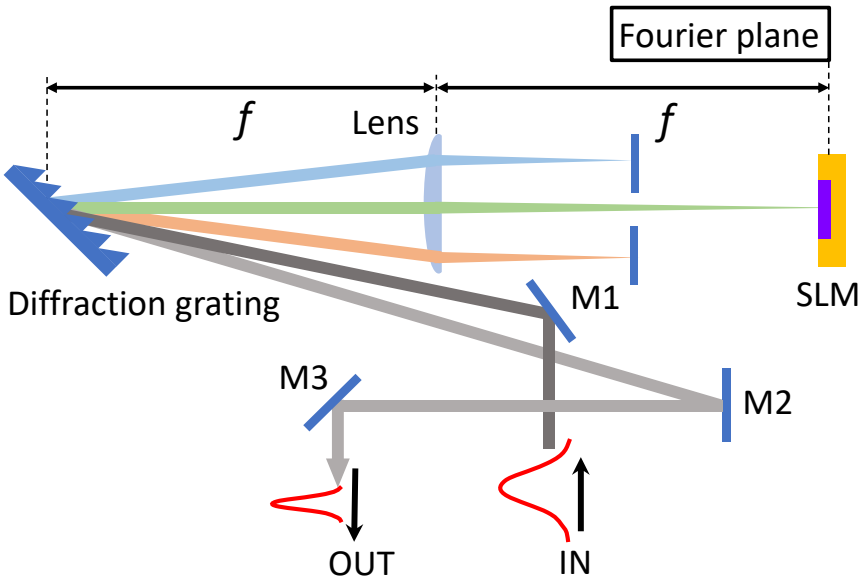


Figure 5.7: Top-view of experimental apparatus considered in the pulse shaping protocol (exactly folded 4–f pulse shaper using an SLM). A collimated 3ps tsunami pulsed laser is reflected from the first mirror (M1), and then diffracted by the diffraction grating (Echelle grating GE2550-0363, Thorlabs). One of the horizontally diffracted modes is selected, focused through the plano-convex cylindrical lens (LJ1277L2-B,f=250mm,Thorlabs) to reach the SLM (512×512 Liquid Crystal on Silicon Spatial Light Modulators, Meadowlark Optics). The phase and amplitude of the liquid crystal material in the SLM can be programmed and adjusted, and are used to make a pattern, e.g. a sawtooth shape in the vertical direction. One of the vertically diffracted modes from the SLM surface is selected, sent back to the grating, and then coupled into the single-mode fibre through the second mirror (M2) and the third mirror (M3).

Note that from this moment, we use a different SLM (512 × 512, Liquid Crystal on Silicon Spatial Light Modulator, Meadowlark Optics) to overcome the issues of the pulse-shaper setup which is shown in Figure 4.5 a). The cylindrical lens— plano-convex cylindrical lens (LJ1277L2-B, f=250mm, Thorlabs) —is used to reduce the back-reflection on the surface with the wavelength of our pump laser. In addition, the SLM was placed in the Fourier plane to maximise the recombination of diffracted modes that came from the SLM window to ensure maximum out-coupling power, providing sufficient energy to excite the QD.

Figure 5.7 shows the spectral pulse shaping setup which follows exactly the folded 4-f pulse shaper setup employing the new SLM (Meadowlark Optics). The beam size reaching the SLM window we obtained is larger than the beam size. This means that the effective area that the beam touches in the SLM window has increased, and the number of pixels that control the beam has increased among the 512×512 pixels that exist on the SLM window. It is difficult to measure the precise size of the beam hitting the SLM window using a beam profiler because the space between the cylinder-shaped lens and the SLM was narrow in the setup. However, it is possible to relatively estimate the change in beam size. In preliminary experiments, when we created a pulse shaper that did not follow the 4-f configuration, we found that among the 16-pixel pillars in the SLM window, we could obtain the narrowest band pulse by turning on 3-pixel pillars in the middle area and creating a sawtooth pattern. However, when we created a pulse shaper that followed the exact 4-f configuration, we were able to obtain the narrowest band pulse when we turned on the 5-pixel columns in the middle area out of the 10-pixel columns in the SLM window and created a sawtooth pattern. This setup is used to operate the ML optimisations for the $g^2(0)$ and HOM-visibility.

On top of this improvement, sufficient nitrogen gas is purged in the Tsunami pump laser cavity for more than 2 hours, to ensure the laser pulse was very stable. The humidity and temperature in the pump laser cavity were monitored in real-time by using a Bluetooth-connected sensor (HT1 Temperature and Humidity Smart Sensor, SensorPush) during the ML process. We found that purging nitrogen gas would maintain a humidity of $7.3 \pm 0.1\%$ during the ML process, which lasted for almost 3.5 hours. Note that the ideal humidity condition for the perfect pulsing performance of the cavity is known to be $3.0 \pm 0.1\%$, according to Chapter 7 in the user manual of the Spectra-Physics Tsunami laser. These comparably stable pump pulses undergo the spectral pulse shaping protocol— Figure 5.7 —to be prepared as a pump for the QD. Then the shaped pump pulses are used to excite the QD, and the $g^2(0)$ was measured by using TTM and APDs. The estimated $g^2(0)$ = 0.042 with the average count-rate was 140 ± 1kHz on the APDs.

Figure 5.8 a) shows the result of $g^2(0)$ ML optimisation by using the spectral pulse shaper (Figure 5.7) and implementing the algorithm (Figure 5.2). An ML optimization process is performed to find again the minimum $g^2(0)$. We used the same ML optimization algorithm used in the preliminary $g^2(0)$ ML optimisation algorithm and provided the same seed parameter vector array. As a result, eight estimated $g^2(0)$ values—0.0709, 0.0665, 0.0648, 0.0606, 0.0598, 0.0552, 0.0532, 0.0532 —are gradually found. Although the process is converging to a lower value, the result still displays some fluctuations in the optimising process.

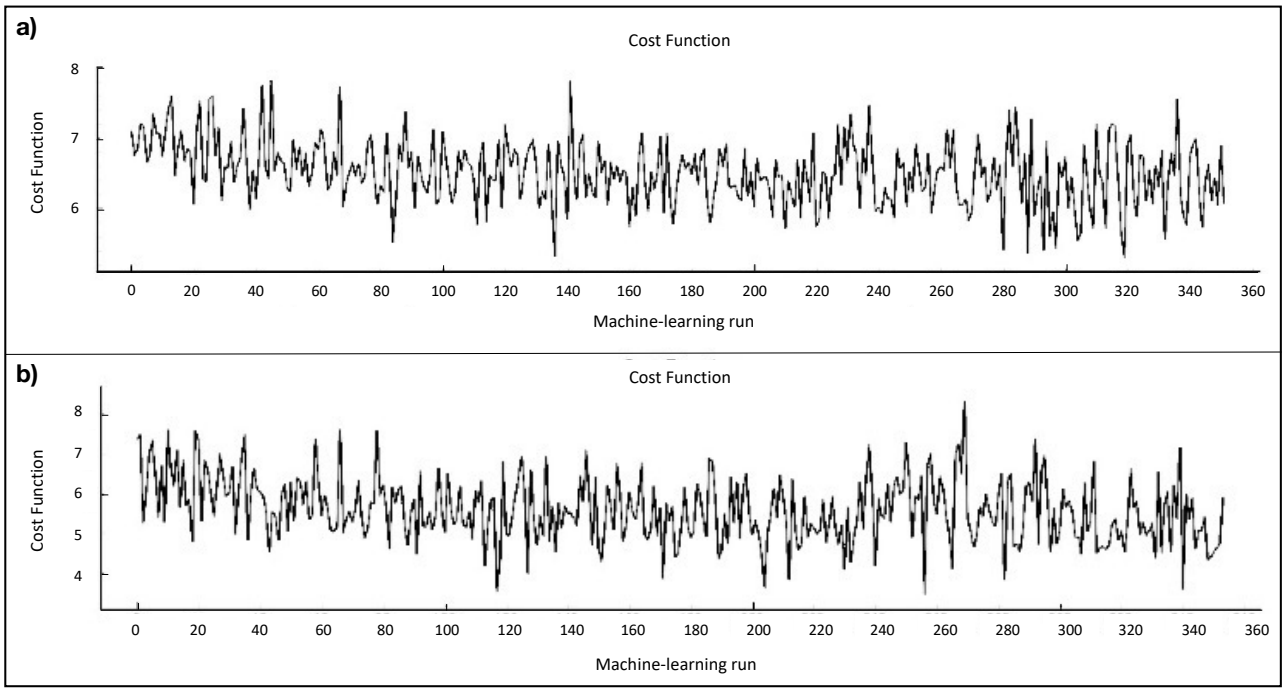


Figure 5.8: Influence of humidity inside of the cavity of the pulsed pump laser to the machine–learning (ML) optimisation of the $g^2(0)$ measurement. a) Humidity = 7.3 $\pm$ 0.1% inside of the cavity of the pulsed pump laser, machine–learning (ML) optimisation of the $g^2(0)$ measurement. a) Cost Function. This is simply the history of the recorded costs for an entire run. the value of the cost representing the $g^2(0)$ in percentage. We can use this to track the progress of the learner as it goes. Estimated $g^2(0)$= 0.0709 is used as the seed value, Estimated $g^2(0)$= 0.0531 is found as the minimum. b) Humidity = 6.6 $\pm$ 0.1% inside of the cavity of the pulsed pump laser, machine–learning (ML) optimisation of the $g^2(0)$ measurement. The value of the cost represents the $g^2(0)$ in percentage. Estimated $g^2(0)$= 0.0738 is used as the seed value, estimated $g^2(0)$= 0.0350 is found as the minimum.

Figure 5.8 b) shows that further investigation is conducted to see the effect of humidity on the fluctuation of the $g^2(0)$–optimisation. The humidity in the pump laser cavity is monitored and maintained at 6.6 $\pm$ 0.1% during the ML process. As a result, seven estimated $g^2(0)$ values—0.0739, 0.0482, 0.0456, 0.0449, 0.0420, 0.0354, 0.0350—are gradually found with corresponding amplitude and the phase parameters.

Summarising the result of two ML optimisation attempts under extremely stabilised humidity conditions (less than 7.3 $\pm$ 0.1% and less than 6.6 $\pm$ 0.1%) in the resonator inside the pump laser, both results showed a clear decreasing trend. The fluctuation of $g^2(0)$ values in the processes has remained but is much more stable than the preliminary test run. Perhaps, the reason for this fluctuation can be thought of as a natural property of the resonance excitation scheme. All estimates of $g^2(0)$ from ML have little statistical consideration for the coincidence count peak area used in the calculation of $g^2(0)$, and are likely to be over-estimated due to large fluctuations in the Tsunami pulsed pump laser.

5.4 Towards the Best Quantum Emitter

In this final section, we test some more improvements implemented in our machine-learning optimisation procedure.

First, the standard for measurement completion used for $g^2(0)$ measurement and HOM-visibility measurement in Sections 5.2 and 5.3 is slightly modified. In our prior measurements, we obtained data by setting the time-tag modules to cease data after accumulating a target number of events (1 million cumulative photon counting). In this new version, we set a time window to acquire data. For the $g^2(0)$ measurement we set a 40-second acquisition time for each run, for the HOM-visibility measurement we set it to a 200-second acquisition time for each run. The reason behind specifying measurement time is that we want to see the difference between assigning accumulated counts and the time window to stop each measurement so that we can decide which approach is more practical or efficient to run the whole process of the optimisation process.

Note that this comparison is essential due to knowing that the stability of the pulsed laser is critical in the long run. measurement, changes in the pulse shape influence the pump power and consequently the total single-photon counts.

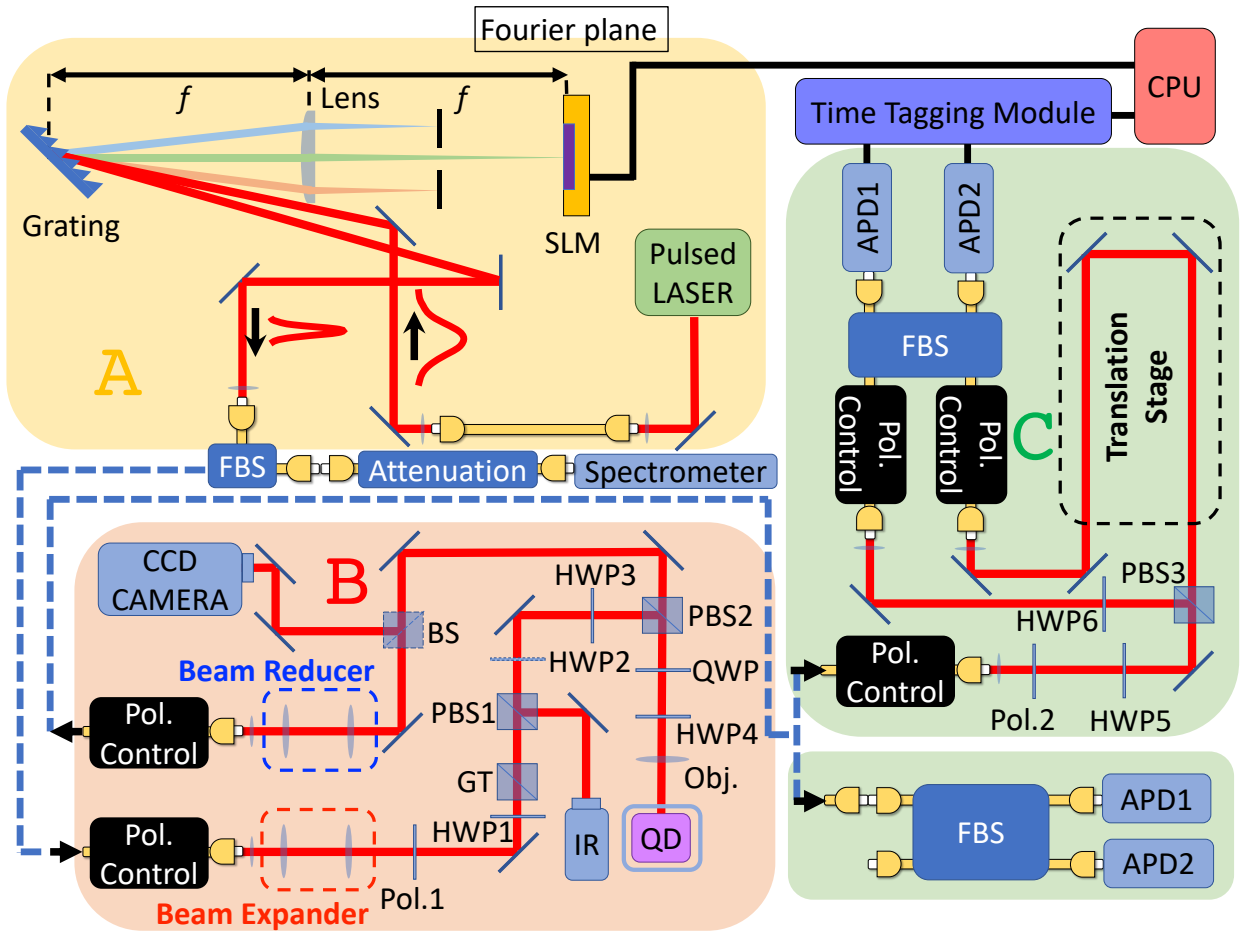
Second, we used a parallel process for the ML calculation, making it possible to employ a large number of interactions of the algorithm during each optimisation.

Lastly, instead of discarding measurements when the count rate was too small, we set a bound on the count rates, making it possible to follow any particular change in the count rate during the entire process.

Figure 5.9 shows the entire experimental setup for the final attempts (two independent ML optimisation experiments). The first optimising attempt targets optimising single-photon purity, by minimising the $g^{(2)}(0)$ value. The single-photon signal is sent to 50:50 FBS, implementing a Hanbury Brown and Twiss setup, used to measure the second-order correlation function. We apply the ML optimisation process for the measurement. The second optimising attempt targets optimising single-photon indistinguishability, by maximising the HOM-visibility. two consecutive single-photons produced by the source are sent to a Hong-Ou-Mandel interferometer, to obtain two-photon interference. We again apply the ML optimisation process for the measurement. The Python codes— $g^{(2)}(0)$ calculation, HOM–visibility calculation, SLM mask to create patterns, Obtained parameter values through the ML optimisation process —used in this section is provided in Appendix A.

5.4.1 The final attempt of Machine–Learning Optimisation: $g^2(0)$

Figure 5.10 shows the process of $g^2(0)$ ML optimisation. During the $g^2(0)$ optimisation, we set 40 seconds for each measurement for this time. the first 50 measurements are training runs of ML, generating random patterns on the SLM. The following 300 measurements are optimising runs of $g^2(0)$ measurements through the ML. Once the total 350 measurements are completed, the process is terminated, and the machine presents the steps of optimised parameters in each step with estimated $g^2(0)$ values. This entire optimisation process takes 14,000 seconds (less than 3.9 hours). Note that



HWP : Half wave plate	BS : Beam splitter	QD : Quantum dot
QWP : Quarter wave plate	APD : Avaranche photodiode	Pol. : Polariser
PBS : Polarisation beam splitter	FBS : Fibre beam splitter	GT : Glan-Tayler prism
IR : Infrared backlight	Obj. : Objective lens	SLM: Spatial light modulator

Figure 5.9: Conceptual overview of the whole experiment setup. A 925.01nm pulse pump laser is fed to a folded 4-f pulse shaper (yellow box: A). One of the modes of the pulsed laser diffracted in the horizontal direction in the reflective grating passes through the cylindrical lens and reaches the SLM. Depending on the programmed pixel, one of the modes of the pulsed laser that is vertically diffracted from the SLM reaches the reflective grating again, where it is coupled to the single-mode fibre through a slightly different path. The coupled-shaped pulse passes through a 90:10 fibre beam splitter (FBS), and 10% of the light is again attenuated through a fibre beam attenuator and monitored by a spectrometer. The remaining 90% of the light is supplied to the QD excitation & collection system (red box: B), used for resonant excitation of the QD. The generated single photons pass through the interferometer (green box: C) and are collected in avalanche photodiodes (APDs). Measure coincidence count using time tagging module to obtain HOM-visibility and $g^{(2)}(0)$ value.

at around the 240th run, the optimised cost function suddenly jumped from around 9 to around 15. And then, the value fluctuates around 15 until the end of the entire process. Note that the optimisation process was continuously monitored, and the pulse pump laser was stable and did not fluctuate for approximately 3.9 hours. This is the unexpected behaviour of the machine. Ideally, we would have expected the machine to continue exploring the parameter space similar to the minimum for a set

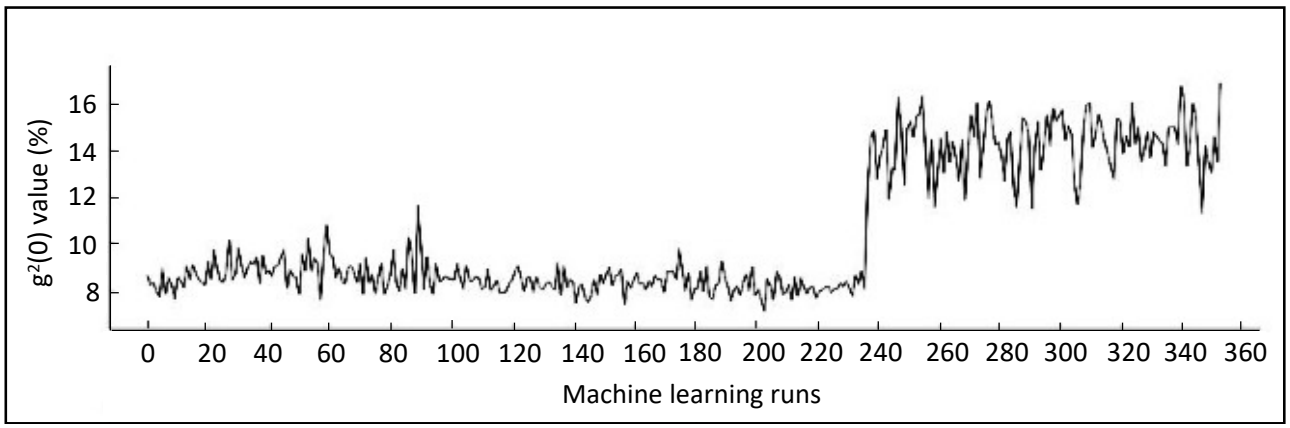


Figure 5.10: $g^2(0)$ ML optimisation process, a 40-second acquisition time for each run, Humidity = $9.0 \pm 0.3\%$ inside of the cavity of the pulsed pump laser. The value of the cost function represents the $g^2(0)$ in percentage. Estimated $g^2(0)$= 0.086 is measured by using the seed parameters, and estimated $g^2(0)$= 0.071 is found as the finally optimised.

amount of time until it found the optimal value, but this was not the case. Eventually, when optimisation no longer occurred, the machine suddenly changed its behaviour patterns. The reason for this behaviour is unknown, and more research is required. As a result, the estimate $g^2(0)$= 0.086 is obtained using the seed parameter, and the final optimisation estimate $g^2(0)$= 0.071 is found.

5.4.2 The final attempt of Machine–Learning Optimisation: HOM–visibility

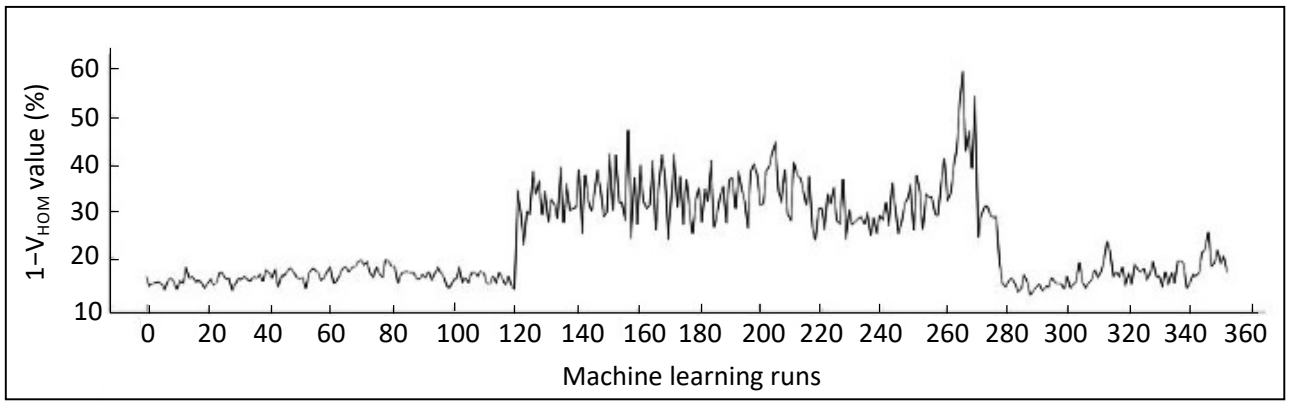


Figure 5.11: HOM–visibility ML optimisation process, a 200-second acquisition time for each run, Humidity = 7 $\pm$ 2% inside of the cavity of the pulsed pump laser. a 200-second acquisition time for each run The value of the cost function represents the 1-(HOM–visibility) in percentage. HOM-visibility can be easily calculated by (100–cost function)/100. Estimated HOM-visibility = 0.840 is used as the seed value, and estimated HOM-visibility = 0.877 is found as the minimum at the end.

Figure 5.11 shows the result of HOM-visibility optimisation through the ML. During the HOM-visibility optimisation, we set 200 seconds for each measurement for this time. The first 50 measurements are training runs of ML. The following 300 measurements are optimising runs. Once the total 350 measurements of HOM-visibility are completed, the process is terminated. This entire optimisa-

tion process takes 70,000 seconds (less than 19.5 hours) to complete. Note that at around the 120th run, the corresponding cost function suddenly jumps from around 15 to around 35, and the fluctuation continues until the 280th run. Then the cost function value comes down to 15, until the end of the entire process. This whole process is also continuously monitored. Unstable pulsing of the pump laser is observed while the process is in between the 120th and 280th runs. When the pump pulse is not stable, the optimisation process is difficult, but once the pump pulse is stable, the optimisation process is performed again based on the optimisation value found through previous learning. We once again confirm that our algorithm is robust to changes in the external environment of the system. As a result, estimated HOM-visibility = 0.840 is used as the seed value, and estimated HOM-visibility = 0.877 is found as the minimum at the end.

5.5 Improving the overall source efficiency

One of the challenging problems for us at this moment is to improve the source's overall efficiency, which is at $\sim 14\%$. To quantify the overall source efficiency, we have to consider, the (i) outcoupling efficiency from the cavity after the QD emits a photon ($\sim 60\%$); (ii) propagation losses before photon collection into a fibre ($< 1\%$); (iii) coupling efficiency into an optical fibre cable itself ($\sim 70\%$); and finally (iv) the efficiency of the detectors used to measure the photons (silicon avalanche photon diodes, efficiency$\sim$ 34%@930nm). Improving (i) is beyond our capabilities as it requires re–engineering the QD/micropillar cavity source. To improve (iv) we will employ superconducting nano-wire single-photon detectors available in the QTLab, which possess $\sim 85\%$ @930nm. Finally, to achieve better coupling efficiency into a fibre, we consider a technique relying on the use of adaptive optics, controlled by a computer search and optimisation algorithm.

5.5.1 Machine–learning Optimisation: Brightness

Improving the brightness of the source is of key importance for the applications—e.g. Boson–sampling [63, 64], Heralded nondestructive entangling gate [104], and QKD with entangled photons generated on demand by a QD [66]. No matter how high the purity and indistinguishability of the single photons, it will be of little value, if the brightness is not sufficient to give a meaningful signal.

One of the factors that affect the brightness of the source is polarisation filtering when using the resonant excitation method. This filtering used in the single–photon collection step reduces the single–photon source brightness due to the rejection of horizontal (vertical) polarised photons. In the worst case, if the QD does not have the preferred polarisation for the emission, it will result in a 50% loss. For this reason, recent proposals have considered using *biexciton*[105] or phonon–assisted [82] excitation to the QD. Both of these techniques have a key advantage: they allow excitation of the QD with a laser wavelength not centred at the QD transition, and the pump laser can be removed during the detection process with spectral filtering. However, it is difficult to implement such a technique as it not only requires control of the centre wavelength of the excitation laser but also changes the overall

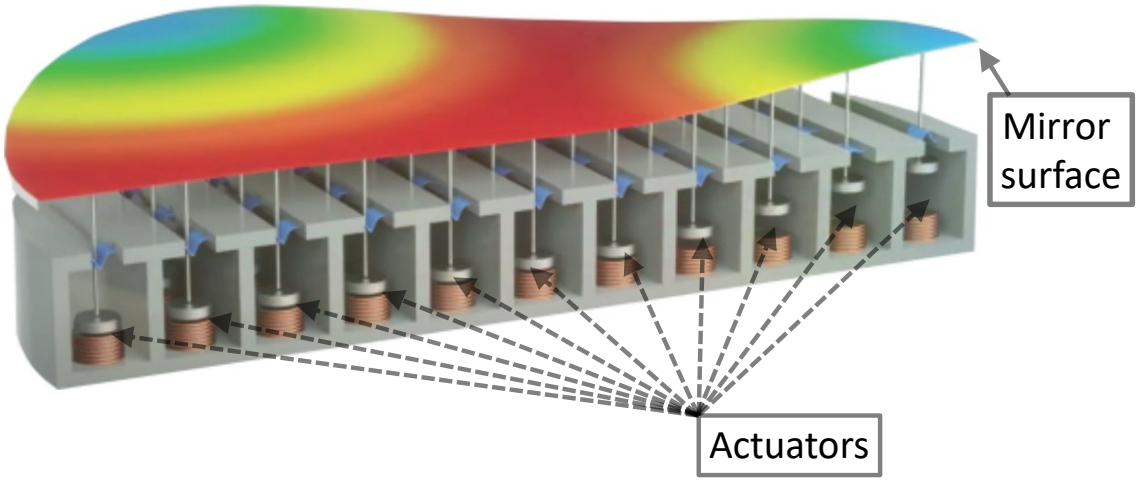


Figure 5.12: Conceptual diagram of the deformable mirror used in this project. Images from ALPAO's website [107]. Graphical image showing the mirror surface located at the centre of the device and the mechanism of the actuator attached to the back of the mirror. 69 independent actuators are evenly distributed in a grid on a 2D plane, each actuator can change its position independently, and the transverse mode of the beam can be modulated by reflected from the mirror surface according to the different position combinations of the 69 actuators.

spectral profile. The required parameters can change significantly from one QD to another, making the problem more complex. In setups using the resonant excitation method, one solution to improving the brightness of the source is to increase the coupling efficiency between the free space single photons and the single mode fibre that collects them. Typically the beam direction is adjusted by two mirrors in the free space between the beam reducer—telescope—and the fiber–coupler. However, this optimises only the alignment of the beam, but not the transverse spatial mode.

Figure 5.12 shows a deformable mirror that can change the surface shape depending on the programmed patterns. In this, 69 independent actuators are evenly distributed in a grid on a two-dimensional plane on the back side of this deformable mirror. Each independent actuator on the deformable mirror can adjust its position independently to change the transverse mode of the reflected beam. In a recent study, single-mode acquisition from InAs-QDs achieved up to 50% coupling increase was achieved with a deformable mirror and an automated optimisation via a genetic algorithm [106].

Figure 5.13 shows the layout of the test-setup in the single-photon collection path in our laboratory. The preliminary experiments Ref. [107] using this setup employing a deformable mirror (Adaptive Optics Deformable Mirrors, ALPAO) [108] to increase the collection efficiency of single photons for our QD–single photon sources. Maximising the single–photon collection efficiency by using the machine–learning algorithm is described in Ref. [107].

Single-photons emitted from the QD source sequentially pass through the objective lens, HWP4, and QWP. Single photons that pass through the PBS and go through a telescope (beam reducer) are coupled to a single-mode fibre. We install a BS on this edge (the path just before coupling to the single-mode fibre) so that half of it is coupled to the single-mode fibre, making it the coupling

reference. The other half is reflected from the BS and goes through a telescope (beam expander) to increase the size of the beam. The enlarged beam reaches the highly reflective and flexible surface of the DM surface, is reflected, passes through a telescope (beam reducer), and is coupled to a single-mode fibre. The number ratio of collected photons is measured using APD.

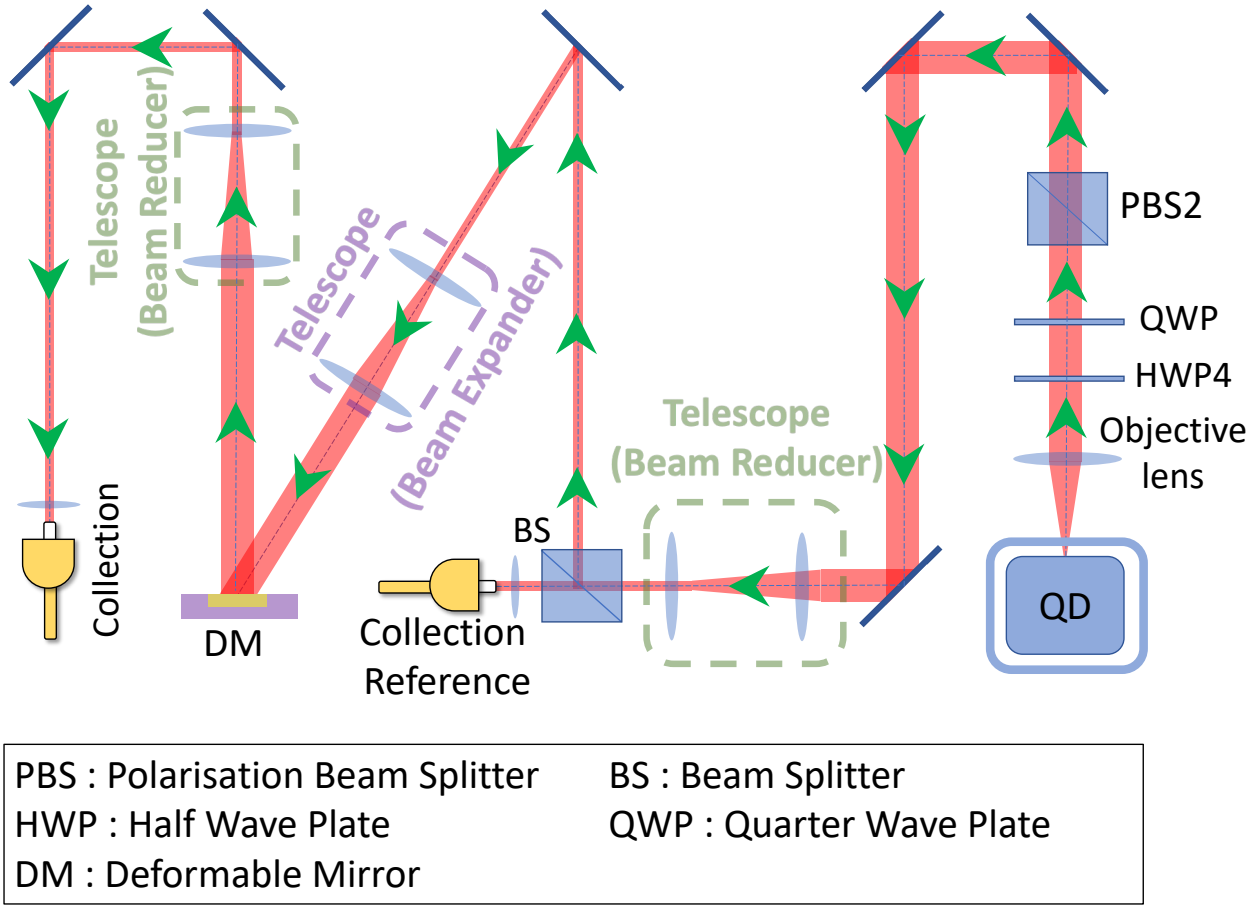


Figure 5.13: Single–photon collection system with deformable mirrors. Single–photons emitted through the top of the QD-micropillar structure pass through the cryostat glass window and the objective lens. The photons are randomly polarised, so only up to half pass through PBS2. A beam reducer is used to couple photons into a single-mode fibre. Half of the light reflected from the BS passes through the beam expander, is reflected off the deformable mirror surface, passes the beam reducer once more, and couples with the single-mode fibre. Meanwhile, half of the light passing through the BS is used as a reference by coupling with the other single-mode optical fibre.

Figure 5.14 shows the result of the ML optimisation of the collection efficiency by employing the deformable mirror for automation and time efficiency. When reflected pump light was used, the count rate increased by 31±3% from 1.27±0.02Hz to 1.67±0.03Hz. When single-photons were used, the count rate increased by 77±29% from 2.9±0.4Hz to 4.9±0.6Hz. When single photons are used in the ML process, the relatively high fluctuation range appears to be greatly affected by the single photon emission rate compared to when the reflected light is used. The reason is that when the reflected light is used, the count rate is sufficiently high even through attenuation, so it does not significantly affect the total photon count rate, so it can be seen as showing low volatility. On the other hand, when single-photon emission is used, it is thought to be highly responsive to minute changes in single-photon

emission because low count rates are measured under high purity and indistinguishable conditions. Despite such large fluctuations, the ML algorithm showed a $\sim 30\%$ and $\sim 70\%$ improvement in coupling efficiency when using reflected light and single-photon emission, respectively.

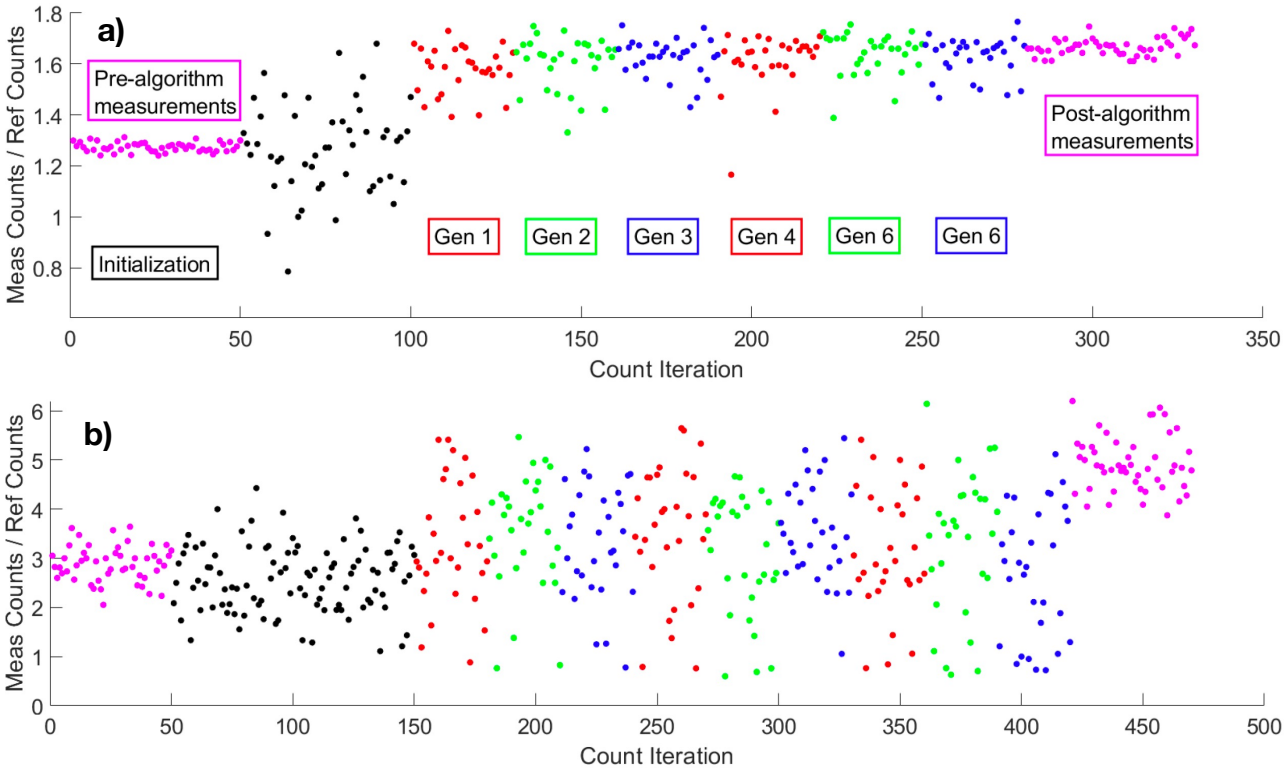


Figure 5.14: Machine–learning (ML) optimisation of single–photon count–rate by using the deformable mirrors. Image from Ref. [107]. a) Reflected pump light from the QD-micropillar cavity is used to run the optimisation for maximising the fibre–coupling efficiency. A fibre attenuator was used to reduce the collection of photons, in terms of avoiding damage on the APDs. (b) Single–photons from the QD-micropillar cavity are used to run the optimisation for maximising the fibre–coupling efficiency.

5.6 Conclusion

The optimisation process of parameters that determine the quality of a single photon source—$g^2(0)$, HOM-visibility, brightness—is automated using ML. As a result of ML optimisation in $g^2(0)$, the optimisation is achieved by reducing the single photon count rate, and a decrease in $g^2(0)$—in other words, an increase in single-photon purity—was observed. In the case of ML optimisation in HOM-visibility, the HOM-visibility is increased with the enhancement of the single photon count rate. The difference between the initial and the final visibility, Est.$(1- V_{\mathrm{HOM}})$, drops by a factor of two, from $> 16\%$ to 8%. Single–photon count rate in each of the measurements by using the parameters while reproducing the HOM–visibility result, note this increases by more than 3 times. This can be thought that the ML boost the efficiency of the single-photon production rate by achieving the higher HOM-visibility.

The final machine-learning optimisation process of parameters that determine the quality of a single photon source—$g^2(0)$, HOM-visibility was automated again to confirm the result of Sections 5.2 and 5.3. As a result of ML optimisation in the estimated $g^2(0)$, the optimisation was achieved by reducing the single photon count rate—from $\sim$220k to $\sim$70k. The estimated $g^2(0)$ decreases from $\sim$8.6% to $\sim$7.1%— around 1.5% increase in single-photon purity —was observed. The total optimisation process took about 9 hours. Compared to the HOM-visibility optimisation process, three more of the best optimisation parameters were found with the relatively stable Tsunami pump laser operation. The HOM-visibility was optimised and increased with the increase of the single–photon count rate. The difference between the initial and the final estimated visibility, Est.(1– V_{HOM}), drops from $>$ 16% to 12%. The results in Section 5.4 look slightly less optimised than those in Sections 5.2 and 5.3. However, the results of Section 5.4 are judged to be more reliable because more statistical considerations have been made than the results of Sections 5.2 and 5.3. In addition, since the code used in Section 5.4 has a fixed time per measurement, the overall ML measurement time can be systematically managed compared to the cumulative count-based code used in Section 5.2. The reason for the less-optimised steps in HOM-visibility compared to the steps in $g^2(0)$ can be interpreted as unstable pump pulse generation in the Tsunami pulsed pump laser for a certain period during the entire process of about 24 hours. The middle area of Figure 5.11 shows the large fluctuation of the values, which prevented further measurements. As a result of the HOM-visibility ML process, the single-photon count rate was improved from $\sim$32k to $\sim$58k. This trend——an increase of single-photon count rate through HOM-visibility ML—is similar to the trend shown in the preliminary HOM-visibility ML in Figure 5.4 c), Section 5.2. This can be thought of as ML achieving higher HOM visibility, increasing the efficiency of the single-photon production rate. The evolution of spectral FWHM in pulsed pump lasers has been minimal. This is thought to be because the initial value of the minimum bandwidth in which bandwidth reduction can no longer be made is given as an initial value. After all, optimisation of both HOM-visibility and $g^2(0)$ started at the stage of having the minimum FWHM spectrum. The good thing about this result is that our ML process can be thought of as an optimisation process that goes beyond the limits of spectral resolution that humans cannot distinguish. In addition, it was confirmed once again that it is necessary to be able to precisely monitor the temperature and humidity inside the pulsed laser to effectively achieve the optimisation due to stability. The stabilisation problem of this pulsed laser requires more research and is closely related to how to supply nitrogen gas stably and efficiently. In addition, this stabilisation is considered to be one of the important factors limiting the ML process time.

By installing a deformable mirror in the collection path of our system, we improved the outcoupling efficiency with single-mode fibre.

Ultimately, we provide a way to overcome the limitations of human capabilities through the optimisation of physical parameters using ML in QD single-photon. source system. Furthermore, we found that this optimisation process can be further improved in time efficiency with an automated optimisation system. Considering that most experimental results in scientific laboratories are generally created through countless hours of investment by numerous researchers, we can expect that machines

will be of great help to human life in the future.

Chapter 6

Discussion and Conclusion

Qubits are the fundamental building blocks for quantum computing or quantum information processing. Since single–photons can be used as qubits by utilising their characteristics of polarisation direction, time-bin, etc., they are one of the most ideal candidates as qubits for realising photonic quantum computation and communication, and information processing. For example, a scalable photonic quantum computer may be made solely out of single–photons, detectors, and linear optical networks in principle, with processing power increasing exponentially with the number of single photons handled [67]. Boson–sampling [63, 64], Heralded nondestructive entangling gate [104], and QKD with entangled photons generated on demand by a QD [66] have been already experimentally proven. Even, most recently, Boson–sampling, which conducted experiments with 20 single–photons fed to a 60-mode interferometer, has become possible [109]. To realise the above-mentioned all quantum technologies using single photons well, securing well-controlled, high-quality single-photons is the core and starting point of photonic quantum technology [110]. No matter how good quantum circuits, quantum algorithms, and high-performance single-photon detectors are provided, if deterministic single-photon sources are not excellent enough, it is difficult to expect good results.

Spontaneous parametric down-conversion (SPDC)—a traditional single–photon source that can generate two–photon entanglement [111]—has naturally high purity and high indistinguishability due to the nature of its generation mechanism, but its brightness is very low compared to the QD single photon source. Since single–photons occur simultaneously with a very low probability, there is a difficulty in practical application in quantum information and quantum computing. On the other hand, the on-demand QD single-photon sources have achieved a breakthrough in technology in recent years and have also achieved purity and indistinguishability comparable to that of an SPDC single photon source [1, 9]. In addition, the practicality of QD single-photon sources becomes even clearer with the use of techniques to improve source performance, as introduced in Chapter 3 of this thesis. Even recently, a deterministic single-photon source has been reported that can overcome noise and decoherence processes to reach the steep benchmarks on generation efficiency and photon indistinguishability by using a QD in an “on-chip” planar nanophotonic waveguide circuit [112]. Therefore, it is expected that more technology developments or platforms using solid-state QD-based deterministic

single-photon emitters than SPDC will appear in the future.

In this thesis, we focused on improving the performance of single-photon sources based on a solid–state QD. The research was conducted on how much the performance of the single-photon source in the form of micropillars can be improved from the point of view of the user, not the point of the manufacturer. The three parameters— suppression of multi-photon emission, photon indistinguishability, and source brightness —that judge the quality of single–photons from this source were considered to optimise as much as possible in Chapter 3. Manual spectrum shaping by using the pulse shaper promised us to reduce the noise from the pulsed pump laser, resulting in the lowest possible $g^2(0)$— 0.0068 ± 0.0004 (after pulse shaping) is measured with SNSPD —without background noise collection and etalon filter in the collection path. This means that our source can generate $>$99.99% purity single–photons. It's worth noting that we get $g^2(0)$ as close to the best as possible without employing an etalon. Because there is no spectral filtering loss imposed by an etalon, our source is significantly brighter. Also, world–class single–photon indistinguishability— HOM–visibility = 0.9468 ± 0.0003 (after pulse shaping) is measured with SNSPD —is achieved without background noise collection and etalon filter in the collection path. We investigated and analysed the relationship between the angle of the polariser and single photon counting so that the intensity of the pump laser can be adjusted according to the rotation angle of the polariser in our system for fast and systematic driving of our single–photon source. By creating our database, we have established a systematic control of pump power. This achievement allows for faster optimisation of the single-photon count rate, as the time required to find the π-pulse pump power that can optimally drive the source can be dramatically reduced. We built a temporal pulse multiplexing setup to use increasing the single-photon production rate. We confirmed that the repetition rate of the pump pulse can be doubled, and showed the possibility of realising the increase of single–photon production rate by a factor of eight. This opens the way to achieve faster data transfer and faster computation of the photonic circuit.

In addition to the resonant excitation of the QD, other possible optical excitation methods have been attempted utilising the programmable spectral pulse shaping function of the SLM. It has been demonstrated that our programmable spectral pulse shaper can drive single-photon sources with phonon-assisted excitation and coherent two-colour excitation. It is a great advantage to be able to implement various optical excitation methods with one spectral shaping protocol, and its usefulness is high. Because each optical excitation method has pros and cons, it is difficult to say that any specific optical excitation is superior. This is because if there is a need to change the method of operating the source according to the operation or purpose of the single–photon source, it can be flexibly dealt with. However, some improvements to the setup are required for practical use. For example, considering the setup of inputting an excitation laser to the side of the micropillar used in Ref. [113] and collecting single–photons from the top of the micropillar, we do not need to use the PBS used for resonance excitation. In other words, it is possible to prevent the output loss of single photons, so that brighter single–photons can be obtained. Coherently driven two-colour excitation, we identified the need for precise phase matching between the two colours, along with the preparation of a two-colour pump beam with well-separated spectra that do not overlap with the cavity–mode of the micropillars.

Similar to phonon-assisted excitation, we found that a better path system to filter the collected single-photon signal and mixed-pump laser is also essential for coherent two-colour excitation. Customised bandpass filter or etalon filter or placing a dichroic mirror at the PBS position can be the solutions to filter the excitation laser.

In Chapter 5, ML was considered to optimise all three desiderata. First-time multi–photon suppression and photon indistinguishability were optimised by ML employing the function of the programmable pulse shaper. Through the process of finding an optimised spectral pulse with an automated, machine-based accuracy that exceeds human capabilities, we demonstrated precise spectral pulse shaping that is difficult to distinguish with the smallest pixels of the spectrometer. The result of machine-based automatic optimisation of multi-photon suppression and photon indistinguishability is also competitive with the manual optimising result since we found the SLM configuration parameters which can be reproduced the $g^2(0)$= 0.0088 $\pm$ 0.005 and HOM-visibility = 0.92 $\pm$ 0.06, measured with APD. In particular, it is very surprising that this result was obtained using APD instead of SNSPD for $g^2(0)$ measurement in the ML process. Another surprising finding was that single-photon counting rates were simultaneously improved during ML optimisation of HOM–visibility. In addition, it was confirmed that the pump laser power used to start HOM-visibility ML was larger than the pump power when using the SLM configuration parameter found after the optimisation process. In other words, HOM-visibility ML optimisation provides a solution to excite the source using less energy to produce single photons with greater indistinguishability. Separately, to increase the collection efficiency of single–photons generated from the source, a deformable mirror was employed in the collection path, and ML was used to optimise the configuration of the deformable mirror. As a result, the fibre coupled single–photon count rate increased by 31$\pm$3% (from 1.27$\pm$0.02Hz to 1.67$\pm$0.03Hz). When single-photons were used, the count rate increased by 77$\pm$29% (from 2.9$\pm$0.4Hz to 4.9$\pm$0.6Hz). $\sim$ 30% and $\sim$ 70% improvement in coupling efficiency when using reflected light and single-photon emission, respectively. Therefore, it was confirmed that ML can automatically improve the single-mode fibre coupling efficiency.

We hope the overall single-photon source performance improvements achieved in this work contribute to large-scale demonstrations in quantum photonics. During the past years, we have seen an increase in the total number of qubits in quantum technology platforms such as superconducting qubits [114, 115, 116, 117, 118, 119] and ion traps [120, 121, 122, 123]. The key technical improvement to allow similar trends in quantum photonics [124, 125, 126, 127, 128], is to improve the generation of single-photons, allowing the realisation of multi-photon experiments involving large number of independent single-photons. Despite the demand for improvement of technical resources, we believe our results can aid the implementation of different quantum photonic applications. One example is the realisation of heralded entangling quantum photonic gates, also known as Type-II fusion–gate. This gate employs conditional detection of two ancillary independent optical qubits, to entangle two other qubits into a Bell-like quantum state. This gate is a key part of a quantum repeater, allowing it to extend the range of entanglement transmission through a quantum network. The first photonic quantum gate was first demonstrated, using single photons from spontaneous down-

conversion (SPDC) [129, 130] and more recently, using single photons from a QD source [104]. By replacing the probabilistic single photon generation of photons from the SPDC source with the deterministic generation in the QD source, it is possible now to generate 2-qubit entangled states at higher brightness and fidelity. Enhancing the purity, indistinguishability, and brightness of the single–photon produced by our QD source is a key requirement for the large-scale use of these entangling devices.

Note that, in 2019, our pump laser (Mode–locked Ti:sapphire laser, Tsunami, Spectra-physics) system experienced a breakdown, which resulted in a considerable delay in the progress of my research.

Bibliography

[1] N. Somaschi, V. Giesz, L. De Santis, J. Loredo, M. P. Almeida, G. Hornecker, S. L. Portalupi, T. Grange, C. Antón, J. Demory, et al. Near-optimal single-photon sources in the solid state. *Nature Photonics*, 10(5):340–345, 2016.

[2] S. L. Braunstein and C. M. Caves. Statistical distance and the geometry of quantum states. *Physical Review Letters*, 72(22):3439, 1994.

[3] P. W. Shor and J. Preskill. Simple proof of security of the bb84 quantum key distribution protocol. *Physical review letters*, 85(2):441, 2000.

[4] T. Kupko, M. von Helversen, L. Rickert, J.-H. Schulze, A. Strittmatter, M. Gschrey, S. Rodt, S. Reitzenstein, and T. Heindel. Tools for the performance optimization of single-photon quantum key distribution. *npj Quantum Information*, 6(1):1–8, 2020.

[5] N. Gershenfeld and I. L. Chuang. Quantum computing with molecules. *Scientific American*, 278(6):66–71, 1998.

[6] L. Mandel and E. Wolf. *Optical coherence and quantum optics*. Cambridge university press, 1995.

[7] D. F. Walls and G. J. Milburn. *Quantum optics*. Springer Science & Business Media, 2007.

[8] P. A. M. Dirac. The quantum theory of the emission and absorption of radiation. *Proceedings of the Royal Society of London. Series A, Containing Papers of a Mathematical and Physical Character*, 114(767):243–265, 1927.

[9] P. Senellart, G. Solomon, and A. White. High-performance semiconductor quantum-dot single-photon sources. *Nature nanotechnology*, 12(11):1026, 2017.

[10] G. Upton and I. Cook. *A dictionary of statistics 3e*. Oxford university press, 2014.

[11] G. Buller and R. Collins. Single-photon generation and detection. *Measurement Science and Technology*, 21(1):012002, 2009.

[12] R. H. Brown and R. Twiss. A test of a new type of stellar interferometer on sirius. *Nature*, 178(4541):1046–1048, 1956.

[13] C.-K. Hong, Z.-Y. Ou, and L. Mandel. Measurement of subpicosecond time intervals between two photons by interference. *Physical review letters*, 59(18):2044, 1987.

[14] C. H. Bennett and D. P. DiVincenzo. Quantum information and computation. *nature*, 404(6775):247–255, 2000.

[15] E. Meyer-Scott, C. Silberhorn, and A. Migdall. Single-photon sources: Approaching the ideal through multiplexing. *Review of Scientific Instruments*, 91(4):041101, 2020.

[16] X. Brokmann, L. Coolen, M. Dahan, and J. Hermier. Measurement of the radiative and non-radiative decay rates of single cdse nanocrystals through a controlled modification of their spontaneous emission. *Physical Review Letters*, 93(10):107403, 2004.

[17] M. Nirmal, B. O. Dabbousi, M. G. Bawendi, J. Macklin, J. Trautman, T. Harris, and L. E. Brus. Fluorescence intermittency in single cadmium selenide nanocrystals. *Nature*, 383(6603):802–804, 1996.

[18] M. Kuno, D. P. Fromm, H. F. Hamann, A. Gallagher, and D. J. Nesbitt. Nonexponential "blinking" kinetics of single cdse quantum dots: A universal power law behavior. *The journal of chemical physics*, 112(7):3117–3120, 2000.

[19] P. Frantsuzov, M. Kuno, B. Janko, and R. A. Marcus. Universal emission intermittency in quantum dots, nanorods and nanowires. *Nature Physics*, 4(7):519–522, 2008.

[20] X. Wang, X. Ren, K. Kahen, M. A. Hahn, M. Rajeswaran, S. Maccagnano-Zacher, J. Silcox, G. E. Cragg, A. L. Efros, and T. D. Krauss. Non-blinking semiconductor nanocrystals. *Nature*, 459(7247):686–689, 2009.

[21] V. Fomenko and D. J. Nesbitt. Solution control of radiative and nonradiative lifetimes: A novel contribution to quantum dot blinking suppression. *Nano Letters*, 8(1):287–293, 2008.

[22] K. L. Knappenberger, D. B. Wong, Y. E. Romanyuk, and S. R. Leone. Excitation wavelength dependence of fluorescence intermittency in cdse/zns core/shell quantum dots. *Nano letters*, 7(12):3869–3874, 2007.

[23] K. Ozasa, S. Nemoto, M. Maeda, and M. Hara. Excitation-wavelength-dependent photoluminescence evolution of cdse/ zns nanoparticles. *Journal of applied physics*, 101(10), 2007.

[24] J. J. Peterson and D. J. Nesbitt. Modified power law behavior in quantum dot blinking: a novel role for biexcitons and auger ionization. *Nano letters*, 9(1):338–345, 2009.

[25] A. A. Cordones, T. J. Bixby, and S. R. Leone. Evidence for multiple trapping mechanisms in single cdse/zns quantum dots from fluorescence intermittency measurements over a wide range of excitation intensities. *The Journal of Physical Chemistry C*, 115(14):6341–6349, 2011.

[26] A. L. Efros and M. Rosen. Random telegraph signal in the photoluminescence intensity of a single quantum dot. *Physical review letters*, 78(6):1110, 1997.

[27] J. A. Smyder, A. R. Amori, M. Y. Odoi, H. A. Stern, J. J. Peterson, and T. D. Krauss. The influence of continuous vs. pulsed laser excitation on single quantum dot photophysics. *Physical Chemistry Chemical Physics*, 16(47):25723–25728, 2014.

[28] L. Jacak, P. Hawrylak, and A. Wojs. *Quantum dots*. Springer Science & Business Media, 2013.

[29] A. M. Smith and S. Nie. Semiconductor nanocrystals: structure, properties, and band gap engineering. *Accounts of chemical research*, 43(2):190–200, 2010.

[30] R. Ashoori. Electrons in artificial atoms. *Nature*, 379(6564):413–419, 1996.

[31] G. S. Agarwal. Quantum statistical theories of spontaneous emission and their relation to other approaches. In *Quantum Optics*, pages 1–128. Springer, 1974.

[32] J. Bylander, I. Robert-Philip, and I. Abram. Interference and correlation of two independent photons. *The European Physical Journal D-Atomic, Molecular, Optical and Plasma Physics*, 22(2):295–301, 2003.

[33] C. Santori, M. Pelton, G. Solomon, Y. Dale, and Y. Yamamoto. Triggered single photons from a quantum dot. *Physical Review Letters*, 86(8):1502, 2001.

[34] J. C. Loredo, N. A. Zakaria, N. Somaschi, C. Anton, L. De Santis, V. Giesz, T. Grange, M. A. Broome, O. Gazzano, G. Coppola, et al. Scalable performance in solid-state single-photon sources. *Optica*, 3(4):433–440, 2016.

[35] X. Ding, Y. He, Z.-C. Duan, N. Gregersen, M.-C. Chen, S. Unsleber, S. Maier, C. Schneider, M. Kamp, S. Höfling, et al. On-demand single photons with high extraction efficiency and near-unity indistinguishability from a resonantly driven quantum dot in a micropillar. *Physical review letters*, 116(2):020401, 2016.

[36] H. Ollivier, S. Thomas, S. Wein, I. M. de Buy Wenniger, N. Coste, J. Loredo, N. Somaschi, A. Harouri, A. Lemaitre, I. Sagnes, et al. Hong-ou-mandel interference with imperfect single photon sources. *Physical Review Letters*, 126(6):063602, 2021.

[37] Y. Yamamoto, F. Tassone, and H. Cao. *Semiconductor cavity quantum electrodynamics*, volume 169. Springer, 2003.

[38] G. Agarwal. Master-equation approach to spontaneous emission. *Physical Review A*, 2(5):2038, 1970.

[39] H.-P. Breuer, F. Petruccione, et al. *The theory of open quantum systems*. Oxford University Press on Demand, 2002.

[40] V. Weisskopf and E. Wigner. Calculation of the natural line width based on dirac's light theory. In *Part I: Particles and Fields. Part II: Foundations of Quantum Mechanics*, pages 30–49. springer, 1997.

[41] E. Fermi. Quantum theory of radiation. *Reviews of modern physics*, 4(1):87, 1932.

[42] H. Yokoyama and K. Ujihara. *Spontaneous emission and laser oscillation in microcavities*, volume 10. CRC press, 1995.

[43] H. L. Luk, J. Feist, J. J. Toppari, and G. Groenhof. Multiscale molecular dynamics simulations of polaritonic chemistry. *Journal of chemical theory and computation*, 13(9):4324–4335, 2017.

[44] E. M. Purcell. Spontaneous emission probabilities at radio frequencies. In *Confined Electrons and Photons*, pages 839–839. Springer, 1995.

[45] C. Santori, D. Fattal, J. Vučković, G. S. Solomon, and Y. Yamamoto. Indistinguishable photons from a single-photon device. *nature*, 419(6907):594–597, 2002.

[46] C. Sheppard. Approximate calculation of the reflection coefficient from a stratified medium. *Pure and Applied Optics: Journal of the European Optical Society Part A*, 4(5):665, 1995.

[47] C. W. Wilmsen, H. Temkin, and L. A. Coldren. *Vertical-cavity surface-emitting lasers: design, fabrication, characterization, and applications*, volume 24. Cambridge University Press, 2001.

[48] K. Iga. Vertical-cavity surface-emitting laser: Its conception and evolution. *Japanese Journal of Applied Physics*, 47(1R):1, 2008.

[49] S. L. Chuang. *Physics of photonic devices*, volume 80. John Wiley & Sons, 2012.

[50] L. Seravalli, M. Minelli, P. Frigeri, S. Franchi, G. Guizzetti, M. Patrini, T. Ciabattoni, and M. Geddo. Quantum dot strain engineering of in as/ in ga as nanostructures. *Journal of applied physics*, 101(2):024313, 2007.

[51] J. P. Reithmaier, G. Sek, A. Löffler, C. Hofmann, S. Kuhn, S. Reitzenstein, L. Keldysh, V. Kulakovskii, T. Reinecke, and A. Forchel. Strong coupling in a single quantum dot–semiconductor microcavity system. *Nature*, 432(7014):197–200, 2004.

[52] O. Gazzano, S. M. De Vasconcellos, C. Arnold, A. Nowak, E. Galopin, I. Sagnes, L. Lanco, A. Lemaître, and P. Senellart. Bright solid-state sources of indistinguishable single photons. *Nature communications*, 4(1):1–6, 2013.

[53] A. Dousse, L. Lanco, J. Suffczyński, E. Semenova, A. Miard, A. Lemaître, I. Sagnes, C. Roblin, J. Bloch, and P. Senellart. Controlled light-matter coupling for a single quantum dot embedded in a pillar microcavity using far-field optical lithography. *Physical review letters*, 101(26):267404, 2008.

[54] K. A. Fischer, L. Hanschke, M. Kremser, J. J. Finley, K. Müller, and J. Vučković. Pulsed rabi oscillations in quantum two-level systems: beyond the area theorem. *Quantum Science and Technology*, 3(1):014006, 2017.

[55] G. Gol'Tsman, O. Okunev, G. Chulkova, A. Lipatov, A. Semenov, K. Smirnov, B. Voronov, A. Dzardanov, C. Williams, and R. Sobolewski. Picosecond superconducting single-photon optical detector. *Applied physics letters*, 79(6):705–707, 2001.

[56] A. D. Semenov, G. N. Gol'tsman, and A. A. Korneev. Quantum detection by current carrying superconducting film. *Physica C: Superconductivity*, 351(4):349–356, 2001.

[57] K. Irwin. An application of electrothermal feedback for high resolution cryogenic particle detection. *Applied Physics Letters*, 66(15):1998–2000, 1995.

[58] A. Peacock, P. Verhoeve, N. Rando, A. Van Dordrecht, B. Taylor, C. Erd, M. Perryman, R. Venn, J. Howlett, D. Goldie, et al. Single optical photon detection with a superconducting tunnel junction. *Nature*, 381(6578):135–137, 1996.

[59] P. K. Day, H. G. LeDuc, B. A. Mazin, A. Vayonakis, and J. Zmuidzinas. A broadband superconducting detector suitable for use in large arrays. *Nature*, 425(6960):817–821, 2003.

[60] C. M. Natarajan, M. G. Tanner, and R. H. Hadfield. Superconducting nanowire single-photon detectors: physics and applications. *Superconductor science and technology*, 25(6):063001, 2012.

[61] H. Ollivier, I. Maillette de Buy Wenniger, S. Thomas, S. C. Wein, A. Harouri, G. Coppola, P. Hilaire, C. Millet, A. Lemaître, I. Sagnes, et al. Reproducibility of high-performance quantum dot single-photon sources. *ACS photonics*, 7(4):1050–1059, 2020.

[62] H. Wang, Y.-M. He, T.-H. Chung, H. Hu, Y. Yu, S. Chen, X. Ding, M.-C. Chen, J. Qin, X. Yang, et al. Towards optimal single-photon sources from polarized microcavities. *Nature Photonics*, 13(11):770–775, 2019.

[63] J. Loredo, M. Broome, P. Hilaire, O. Gazzano, I. Sagnes, A. Lemaitre, M. Almeida, P. Senellart, and A. White. Boson sampling with single-photon fock states from a bright solid-state source. *Physical review letters*, 118(13):130503, 2017.

[64] H. Wang, Y. He, Y.-H. Li, Z.-E. Su, B. Li, H.-L. Huang, X. Ding, M.-C. Chen, C. Liu, J. Qin, et al. High-efficiency multiphoton boson sampling. *Nature Photonics*, 11(6):361–365, 2017.

[65] S.-K. Liao, W.-Q. Cai, W.-Y. Liu, L. Zhang, Y. Li, J.-G. Ren, J. Yin, Q. Shen, Y. Cao, Z.-P. Li, et al. Satellite-to-ground quantum key distribution. *Nature*, 549(7670):43–47, 2017.

[66] F. B. Basset, M. Valeri, E. Roccia, V. Muredda, D. Poderini, J. Neuwirth, N. Spagnolo, M. B. Rota, G. Carvacho, F. Sciarrino, et al. Quantum key distribution with entangled photons generated on demand by a quantum dot. *Science Advances*, 7(12):eabe6379, 2021.

[67] E. Knill, R. Laflamme, and G. J. Milburn. A scheme for efficient quantum computation with linear optics. *nature*, 409(6816):46–52, 2001.

[68] P. Hilaire, C. Antón, C. Kessler, A. Lemaître, I. Sagnes, N. Somaschi, P. Senellart, and L. Lanco. Accurate measurement of a 96% input coupling into a cavity using polarization tomography. *Applied Physics Letters*, 112(20):201101, 2018.

[69] D. Strickland and G. Mourou. Compression of amplified chirped optical pulses. *Optics communications*, 55(6):447–449, 1985.

[70] T. Oksenhendler and N. Forget. Pulse-shaping techniques theory and experimental implementations for femtosecond pulses. Technical report, ISBN 978–953–7619–80–0, 2010.

[71] A. Monmayrant, S. Weber, B. Chatel, et al. A newcomer's guide to ultrashort pulse shaping and characterization. *J. Phys. B*, 43(10):103001, 2010.

[72] F. Gires and P. Tournois. Interferometre utilisable pour la compression dimpulsions lumineuses modulees en frequence. *Comptes Rendus Hebdomadaires Des Seances De L Academie Des Sciences*, 258(25):6112, 1964.

[73] A. M. Weiner, D. E. Leaird, J. S. Patel, and J. R. Wullert. Programmable femtosecond pulse shaping by use of a multielement liquid-crystal phase modulator. *Optics letters*, 15(6):326–328, 1990.

[74] A. M. Weiner, D. E. Leaird, J. Patel, and J. R. Wullert. Programmable shaping of femtosecond optical pulses by use of 128-element liquid crystal phase modulator. *IEEE journal of quantum electronics*, 28(4):908–920, 1992.

[75] E. Frumker and Y. Silberberg. Phase and amplitude pulse shaping with two-dimensional phase-only spatial light modulators. *JOSA B*, 24(12):2940–2947, 2007.

[76] T. Feurer, J. C. Vaughan, R. M. Koehl, and K. A. Nelson. Multidimensional control of femtosecond pulses by use of a programmable liquid-crystal matrix. *Optics letters*, 27(8):652–654, 2002.

[77] J. C. Vaughan, T. Feurer, and K. A. Nelson. Automated spatiotemporal diffraction of ultrashort laser pulses. *Optics letters*, 28(23):2408–2410, 2003.

[78] M. A. Broome, M. P. Almeida, A. Fedrizzi, and A. G. White. Reducing multi-photon rates in pulsed down-conversion by temporal multiplexing. *Optics express*, 19(23):22698–22708, 2011.

[79] L. Lanco and P. Senellart. A highly efficient single photon-single quantum dot interface. In *Engineering the Atom-Photon Interaction*, pages 39–71. Springer, 2015.

[80] L. M. Hansen, L. Carosini, L. Jehle, F. Giorgino, R. Houvenaghel, M. Vyvlecka, J. C. Loredo, and P. Walther. Single-active-element demultiplexed multi-photon source. *Optica Quantum*, 1(1):1–5, Oct 2023.

[81] A. M. Barth, S. Lüker, A. Vagov, D. Reiter, T. Kuhn, and V. M. Axt. Fast and selective phonon-assisted state preparation of a quantum dot by adiabatic undressing. *Physical Review B*, 94(4):045306, 2016.

[82] M. Reindl, J. H. Weber, D. Huber, C. Schimpf, S. F. C. da Silva, S. L. Portalupi, R. Trotta, P. Michler, and A. Rastelli. Highly indistinguishable single photons from incoherently excited quantum dots. *Physical Review B*, 100(15):155420, 2019.

[83] C. Gustin and S. Hughes. Efficient pulse-excitation techniques for single photon sources from quantum dots in optical cavities. *Advanced Quantum Technologies*, 3(2):1900073, 2020.

[84] M. Bayer, G. Ortner, O. Stern, A. Kuther, A. Gorbunov, A. Forchel, P. Hawrylak, S. Fafard, K. Hinzer, T. Reinecke, et al. Fine structure of neutral and charged excitons in self-assembled in (ga) as/(al) gaas quantum dots. *Physical Review B*, 65(19):195315, 2002.

[85] M. Cosacchi, F. Ungar, M. Cygorek, A. Vagov, and V. M. Axt. Emission-frequency separated high quality single-photon sources enabled by phonons. *Physical review letters*, 123(1):017403, 2019.

[86] J. H. Quilter, A. Brash, F. Liu, M. Glässl, A. M. Barth, V. M. Axt, A. Ramsay, M. Skolnick, and A. Fox. Phonon-assisted population inversion of a single ingaas/gaas quantum dot by pulsed laser excitation. *Physical review letters*, 114(13):137401, 2015.

[87] S. Thomas, M. Billard, N. Coste, S. Wein, P. Priya, H. Ollivier, O. Krebs, L. Tazaïrt, A. Harouri, A. Lemaıtre, et al. Bright polarized single-photon source based on a linear dipole. 2020.

[88] Y.-M. He, H. Wang, C. Wang, M.-C. Chen, X. Ding, J. Qin, Z.-C. Duan, S. Chen, J.-P. Li, R.-Z. Liu, et al. Coherently driving a single quantum two-level system with dichromatic laser pulses. *Nature Physics*, 15(9):941–946, 2019.

[89] A. Ramsay, T. Godden, S. Boyle, E. Gauger, A. Nazir, B. Lovett, A. V. Gopal, A. Fox, and M. Skolnick. Effect of detuning on the phonon induced dephasing of optically driven ingaas/gaas quantum dots. *Journal of Applied Physics*, 109(10):102415, 2011.

[90] R. Anderson, H. Bilger, and G. Stedman. "sagnac"effect: A century of earth-rotated interferometers. *American Journal of Physics*, 62(11):975–985, 1994.

[91] M. Galván-Sosa, J. Portilla, J. Hernandez-Rueda, J. Siegel, L. Moreno, A. R. de la Cruz, and J. Solis. Optimization of ultra-fast interactions using laser pulse temporal shaping controlled by a deterministic algorithm. *Applied Physics A*, 114(2):477–484, 2014.

[92] N. Accanto, P. M. De Roque, M. Galvan-Sosa, S. Christodoulou, I. Moreels, and N. F. Van Hulst. Rapid and robust control of single quantum dots. *Light: Science & Applications*, 6(3):e16239–e16239, 2017.

[93] A. D. Tranter, H. J. Slatyer, M. R. Hush, A. C. Leung, J. L. Everett, K. V. Paul, P. Vernaz-Gris, P. K. Lam, B. C. Buchler, and G. T. Campbell. Multiparameter optimisation of a magneto-optical trap using deep learning. *Nature communications*, 9(1):1–8, 2018.

[94] H. Hush, M. R. Slatyer. M-loop. `https://github.com/charmasaur/M-LOOP.git`. Accessed: 2023-11-27.

[95] R. Fletcher. *Practical methods of optimization*. John Wiley & Sons, 2000.

[96] C. M. Bishop and N. M. Nasrabadi. *Pattern recognition and machine learning*, volume 4. Springer, 2006.

[97] C. E. Rasmussen, C. K. Williams, et al. *Gaussian processes for machine learning*, volume 1. Springer, 2006.

[98] J. Schmidhuber. Deep learning in neural networks: An overview. *Neural networks*, 61:85–117, 2015.

[99] M. A. Nielsen. *Neural networks and deep learning*, volume 25. Determination press San Francisco, CA, USA, 2015.

[100] C. C. Aggarwal et al. Neural networks and deep learning. *Springer*, 10:978–3, 2018.

[101] O. I. Abiodun, A. Jantan, A. E. Omolara, K. V. Dada, N. A. Mohamed, and H. Arshad. State-of-the-art in artificial neural network applications: A survey. *Heliyon*, 4(11):e00938, 2018.

[102] L. V. Jospin, H. Laga, F. Boussaid, W. Buntine, and M. Bennamoun. Hands-on bayesian neural networks—a tutorial for deep learning users. *IEEE Computational Intelligence Magazine*, 17(2):29–48, 2022.

[103] G. E. Box and G. C. Tiao. *Bayesian inference in statistical analysis*. John Wiley & Sons, 2011.

[104] J.-P. Li, X. Gu, J. Qin, D. Wu, X. You, H. Wang, C. Schneider, S. Höfling, Y.-H. Huo, C.-Y. Lu, et al. Heralded nondestructive quantum entangling gate with single-photon sources. *Physical Review Letters*, 126(14):140501, 2021.

[105] L. Hanschke, K. A. Fischer, S. Appel, D. Lukin, J. Wierzbowski, S. Sun, R. Trivedi, J. Vučković, J. J. Finley, and K. Müller. Quantum dot single-photon sources with ultra-low multi-photon probability. *npj Quantum Information*, 4(1):1–6, 2018.

[106] A. D. Hill, D. Hervas, J. Nash, M. Graham, A. Burgers, U. Paudel, D. Steel, C. Schneider, M. Kamp, S. Höfling, et al. Optimizing single-mode collection from pointlike sources of single photons with adaptive optics. *Optics express*, 25(16):18629–18642, 2017.

[107] S. Malewicz. Implementation of adaptive optics to maximize single-photon collection efficiency. Master's thesis, The University of Queensland, 2021.

[108] Alpao deformable modal mirror. `https://www.alpao.com/products-and-services/deformable-mirrors/`. Accessed: 2021-10-12.

[109] H. Wang, J. Qin, X. Ding, M.-C. Chen, S. Chen, X. You, Y.-M. He, X. Jiang, L. You, Z. Wang, et al. Boson sampling with 20 input photons and a 60-mode interferometer in a 1 0 14-dimensional hilbert space. *Physical review letters*, 123(25):250503, 2019.

[110] J. L. O'brien, A. Furusawa, and J. Vučković. Photonic quantum technologies. *Nature Photonics*, 3(12):687–695, 2009.

[111] T. E. Keller and M. H. Rubin. Theory of two-photon entanglement for spontaneous parametric down-conversion driven by a narrow pump pulse. *Physical Review A*, 56(2):1534, 1997.

[112] R. Uppu, F. T. Pedersen, Y. Wang, C. T. Olesen, C. Papon, X. Zhou, L. Midolo, S. Scholz, A. D. Wieck, A. Ludwig, et al. Scalable integrated single-photon source. *Science advances*, 6(50):eabc8268, 2020.

[113] S. Ates, S. Ulrich, S. Reitzenstein, A. Löffler, A. Forchel, and P. Michler. Post-selected indistinguishable photons from the resonance fluorescence of a single quantum dot in a microcavity. *Physical Review Letters*, 103(16):167402, 2009.

[114] J. Majer, J. Chow, J. Gambetta, J. Koch, B. Johnson, J. Schreier, L. Frunzio, D. Schuster, A. A. Houck, A. Wallraff, et al. Coupling superconducting qubits via a cavity bus. *Nature*, 449(7161):443–447, 2007.

[115] M. Kjaergaard, M. E. Schwartz, J. Braumüller, P. Krantz, J. I.-J. Wang, S. Gustavsson, and W. D. Oliver. Superconducting qubits: Current state of play. *Annual Review of Condensed Matter Physics*, 11:369–395, 2020.

[116] Y. Wang, Y. Li, Z.-q. Yin, and B. Zeng. 16-qubit ibm universal quantum computer can be fully entangled. *npj Quantum information*, 4(1):1–6, 2018.

[117] D. Castelvecchi. Quantum computers ready to leap out of the lab in 2017. *Nature News*, 541(7635):9, 2017.

[118] F. Arute, K. Arya, R. Babbush, D. Bacon, J. C. Bardin, R. Barends, R. Biswas, S. Boixo, F. G. Brandao, D. A. Buell, et al. Quantum supremacy using a programmable superconducting processor. *Nature*, 574(7779):505–510, 2019.

[119] C. Vu. Ibm makes quantum computing available on ibm cloud to accelerate innovation. *IBM News Room*, 2016.

[120] N. Friis, O. Marty, C. Maier, C. Hempel, M. Holzäpfel, P. Jurcevic, M. B. Plenio, M. Huber, C. Roos, R. Blatt, et al. Observation of entangled states of a fully controlled 20-qubit system. *Physical Review X*, 8(2):021012, 2018.

[121] T. Monz, P. Schindler, J. T. Barreiro, M. Chwalla, D. Nigg, W. A. Coish, M. Harlander, W. Hänsel, M. Hennrich, and R. Blatt. 14-qubit entanglement: Creation and coherence. *Physical Review Letters*, 106(13):130506, 2011.

[122] J. I. Cirac and P. Zoller. Quantum computations with cold trapped ions. *Physical review letters*, 74(20):4091, 1995.

[123] D. Kielpinski, C. Monroe, and D. J. Wineland. Architecture for a large-scale ion-trap quantum computer. *Nature*, 417(6890):709–711, 2002.

[124] G. Hutchinson and G. Milburn. Nonlinear quantum optical computing via measurement. *Journal of Modern Optics*, 51(8):1211–1222, 2004.

[125] A. Politi, M. J. Cryan, J. G. Rarity, S. Yu, and J. L. O'brien. Silica-on-silicon waveguide quantum circuits. *Science*, 320(5876):646–649, 2008.

[126] M. G. Thompson, A. Politi, J. C. Matthews, and J. L. O'Brien. Integrated waveguide circuits for optical quantum computing. *IET circuits, devices & systems*, 5(2):94–102, 2011.

[127] P. Kok, W. J. Munro, K. Nemoto, T. C. Ralph, J. P. Dowling, and G. J. Milburn. Linear optical quantum computing with photonic qubits. *Reviews of modern physics*, 79(1):135, 2007.

[128] J. L. O'brien. Optical quantum computing. *Science*, 318(5856):1567–1570, 2007.

[129] J.-W. Pan, D. Bouwmeester, H. Weinfurter, and A. Zeilinger. Experimental entanglement swapping: entangling photons that never interacted. *Physical review letters*, 80(18):3891, 1998.

[130] Q. Zhang, X.-H. Bao, C.-Y. Lu, X.-Q. Zhou, T. Yang, T. Rudolph, and J.-W. Pan. Demonstration of a scheme for the generation of "event-ready" entangled photon pairs from a single-photon source. *Physical Review A*, 77(6):062316, 2008.

Appendix A

Machine Learning Code

These codes are used to run machine learning in Chapter 5.

A.1 $g^2(0)$ calculation in *Python*

```
import numpy as np
from scipy.signal import find_peaks


def g2_calc(cc):
    Hist= np.histogram(cc,1000) #Bulding a histogram Frequency/Time Tag

    time_tag=Hist[1][0:1000]/(1e-9)-np.max(Hist[1][0:1000]/(1e-9))/2
     #Converting time tag to interval -100-100ns

    Freq=Hist[0]
    peaks, _ = find_peaks(Freq , distance=50) #Finding peaks

    z=0
    for i in range(0,len(peaks)-1):
        if Freq[peaks[i]]<0.5*Freq[peaks[i+1]]:
            z=i #This loop will search for the peaks located on the left
            and right of the zero delay

    delta=25 #total points used to calculate the area

    Y_zero=Freq[peaks[z]-delta:peaks[z]+delta]
```

```
    a_zero=np.sum(Y_zero) #area of the peak at zero delay

    Y_m=np.zeros((2*delta,z))
    Y_p=np.zeros((2*delta,z))
    a_m=np.zeros(z)
    a_p=np.zeros(z)



    #this loop calculates the areas of the peaks on the left and right with
     respect to the zero delay
    print(Y_p.shape)
    for i in range(z-1):
        print(i, len(Freq[peaks[z+1+i]-delta:peaks[z+1+i]+delta]))
        Y_m[:,i]=Freq[peaks[z-1-i]-delta:peaks[z-1-i]+delta]
        Y_p[:,i]=Freq[peaks[z+1+i]-delta:peaks[z+1+i]+delta]
        a_m[i]=np.sum(Y_m[:,i])
        a_p[i]=np.sum(Y_p[:,i])


a_m_tot=np.mean(a_m) #total areas left
a_p_tot=np.mean(a_p) #total areas right


g_2=100*a_zero/((a_m_tot+a_p_tot)/2) #g2 estimate value

    #err_g_2=g_2*np.sqrt((2*area_zero_err**2/(area_minus_av+area_plus_av))**2
    #         +(2*area_zero_av*area_minus_err/(area_minus_av+area_plus_av))**2
    #         +(2*area_zero_av*area_plus_err/(area_minus_av+area_plus_av))**2)

return g_2
```

A.2 HOM–visibility calculation in *Python*

```
import numpy as np
from scipy.signal import find_peaks
```

```
def hom_calc(cc):



    Hist= np.histogram(cc,1000) #Bulding a histogram Frequency/Time Tag

    time_tag=Hist[1][0:1000]/(1e-9)-np.max(Hist[1][0:1000]/(1e-9))/2
        #Converting time tag to interval -100-100ns

    Freq=Hist[0]

    peaks, _ = find_peaks(Freq , distance=50) #Finding peaks

    z=0

    #This loop will search for the peaks located on the left and right
     of the zero delay
    for i in range(0,len(peaks)-1):
        if Freq[peaks[i]]<0.5*Freq[peaks[i+1]]:
            z=i

    delta=25#total points used to calculate the are



    Y_zero=Freq[peaks[z]-delta:peaks[z]+delta]

    a_zero=np.sum(Y_zero)#area of the peak at zero delay

    Y_m=np.zeros((2*delta,z))
    Y_p=np.zeros((2*delta,z))
    a_m=np.zeros(z)
    a_p=np.zeros(z)

    #this loop calculates the areas of the peaks on the left and right
     with respect to the zero delay
    print(Y_p.shape)
    for i in range(z-2):
        print(i, len(Freq[peaks[z+2+i]-delta:peaks[z+2+i]+delta]))
```

```
        Y_m[:,i]=Freq[peaks[z-2-i]-delta:peaks[z-2-i]+delta]
        Y_p[:,i]=Freq[peaks[z+2+i]-delta:peaks[z+2+i]+delta]
        a_m[i]=np.sum(Y_m[:,i])
        a_p[i]=np.sum(Y_p[:,i])


    a_m_tot=np.mean(a_m) #total areas left
    a_p_tot=np.mean(a_p) #total areas right


HOM_e=100*a_zero/((a_m_tot+a_p_tot)/2) #HOM visibility estimate value

#    err_g_2=g_2*np.sqrt((2*area_zero_err**2/(area_minus_av+area_plus_av))
#             **2
#             +(2*area_zero_av*area_minus_err/(area_minus_av+area_plus_av))
#             **2
#             +(2*area_zero_av*area_plus_err/(area_minus_av+area_plus_av))
#             **2)

return HOM_e
```

A.3 SLM mask in *Python*

```
#----------BELOW CONTAINS FUNCTIONS FOR THE ML ALGORITHM-------------------------

import numpy as np
import numpy.random as r
import matplotlib.pyplot as plt
from time import sleep
import cv2 #OpenCV
from numpy import savetxt
#import screeninfo
import os
#from scipy.signal import find_peaks
import time

#----------------------PIXEL ARRAY TO SLM----------------------------------
#For this to work set the second monitor as the main monitor
#and duplicate that monitor to the SLM display.
```

```
#create an array for passing to cv2 and placing on SLM screen.
#screen=screeninfo.get_monitors()[1]
#print(screen)

#width, height = screen.width, screen.height
#print('SLM screen width ',width)
#print('SLM screen height ',height)

#---------CREATES THE NARROWBAND SPECTRUM WITH PARAMETER-CONTROL--------------
size = 512

pi = np.pi

alpha = 2.0*pi  #Maximum appliable phase of SLM.

d = 0.01    #Period of sawtooth pattern on SLM. 0.01 is 8 pixels per ramp.

a = 0.5 #amplitue of sawtooth pattern.
x = np.linspace(0,1,512)
pixel_width = 512   #This is the horizontal pixel width on SLM window.


params = np.zeros(10)

params = [0, 0, 0, 1, 1, 1, 1, 1, 0, 0, 0, 0, 0, 5, 5, 5, 5, 5, 0, 0]

#HOM200s_1params =
[0.5858585858585859, 0.4612794612794613, 0.34006734006734013,
0.5757575757575757, 0.5858585858585859, 0.4713804713804714,
0.4814814814814815,0.3703703703703704, 0.35690235690235694,
0.5791245791245792, 2.179017126732315, 2.4540387058344515,
2.644438260597469, 3.7022135648364562, 3.469502997903879,
3.3848809735647603, 2.136706114562755, 3.6387470465821172,
3.913768625684254, 3.892613119599474]

#HOM200s_2params =
[0.5555555555555556, 0.4107744107744108, 0.5925925925925926,
0.494949494949495, 0.494949494949495, 0.5656565656565656,
```

```
0.5387205387205387, 0.5084175084175084, 0.5185185185185185,
0.5925925925925926, 4.040701662192932, 4.0618571682777125,
3.8079910952603555, 3.892613119599474, 3.0675483822930643,
3.5329695161582184, 3.5118140100734387, 3.575280528327778,
3.8079910952603555, 2.179017126732315]

#HOM200s_3params =
[0.44276094276094274, 0.5774410774410774, 0.7255892255892256,
0.3484848484848485, 0.4225589225589225, 0.30134680134680136,
0.5168350168350169, 0.765993265993266, 0.20033670033670034,
0.7255892255892256, 4.051279415235322, 2.274216904113823,
4.728255609948274, 3.37430322052237, 4.770566622117833,
3.3319922083528106, 2.908882086657216, 1.5549296972313118,
4.389767512591797, 2.697327025809418]


#HOM200s_4params =
[0.3158897122162896, 0.49526697586018303, 1.0, 0.12565702095309167,
0.8985792114599093, 0.507192811409887, 0.4096039655876192, 1.0,
0.7142542590330233, 1.0, 6.283185307179586, 3.0196686102857804,
4.135007442767116, 4.580286498026535, 6.283185307179586,
2.90303422517735, 0.8892154001954495, 0.0, 4.724650018003641,
2.0899147879389126]

#HOM200s_5params =
[0.35980268374784624, 0.7429692795535386, 1.0, 0.003296679876409277,
0.8526619979563494, 0.7104751861294885, 0.04814305920146503,
0.840667964384551, 0.8442266490336724, 0.9607610384233028,
6.221757359923743, 2.8410178496478937, 4.874237637438109,
4.897477451943646, 6.283185307179586, 2.880067330294334,
0.6950956935366217, 0.0, 4.591262530562544, 1.4099913527255015]


#g2_40s_1params =
[0.6161616161616161, 0.6531986531986531, 0.6632996632996633,
0.6599326599326599, 0.6464646464646464, 0.595959595959596,
0.46464646464646464, 0.41750841750841755, 0.5454545454545454,
0.5050505050505051, 3.2579479370560818, 2.9406153457843853,
```

```
2.3694166814953324, 2.136706114562755, 3.1944814188017423,
4.167634698701611, 3.977235143938593, 2.982926357953945,
3.088703888377844, 2.9194598396996057]

#g2_40s_2params =
[0.5387205387205387, 0.6599326599326599, 0.5622895622895623,
0.6397306397306397, 0.5993265993265993, 0.6430976430976431,
0.3602693602693603, 0.5993265993265993, 0.5656565656565656,
0.38383838383838387, 2.3694166814953324, 4.167634698701611,
2.7079047788518085, 3.7022135648364562, 2.58097174234313,
3.7868355891755754, 2.7713712971061475, 2.9617708518691654,
3.1944814188017423, 2.475194211919231]

#g2_40S_3params =
[0.5925925925925926, 0.43434343434343436, 0.4814814814814815,
0.49158249158249157, 0.43434343434343436, 0.4444444444444445,
0.5420875420875421, 0.33333333333333337, 0.6060606060606061,
0.6127946127946128, 3.9560796378538132, 2.5175052240887905,
2.136706114562755, 3.6175915404973376, 3.829146601345135,
2.729060284936588, 2.5386607301735706, 2.644438260597469,
3.004081864038725, 3.1733259127169626]

#g2_40s_4params =
[0.41414141414141414, 0.34680134680134683, 0.36700336700336705,
0.632996632996633, 0.5925925925925926, 0.5589225589225589,
0.6599326599326599, 0.6632996632996633, 0.49158249158249157,
0.3535353535353536, 2.2001726328170945, 3.5329695161582184,
2.6655937666822487, 2.834837815360487, 3.5118140100734387,
3.5118140100734387, 4.146479192616831, 3.3214144553104212,
2.6021272484279097, 2.2636391510714335]

#g2_40s_5params =
[1.0, 0.8127093205905616, 0.3544103987615896, 0.7168355700807324,
0.0, 0.573142921420631, 0.0, 0.0, 1.0, 1.0, 6.283185307179586,
0.0, 0.0, 4.519384715244627, 3.1836232759831957, 3.4172478952344263,
0.0, 4.275334097920657, 6.283185307179586, 6.283185307179586]

#g2_40s_6params =
[1.0262242736997578, 0.8627093205905616, 0.37405160447799407,
```

```
0.7325334614814245, -0.04267745357849898, 0.5937289144382247,
-0.0027842300213036064, -0.017551509532152832, 1.0363632934492197,
0.9622731555682722, 6.111403090142579, -0.0814228373203104,
-0.11005614720536165, 4.751609050554386, 2.983036514838239,
3.3294297164183733, 0.25786213002656094, 4.19111981403027,
6.029423193222684, 6.289937347480263]

#g2_40s_7params =
[0.9929915994916548, 0.8332778098333329, 0.37536447549725205,
0.725391800439024, -0.03918989169522948, 0.5966729012388657,
0.006237415875297671, -0.0003961284627661821, 1.0774191797101407,
0.9388054161392247, 5.97416451885325, -0.055162128531932975,
-0.06699231665486238, 4.521476305743291, 3.0150913765330745,
3.3896261662280334, 0.38589055245189735, 4.331204451271682,
6.200680019389915, 6.530660905275519]

#g2_40s_7params =
[0.0, 0.0, 0.0, 0.22496302147259928, 1.0, 1.0, 1.0, 0.0,
0.0, 1.0, 6.283185307179586, 2.5363603404198476, 6.283185307179586,
4.562010858432769, 6.283185307179586, 0.0, 6.283185307179586,
6.283185307179586, 0.007204920772935895, 0.0]

#Initialise phase and amplitude arrays.
phase_array = np.zeros(pixel_width)
A_array = np.zeros(pixel_width)

#Populate phase_array and amplitude array with paramters from param.
for p in range(9):
    phase_array[142+p] =np.round(params[p+9]) #Used np.round to discretize
                                                phase parameters.
    A_array[142+p] =params[p]

#Creates the array size random array values.
float_img=np.zeros((pixel_width,size))

for i in range(0,pixel_width):

    float_img[i]=alpha*((A_array[i])*(2.0*a/pi)
                 *np.arctan(1.0/(np.tan((x-((phase_array[i])/512))*pi/d))))
```

```
float_img=np.transpose(float_img)

img = np.array(((float_img))/(alpha)*256, dtype = np.uint8)
        #array of size width*height with random integers [0,255]

cv2.moveWindow("window",1680,0) #Move window to the SLM

cv2.namedWindow("window", 0);

cv2.namedWindow("window", cv2.WND_PROP_FULLSCREEN)
#name a window to display SLM array

cv2.resizeWindow("window",512,512);

cv2.imshow("window", img) #show the window

cv2.waitKey(1)#allow a new array to put up almost immediately.
```